

2015

# Swash zone dynamics of coarse-grained beaches during energetic wave conditions

Almeida, Luis Pedro

<http://hdl.handle.net/10026.1/3837>

---

<http://dx.doi.org/10.24382/4590>

Plymouth University

---

*All content in PEARL is protected by copyright law. Author manuscripts are made available in accordance with publisher policies. Please cite only the published version using the details provided on the item record or document. In the absence of an open licence (e.g. Creative Commons), permissions for further reuse of content should be sought from the publisher or author.*

**SWASH ZONE DYNAMICS OF COARSE-GRAINED BEACHES  
DURING ENERGETIC WAVE CONDITIONS**

by

**LUIS PEDRO MELO DE ALMEIDA**

A thesis submitted to the University of Plymouth  
in partial fulfilment for the degree of

**DOCTOR OF PHILOSOPHY**

School of Marine Sciences and Engineering  
Faculty of Science

**June 2015**

This copy of the thesis has been supplied on condition that anyone who consults it is understood to recognise that its copyright rests with its author and that no quotation from the thesis and no information derived from it may be published without the author's prior consent.

## ABSTRACT

**Name:** Luís Pedro Melo de Almeida

**Title:** Swash zone dynamics of coarse-grained beaches during energetic wave conditions

Coarse-grained beaches, such as pure gravel (PG), mixed sand-gravel (MSG) and composite (CSG) beaches, can be considered as one of the most resilient non-cohesive morpho-sedimentary coastal environments to energetic wave forcing (e.g., storms). The hydraulically-rough and permeable nature of gravel ( $D_{50} > 2$  mm), together with the steep (reflective) beach face, provide efficient mechanisms of wave energy dissipation in the swash zone and provide a natural means of coastal defence. Despite their potential for shore protection very little is known about the response of these environments during high energetic wave conditions.

Field measurements of sediment transport and hydrodynamics on coarse-grained beaches are difficult, because there are few instruments capable of taking direct measurements in an energetic swash zone in which large clasts are moving, and significant morphological changes occur within a short period of time. Remote sensing methods emerge in this context as the most appropriate solution for these types of field measurement. A new remote sensing method, based around a mid-range ( $\sim 50$  m) 2D laser-scanner was developed, which allows the collection of swash zone hydrodynamics (e.g., vertical and horizontal runup position, swash depth and velocity) and bed changes on wave-by-wave time scale. This instrument allowed the complete coverage of the swash zone on several coarse-grained beaches with a vertical accuracy of approximately  $\pm 0.015$  m and an average horizontal resolution of 0.07 m. The measurements performed with this new methodology are within the accuracy of traditional field techniques (e.g. video cameras, ultrasonic bed-level sensors or dGPS).

Seven field experiments were performed between March 2012 and January 2014 on six different coarse-grained beaches (Loe Bar, Chesil, Slapton, Hayling Island, Westward Ho! and Seascale), with each deployment comprising the 2D laser-scanner together with complementary *in-situ* instrumentation (e.g., pressure transducer, ADV current meter). These datasets were used to explore the hydrodynamics and morphological response of the swash zone of these different environments under different energetic hydrodynamic regimes, ranging from positive, to zero, to negative freeboard regimes.

With reference to the swash zone dynamics under storms with positive freeboard regimes (when runup was confined to the foreshore) it was found that extreme runup has an inverse relationship with the surf scaling parameter ( $\varepsilon = \pi^2 H_s / g T_p \tan^2 \beta$ ). The highest vertical runup excursions were found on the steepest beaches (PG beaches) and under long-period swell, while lower vertical runup excursions were linked to short-period waves and beaches with intermediate and dissipative surf zones, thus demonstrating that the contrasting degree of wave dissipation observed in the different types of surf zones is a key factor that control the extreme runup on coarse-grained beaches.

Contrasting morphological responses were observed on the different coarse-grained beaches as a result of the distinct swash\surf zone hydrodynamics. PG beaches with narrow surf zone presented an asymmetric morphological response during the tide cycle (accretion during the rising and erosion during the falling tide) as a result of beach step adjustments to the prevailing hydrodynamics. On dissipative MSG and CSG beaches the morphological response was limited due to the very



dissipative surf zone, while on an intermediate CSG beach significant erosion of the beach face and berm was observed during the entire tide cycle as a result of the absence of moderate surf zone wave dissipation and beach step dynamics.

Fundamental processes related to the link between the beach step dynamics and the asymmetrical morphological response during the tidal cycle were for the first time measured under energetic wave conditions. During the rising tide the onshore shift of the breaking point triggers the onshore translation of the step and favors accretion (step deposit development), while during the falling tide the offshore translation of the wave breaking point triggers retreat of the step and favours backwash sediment transport (erosion of the step deposit).

Under zero and negative freeboard storm regimes (when runup exceeds the crest of the barrier or foredune), field measurements complimented by numerical modelling (Xbeach-G) provide clear evidence that the presence of a bimodal wave spectrum enhances the vertical runup and can increase the likelihood of the occurrence of overtopping and overwash events over a gravel barrier. Most runup equations (e.g., Stockdon et al., 2006) used to predict the thresholds for storm impact regime (e.g., swash, overtopping and overwash) on barriers lack adequate characterisation of the full wave spectra; therefore, they may miss important aspects of the incident wave field, such as wave bimodality. XBeach-G allows a full characterization of the incident wave field and is capable of predicting the effect of wave spectra bimodality on the runup, thus demonstrating that is a more appropriate tool for predicting the storm impact regimes on gravel barriers.

Regarding the definition of storm impact regimes on gravel barriers, it was found that wave period and wave spectra bimodality are key parameters that can affect significantly the definition of the thresholds for these different regimes. While short-period waves dissipate most of their energy before reaching the swash zone (due to breaking) and produce short runup excursions, long-period waves arrive at the swash zone with enhanced heights (due to shoaling) and break at the edge of the swash, thus promoting large runup excursions. When offshore wave spectrum presents a bimodal shape, the wave transformation on shallow waters favours the long period peak (even if the short-period peak is the most energetic offshore) and large runup excursions occur.

XBeach-G simulations show that the morphological response of fine gravel barriers is distinct from coarse gravel barriers under similar overtopping conditions. While on coarser barriers overtopping regimes are expected to increase the crest elevation and narrow the barrier, on fine barriers sedimentation occurs on the back of the barrier and in the lower beach face. Such different sedimentation patterns are attributed to the different hydraulic conductivity of the different sediment sizes which control the amount of flow dissipation (due to infiltration) and, therefore, the capacity of the flow to transport sediment across and over the barrier crest.

The present findings have significantly improved our conceptual understanding of the response of coarse-grained beaches during storms. A new field technique to measure swash dynamics in the field was developed during this thesis and has great potential to become widely used in a variety of coastal applications.

## **AUTHORS DECLARATION**

At no time during the registration for the degree of Doctor of Philosophy has the author been registered for any other University award without prior agreement of the Graduate Sub Committee.

Work submitted for this research degree at the Plymouth University has not formed part of any other degree either at Plymouth University or at another establishment.

This study was financed with the aid of a studentship from the Engineering and Physical Sciences Research Council (EPSRC) research project - ARCoES Adaptation and Resilience of the UK Energy System to Climate Change (EPSRC reference: EP/1035390/1) and carried out in collaboration with another EPSRC project – NUPSIG – New Understanding and Prediction of Storm Impacts on Gravel beaches (grant EP/H040056/1) and Plymouth University.

The author acknowledges the collaborative contribution from Peter Granderton, Plymouth University, and Robert McCall, Deltares (Netherlands). Peter Ganderton provided fundamental support on the design and preparation of all the field instrumentation used in all the field experiments. Robert McCall provided extremely important guidance on the use of the numerical model XBeach-G on Chapters 3 and 4.

Relevant scientific seminars and conferences were regularly attended at which work was often presented; external institution was visited for consultation purposes and several papers prepared for publication.

## **Publications:**

**Almeida, L.P.**, Masselink, G., Russell, P., Davidson, M., Poate, T., McCall, R., Blenkinsopp, C., Turner, I., 2013. Observations of the swash zone on a gravel beach during a storm using a laser-scanner. *Journal of Coastal Research Proceedings 12th International Coastal Symposium* (Plymouth, England), pp. 636–641 (Special Issue No. 65).

**Almeida, L.P.**, Masselink, G., Russell, P., Davidson, M., McCall, R., Poate, T., 2014. Swash zone morphodynamics of coarse-grained beaches during energetic wave conditions. *Proceedings to International Conference on Coastal Engineering*, Seoul, South Korea.

**Almeida, L.P.**, Masselink, G., Russell, P., Davidson, M., 2015. Observations of gravel beach dynamics during high energy wave conditions using a laser scanner. *Geomorphology* 228 (0), 15, 27.

McCall, R., Masselink, G., Poate, T., Roelvink, J., **Almeida, L.P.**, Davidson, M., Russell, P., 2014. Modelling storm hydrodynamics on gravel beaches with Xbeach-G. *Coastal Engineering* 91, 231, 250.

McCall, R., Masselink, G., Poate, T., Roelvink, D., **Almeida, L.P.**, 2015. Modelling storm morphodynamics on gravel beaches with Xbeach-G. *Coastal Engineering*, 91, 231-250.

Masselink, G., Scott, T., Poate, T., **Almeida, L.P.**, Inch, K., Davidson, M., Russell, P., Conley, D. Measuring extreme storm dynamics and response on sandy and gravel beaches: regional monitoring and storm surveys. Submitted to *Earth Surface Processes and Landforms*.

#### **Presentation and Conferences Attended:**

Almeida, L., Masselink, G., Russell, P., Davidson, M., Poate, T., McCall, R., Blenkinsopp, C., Turner, I. *Observations of the swash zone on a gravel beach during a storm using a laser-scanner*. Oral presentation at 12<sup>th</sup> ICS -International Coastal Symposium, Plymouth, UK. April 2013

Almeida, L.P., Masselink, G., Russell, P., Davidson, M., McCall, R., Poate, T. *Swash zone morphodynamics of coarse-grained beaches during energetic wave conditions*. Oral presentation at International Conference on Coastal Engineering, Seoul, South Korea. June 2014

Word count of main body of thesis: 42,154

Signed: 

Date: 27/10/2015

# TABLE OF CONTENTS

<b>LIST OF FIGURES</b>	<b>IX</b>
<b>LIST OF TABLES</b>	<b>XV</b>
<b>ABBREVIATIONS AND SYMBOLS</b>	<b>XVI</b>

<b>1</b>	<b>Introduction.....</b>	<b>1</b>
1.1	Project Context.....	2
1.2	Scientific context.....	6
1.3	Project Aim and Objectives.....	10
1.4	Project Structure.....	12
<b>2</b>	<b>Development of a new tool to measure swash zone dynamics during a storm: application to a gravel beach.....</b>	<b>14</b>
2.1	Introduction .....	14
2.2	Methods.....	18
2.2.1	Study site and field deployment.....	18
2.2.2	2D Laser-scanner and working principle.....	22
2.3	Results .....	24
2.3.1	Processing and validation of Laser-scanner measurements.....	24
2.3.1.1	Correction of the laser measurements position and orientation.....	24
2.3.1.3	Separation between bed level and water surface .....	27
2.3.1.4	Defining the separation threshold.....	28
2.3.1.5	Comparisons between laser-scanner measurements and state-of-the-art techniques	30
2.3.2	Insight into the swash zone morphodynamics of gravel beach .....	33
2.3.2.1	Wave and tide records .....	33
2.3.2.2	Data analysis.....	34

2.3.2.3 Swash hydrodynamics .....	36
2.3.2.4 Swash morphological response.....	39
2.4 Discussion .....	43
2.4.1 Deployment and data analysis using a laser scanner .....	43
2.4.2 Comparison of laser measurements and state-of-the-art instruments.....	44
2.4.3 Insight into gravel beachface morphodynamics gained using the laser scanner.....	45
2.5 Conclusion.....	50
<b>3 Swash zone morphodynamics and extreme runup of coarse-grained beaches during energetic wave conditions.....</b>	<b>51</b>
3.1 Introduction .....	51
3.2 Methods.....	54
3.2.1 Study sites and field deployments.....	54
3.2.3 2D Laser-scanner .....	59
3.2.3 Xbeach-G model .....	60
3.3 Results .....	62
3.3.1 Wave and tide records.....	62
3.3.2 Field data analysis and Xbeach-G modelling .....	65
3.3.3 Wave conditions on the swash .....	69
3.3.4 Swash hydrodynamics.....	72
3.3.5 Swash morphological response.....	74
3.3.6 Beach morphodynamic states and runup .....	76
3.3.7 Xbeach-G modelling .....	77
3.4 Discussion .....	79
3.4.1 Wave breaking and swash boundary conditions .....	79

3.4.2	Swash hydrodynamics and morphological response .....	80
3.4.3	Extreme runup on coarse-grained beaches.....	82
3.4.3	The effect of groundwater and morphological evolution on the runup ....	84
3.5	Conclusion.....	86
<b>4</b>	<b>Measuring and modelling storm overwash on a gravel barrier .....</b>	<b>88</b>
4.1.	Introduction .....	88
4.2.	Methods .....	90
4.2.2	2D Laser-scanner .....	92
4.2.3	Xbeach-G model description .....	94
4.3	Results .....	97
4.3.1	Waves, tides and laser-scanner measurements .....	97
4.3.2	Xbeach-G validation .....	105
4.3.2.1	Hydrodynamics .....	105
4.3.2.2	Morphodynamics .....	108
4.3.3	Overtopping and overwashing discharge under variable wave height and water levels 110	
4.3.4	The effect of wave period, spectral shape and groundwater on the definition of storm impact regimes.....	114
4.3.5	Morphological response under different regimes .....	117
4.4	Discussion .....	120
4.4.1	Measuring wave overtopping on a gravel barrier with a laser-scanner ..	120
4.4.2	The use of Xbeach-G to predict overtopping and overwash on a gravel barrier.....	122
4.4.3	Defining storm impact regimes on Loe Bar.....	125
4.5	Conclusion.....	128

<b>5</b>	<b>Discussion and Conclusions .....</b>	<b>130</b>
5.1.	Development of a 2D laser-scanner to measure swash zone during storms ..	130
5.1.1	Advantages and limitations .....	133
5.1.2	Future developments and applications .....	137
5.2	Morphodynamics of coarse-grained beaches during storms (positive freeboard.....	140
5.3	Storm impact regimes on gravel barriers .....	148
5.4	Conclusions .....	156
	<b>References .....</b>	<b>161</b>
	<b>Appendix I .....</b>	<b>172</b>
	<b>Appendix II.....</b>	<b>176</b>

## LIST OF FIGURES

Figure 1.1 Diagram showing the organization of ARCoES project. ....	3
Figure 1.2 Diagram showing the organization of NUPSIG project. ....	5
Figure 1.3 ARCoES and NUPSIG project study sites around UK. The ARCoES sites with a red cross were not used in the present research project. ....	6
Figure 1.4 Sketch of the three types of coarse grained beaches (adapted from Jennings and Schulmeister, 2002). ....	6
Figure 1.5 Sketch of the three impact regimes of storms on coarse-grained beaches (adapted from Orford et al., 2003).....	10
Figure 1.6 Summary structure of the thesis including the bold objectives (black boxes) and specific objectives (green boxes) of each chapter. ....	13
Figure 2.1 Map showing the location of the study site (Loe Bar), the location of the offshore wave buoy and bathymetry. The wave rose represents 1 year (from October 2011 to October 2012) of directional wave buoy data. ....	18
Figure 2.2 Photos showing the deployment of the laser-scanner tower in the field (top and right panels), with the indication of the video camera pixel time-stack transect (T2) and bed-level sensors transect ( T1). Lower left panel shows the beach profile with locations of the equipment used during the survey. ....	20
Figure 2.3 Photo showing the scaffold frame with ultrasonic bed-level sensors covering of the gravel barrier. ....	21
Figure 2.4 Diagram of the 2D laser-scanner LD-OEM3100 (SICK) showing working principles in the field. ....	23
Figure 2.5 Comparison between laser-derived beach morphology and that measured using dGPS. Upper panels show comparison between dGPS profile and raw laser-derived profile (upper-left panel) and between dGPS profile and laser-derived profile corrected for mis-orientation and translation (upper-right panel). The lower panels show the associated residuals (difference between dGPS profile and laser-derived profile). ....	24
Figure 2.6 Average horizontal resolution of the laser-scanner measurements computed for different tower elevations, assuming 0.125 angular resolution and the same cross-shore position (top panel). Example of the laser-scanner horizontal resolution (black dots) computed for the laser-scanner beams (grey lines) using different laser-scanner elevations (5.2 – bottom left panel; and 1 m – bottom right panel).....	26
Figure 2.7 Raw laser-scanner measurements without the separation between beach topography and water (top panels), and after applying the separation methods (lower panels).....	27
Figure 2.8 Section of the beach profile analysed during 40 minutes of laser-scanner measurements and the respective angles of incidence (left panels); variance computed for each angle of incidence (right panel). The two horizontal lines in the right panel represent the two variance thresholds computed for two groups of angles of incidence. ....	29



Figure 2.9 Offshore wave conditions (black line) and tide (blue line) for the survey period with the indication of measurements performed with the different instruments: DGPS (green vertical lines); laser-scanner and bed level sensors (red areas); video (box with yellow dashed line);..	30
Figure 2.10 Comparison between DGPS measurements made on T0 and bed level sensors for the tides 1 and 2 (two figures on the top); comparisons between DGPS measurements made on T5 and the laser-scanner scan for the tides 1 and 2; residual between all the instruments: DGPS vs bed level sensors (green line), DGPS vs laser-scanner (red line), Laser vs bed level sensors (blue line) and DGPS vs DGPS (black line) (lower figures).	31
Figure 2.11 Comparison between the $R_{2\%}$ computed with the laser-scanner and video camera (upper panel); scatter diagram of the measured $R_{2\%}$ with video vs. $R_{2\%}$ measured with Laser-scanner (bottom panel), with the linear regression line (red line).	32
Figure 2.12 Time series of significant wave height (upper left panel), peak wave period (upper right panel), wave direction (lower left panel) and tide elevation (lower right panel). Solid black lines represent offshore wave conditions measured by the offshore wave buoy, solid gray lines are measurements made by the pressure transducer on the beach deployed just above high tide level, and the dashed line represents tide measurements performed at Porthleven by a pressure transducer deployed around the MLWS level.	33
Figure 2.13 Time series of runup elevation ( $R$ ) and explanation for deriving swash instantaneous velocities ( $u$ ) and vertical runup excursions ( $R_{exc}$ ).	35
Figure 2.14 Time series of runup elevation ( $R$ ) measured by the laser-scanner (gray line) during Tide 2 and the measured tide elevation (dashed black line).	36
Figure 2.15 Swash hydrodynamics calculated from the laser-scanner measurements: the normalized 2% exceedence of the runup maxima ( $R_{2\%}/H_s$ - top left panel), swash velocity skewness ( $\langle u^3 \rangle$ - top right panel), normalized runup standard deviation ( $R_{\sigma}/H_s$ - bottom-left panel), and normalized mean and maximum runup vertical excursions ( $mean(R_{exc})/H_s$ and $max(R_{exc})/H_s$ - bottom-right panel).	37
Figure 2.16 Runup power spectra (top panel) averaged for the rising (gray line) and falling tide (dashed line). The spectra have 16 degree of freedom and the frequency resolution is 0.0089 Hz. Significant normalized runup elevation (black line), normalized by the offshore significant wave height ( $S/H_s$ ) and the percentage of the significant infragravity runup elevation ( $\%S_{ig}$ - grey line) to the total runup energy (bottom panel).	38
Figure 2.17 Colour plot showing morphological change relative to the initial beach profile ('cumulative change') obtained from the laser-scanner during the tide cycle (top panel). The white and black line represent the average and maximum runup elevations and the black dashed line represents the average rundown minima computed for consecutive segments of 15 minutes of measurements. Step deposit elevation (mid panel) and shoreface slope (lower panel) during the tide cycle.	40
Figure 2.18 Field photos taken at high tide showing the lower swash gravel deposit (right); several beach profiles showing several stages of growth of the lower beach face deposit during the rising tide phase (left).	41
Figure 2.19 Sketch of the morphological response and runup characteristics of a gravel beach, over a tidal cycle during energetic wave conditions.	46

Figure 3.1 Study site locations, field photo and sketch of the type of beach profile showing shape, composition, location of the laser-scanner (red flag) and inshore pressure transducer (red cross), and highest and lowest water level (HWL and LWL) observed during the field experiments.	55
Figure 3.2 Raw measurements obtained from the laser-scanner (left panel) and the two types of time-series obtained after the data processing: 1) continuous topographic measurements (top-right panel) and 2) swash hydrodynamics (bottom-right panel).....	59
Figure 3.3 Tide height relative to ODN datum (black dashed line), offshore significant wave height (blue line – top panels), peak period, wave direction, wave steepness and normalized wave spectra with the overlap of the mean period ( $T_{m-10}$ ) measured by the offshore wave buoys during the laser measurements (grey areas).....	64
Figure 3.4 Two examples of swash velocity skewness results: left) time series of horizontal runup and respective instantaneous velocity (top), and resultant positively skewed velocity distribution (bottom); right) time series of horizontal runup and respective instantaneous velocity (top), and resultant negatively skewed velocity distribution (bottom). ....	66
Figure 3.5 Sketch of the swash and effective slope calculations. ....	68
Figure 3.6 Scatter diagram of the offshore significant wave height measurements versus the inshore significant wave height measurements for all the sites. ....	70
Figure 3.7 Field photos showing the breaking conditions at each of the study sites during the field experiment; and surf similarity (black line) computed for the time when laser-scanner measurements were performed (grey areas). ....	71
Figure 3.8 Time series of vertical runup (grey) with the overlap of the tide elevation (black line – top panels); 2% exceedence of the runup maxima (second line of panels); vertical runup spectra, normalized by total energy (third line of panels); and swash flow skewness (bottom line of panels), computed for all the sites. ....	73
Figure 3.9 Contour plots showing the cumulative topographic changes calculated from the laser-scanner observations (top panels) with the overlap of the maximum and mean runup and minimum backwash position (black lines); swash gradient (second row of panels); and a sketch of the representative morphological changes observed during a tide cycle (lower panels). ....	75
Figure 3.10 Scatter diagram of the surf scaling parameter versus the extreme runup ( $R_{2\%}/H_s$ ) for all the sites. Surf scaling was computed using (a) $T_p$ and $\beta_{profile}$ , (b) $T_{m-10}$ and $\beta_{profile}$ , (c) $T_p$ and $\beta_{swash}$ and (d) $T_{m-10}$ and $\beta_{swash}$ . ....	76
Figure 3.11 Comparison between the measured (red) and modelled (blue) runup and rundown limits at Chesil Beach.....	85
Figure 4.1 Location of the Loe Bar study site, the Porthleven wave buoy and the Newlyn tide gauge (inset maps). Aerial photograph of Loe Bar with the overlap of the digital terrain model from a Lidar survey (survey performed by the Channel of Coastal Observatory in 2013) with the laser-scanner position and scan profile indicated. ....	91
Figure 4.2 Field photographs showing the laser-scanner setup (right panel) and the deployment of the scanner on the crest of Loe Bar during overwash conditions (top left panel), and detailed cross-shore profile of the barrier indicating position of the laser scanner and sea and lagoon water levels (bottom left panel).....	92

Figure 4.3 Sequence of video snapshots (top) and corresponding laser-scanner measurements (bottom) during an overwash event over the barrier. ....	93
Figure 4.4 Corrected tide level and surge measurements for Porthleven harbour (top panel); offshore wave conditions, including significant and maximum wave height (second panel), peak period (third), wave direction (fourth panel) and normalised spectra (bottom panel), measured at Porthleven offshore wave buoy; shaded area corresponds to the period of time when laser measurements were performed. ....	98
Figure 4.5 Vertical (top panel) and horizontal (second panel) runup excursions and morphology cumulative changes (bottom panel) measured by the laser-scanner. Red line indicates the location of the crest of the barrier. ....	99
Figure 4.6 Cross-shore barrier profile with location of the point (red cross) where overwash discharge was computed (left panel) and example time series of water elevation (top right panel), overwash front velocity (middle right panel) and estimated overwash discharge (bottom right) for a single overwash event measured by the laser-scanner. ....	101
Figure 4.7 Characteristics of the overwash events measured by the laser-scanner: time series of overwash depth for each event (top panel); average and maximum overwash depth (second panel); average and maximum overwash front velocity (third panel); and average and maximum overwash discharge (bottom panel). ....	102
Figure 4.8 Mean and maximum overwash front velocity at the crest as a function of mean and maximum overwash depth at the crest * gravitational acceleration (g). The dam break equation is plotted in the figure (green dashed line) together with a linear fit (black line) between these two parameters. ....	104
Figure 4.9 Cross-shore profile used for the model validation (left panel), and example of the bed evolution for Setups 2 and 4 (right panel). ....	106
Figure 4.10 Example of XBeach-G output for the simulations with Setup 1, showing the time series of vertical (top panel) and horizontal (middle panel) runup and the overwash discharge (bottom panel) computed for the storm conditions observed during the present experiment. Red dashed line indicates the position and elevation of the barrier crest. ....	107
Figure 4.11 Comparison between measured and modelled morphological response to a storm event, with the top panels showing the cumulative vertical changes and the bottom panel comparing the initial measured profile with the final measured profile and those predicted by Xbeach-G. Two XBeach-G models were run: groundwater = ON and groundwater = OFF. ....	109
Figure 4.12 Contour map of the average wave overtopping and overwash discharge under different significant wave height and water level conditions, overlain by a bivariate histogram of measured $H_s$ and water level for waves with $T_p > 10$ s (wave data source: Porthleven wave buoy; tide source: Newlyn tide gauge). The yellow dots represent the mid-regime forcing conditions for which the effect of changing wave period, spectral shape and groundwater interactions will be explored later in this chapter. ....	111
Figure 4.13 Results of the overtopping discharge (lower panels) computed using a bimodal (top left panel) and unimodal Jonswap spectra (top right panel) with the same $T_m = 10$ s and $H_s = 4.5$ , using $\gamma = 2$ . ....	113
Figure 4.14 Wave spectrum computed for each time series of water elevations predicted for each cross-shore position of the grid from the model outputs presented in Figure 14. ....	114

Figure 4.15 Shape of the three different wave spectra tested for each regime; these wave spectra are representative of the simulations performed with the $T_p = 10$ s. ....	115
Figure 4.16 Discharge under variable $T_m$ values for the different regimes, testing different parameters: typical Jonswap spectra with groundwater ON (black line); with groundwater OFF (dashed grey line); and testing different wave spectral shapes (red, blue and green lines). The yellow dots represent the mid-regime simulations indicated in Figure 13. ....	116
Figure 4.17 Contour maps of the net of changes predicted for Loe Bar barrier under different impact regimes, with varying mean wave period ( $T_m$ ), spectral shapes and using groundwater off, using Xbeach-G. The dashed line represents the barrier crest and the two other black lines represent the mean water level and rundown limit. ....	118
Figure 4.18 Example of the two morphological responses of the gravel barrier under an overtopping regime. ....	119
Figure 4.19 Morphological response of Loe Bar under overtopping impact regime for different wave periods and using different sediment sizes. Green dashed line represents the barrier crest while the two black dashed lines indicate the lower and mid limit of the water level. ....	124
Figure 4.20 Volume deposited at the back of the barrier as a function of average overwash discharge at the crest (top panel). The power fitting adjustment to data is represented with a black line. Crest lowering as a function of average overwash discharge at the crest (bottom panel). ....	126
Figure 4.21 Map showing the average overwash discharge threshold (20 l/s/m) predicted using different wave period ( $T_m$ ) and wave spectrum shape. ....	127
Figure 5.1 Field photos from each field deployment performed with the laser-scanner, showing the large variety of environments and setup types (e.g., mounted on the beach or at the top of a seawall). ....	132
Figure 5.2 Theoretical laser-beam trajectories during a scanner rotation (gray lines) and horizontal distance between measurements (black dots) performed by the laser-scanner at each of the study sites. ....	136
Figure 5.3 Sequence of photos showing the deployment of the laser-scanner on top of the seawall at Chesil on the 05/02/14 during an extreme storm. ....	138
Figure 5.4 Time series of: (a) significant wave height $H_s$ and tide level; (b) bed elevation at Chesil in south Devon during an extreme storm. ....	139
Figure 5.5 Conceptual diagram for coarse-grained beaches morphodynamics during storms; on the basis of this diagram is the relationship between surf scaling parameter and extreme vertical runup (top panel – the dashed area represents the relative range of vertical runup excursions under different regimes), which express the different types of surf zone dissipation (middle panel) and can be linked to the swash morphodynamics response (bottom panel). ....	143
Figure 5.6 Illustration of the link between breaking location and sediment transport during the rising and falling tide, and consequent morphological response. On the rising tide (left panels) the breaking point moves onshore and waves break more often landward from the beach step and the sediment transport favours uprush and step deposit development. On the falling tide (right panels) the breaking point moves offshore reducing the uprush sediment transport and enhancing backwash and erosion of the step deposit. ....	145

Figure 5.7 Comparison between vertical runup observations and predictions using Stockdon et al., (2006) runup equation and Xbeach-G numerical model (bottom panel), forced with 2 hours of wave measurements (performed at Porthleven wave buoy) during the storm presented in Chapter 4; Stockdon et al., (2006) runup equation was implemented using significant offshore wave height (top panel), peak period (second panel), while Xbeach-G used the full wave spectra (third panel). For these simulations it was used the tide elevation presented in Chapter 4..... 151

Figure 5.8 Diagram illustrating the effect of the modification of wave period and spectral shape on the definition of the overwash discharge threshold (left panel). This overwash discharge map was produced based on a combination of water levels and wave heights and using a hypothetical wave period time series which express the variability of this parameter along the time (top right panel); the different statistical moments of this distribution (mean, max and min) were used to produce the discharge map, using different wave spectra shapes: unimodal and bimodal (bottom right panel). ..... 152

Figure 5.9 Illustration of the two types of morphological response that a coarse (left) and a fine (right) gravel barrier present under overtopping conditions. .... 155

## LIST OF TABLES

Table 3.1 Wave climate, tides and sediment characteristics of the study sites.....	56
Table 3.2 Results of the statistical measures ( <i>rmse and bias</i> ) for the comparison between the measured (laser-scanner) and modelled $R_{2\%}$ .....	78
Table 4.1 Sediment properties used in the simulations.....	105
Table 4.2 Results of the comparison between Xbeach-G .....	108

## ABBREVIATIONS AND SYMBOLS

$H_s$	Significant wave height
$T_p$	Peak wave period
$T_{m-1,0}$	Mean wave period
$m_1$	First moment of the wave spectrum
$m_0$	Zero moment of the wave spectrum
$\theta_{wave}$	Mean wave direction
$L_0$	Offshore wave length
MHWS	Mean high water spring
MLWS	Mean low water spring
$\tan\beta$	Beach gradient
$\beta$	Bed slope
$\beta_{swash}$	Slope of the swash zone
$\beta_{effective}$	Effective slope
$t$	Time
$g$	Gravitational constant
$R$	Vertical runup
$R_{zmodel}$	Modelled vertical runup
$R_\sigma$	Standard deviation of vertical runup
$R_{2\%}$	2% of exceedance of the vertical runup maxima
$R_{exc}$	Vertical runup excursion
$u$	Cross-shore instantaneous velocity of the runup edge
$u_{crest}$	Cross-shore instantaneous velocity of the runup edge at the crest of the barrier
$\langle u^3 \rangle$	Flow velocity skewness
$S$	Significant vertical runup
$S_{ig}$	Significant infragravity vertical runup
$h_c$	Overwash depth at the barrier crest

$q_c$	Average overwash discharges at the crest
$D_{50}$	Median grain size
$D^*$	Non-dimensional grain size
$\rho$	Density of water
$\rho_s$	Density of the sediment
$Z_{topo}$	Laser-scanner bed elevation
$Z_{lazer}$	Laser-scanner raw measurements
$\sigma^2_{threshold}$	Variance threshold (laser-scanner)
$x$	Horizontal spatial coordinates
$\xi$	Surf similarity parameter
$\varepsilon$	Surf scaling parameter
$\zeta$	Free surface elevation above an arbitrary horizontal plane
$\xi_b$	Elevation of the bed above an arbitrary horizontal plane
$c_f$	Bed friction factor
$\Delta_i$	Effective weight of sediment
$\alpha$	Empirical constant relating the surface seepage force to the seepage force in the bed
$\bar{H}$	Depth-averaged hydraulic head
$h$	Water depth
$h_{gw}$	Height of the groundwater surface above the bottom of the aquifer
$K$	Hydraulic conductivity of the aquifer
$n$	Porosity
$\theta$	Shields parameter
$\theta_{cr}$	Shields parameter for the initiation of transport
$\emptyset$	Angle of repose
$q_b$	Volumetric bed load sediment transport rate
$\bar{q}$	Depth-averaged dynamic pressure
$s$	Surface water-groundwater exchange flux
$\tau_b$	Bed shear stress
$u_z$	Depth-averaged cross-shore velocity
$w_{gw,s}$	Vertical groundwater velocity at the groundwater surface



$u_{gw}$	Depth-averaged horizontal groundwater velocity
$\nu$	Kinematic viscosity coefficient of water
$\nu_h$	Horizontal viscosity
$\gamma$	Calibration coefficient (bed load Van Rijn (2007) transport equation)

## ACKNOWLEDGEMENTS

I would like to thank my supervisory team, Gerd Masselink, Paul Russell and Mark Davidson for giving me this unique opportunity to participate in such an amazing professional and personal experience. Their support and availability were impeccable and I couldn't have asked for any more. Gerd, thank you very much for sharing such amount of energy, enthusiasm and knowledge, and to be always available when I needed. It was extremely motivating to work with someone with such commitment and enthusiasm; I learned and enjoyed a lot to work with you! Paul, thank you a lot for your wise advises and for your positive energy, essential to keep the motivation high and to face life with the right mind set. Mark, thank you very much for always be available to give your advice and also to be always positive and encouraging. I will keep always very good memories of the time I've spend with all of you in the field, during storms and good weather, on very nice beaches or just in front of the power stations! For you all I do want to express my gratitude and friendship, because besides the professional side, I had very good personal experiences with all of you!

I would like to thank all the great people involved in the field experiments and with who I shared very good moments of my life during these last 3 years and half: Gerd, Tim Poate, Claire Earlie, Kris Inch, Paul Russell, Mark Davidson, Kit Stokes, Erwin Bergsma, Rob McCall, Olivier, Sam Prodger, Marcus Zanicchi, Tim Scott, Ellie, Andrea. A special thanks to Peter Ganderton and Megan for their support to all field experiments and for teaching me so much about many technical details, which are fundamental in this job.

A special thank you to all my colleagues, but more importantly, friends with who I spend most of my time sharing the office, very good, and not so good moments of this journey: Claire Earlie, Kit Stokes, Barbara Proenca, Sam Cox, Erwin, Carlos Collazo, Kris Inch, Davide Banfi, Javier, Gregorio, Guiomar, Ellie, Marcus, Ed, Anthony Thorpe, Olivier, Sam Prodger and Thomas. I'll never forget the moments we have shared together and I think that it couldn't be possible to ask for a better group of people to have as office mates rather than this.

I also would like to say thank you to all friends from outside de Marine Building who made my life experience in Plymouth (and UK in general) a really nice life experience: Nicky and Ian, Sam and Thomas, Toby and Jennifer, Robert and Joanna, Rafa and Lara, Andre Antunes, and my football team mates (Santos).

I would like to dedicate this thesis to my love, best friend and companion, my wife Paula, for the patience and support and to be my main source of inspiration and happiness. You were always there during the good and bad times and without you this PhD/life experience in Plymouth would not be the same. I would like also to dedicate this thesis to my parents, Elisabete and Albino, because without them I wouldn't exist and would not be here having such an amazing life experiences. This thesis represents a small retribution to all what they have done for me. To all my family and friends that supported me during this important period of my life: my sister Ana and Ricky, Tia Lena, Tio Mario Jorge and Dina, Tio Vitor and Gracinda, Joao Matos, Andre Pacheco! Many thanks. A special thanks to Simon Connor (Simao) for all the help with the English revision and for is friendship!

Finally I would like to dedicate this thesis to my grand-mother (Maria das Neves) as well, who is 100 years old and is proud to see her grandson that she kindly helped to grow, accomplish a PhD diploma.

# 1. Introduction

This chapter presents the scientific context of this thesis and the work that is presented in the following Chapters. The framework of the thesis is introduced with a brief outline of the context of the present research project and the wider projects it sits within and contributes to. This is followed by the aim and objectives of this research project, and an outline of the thesis structure.

The research reported in this PhD thesis is largely field-based with data collection at several coastal sites in the UK. As explained in the next section, the planned field sites for this research were coastal sites characterised by the presence of nuclear power stations and the objective was to collect high-energy (storm) data sets of hydrodynamics and morphological response. These sites are part of the Adaptation and Resilience of Coastal Energy Supply in the UK (ARCoES) project. However, wave conditions were such that only one of these sites could be successfully instrumented. To address the scientific objectives of this PhD, additional field sites were used to provide high-energy data sets. These sites were all coarse-grained beaches and the data were collected as part of the New Understanding and Prediction of Storm Impacts on Gravel beaches (NUPSIG) project. In the next section the ARCoES project is discussed in some detail, but some discussion of the NUPSIG project is also provided.

## **1.1 Project Context**

The security of the UK nuclear energy sector and coastal energy supply faces important challenges due to the present projections of future sea level rise (Nicholls et al., 2011) and changing patterns of storminess (Feser et al., 2014). The threats posed to future energy generation and the distribution network by flooding and changing patterns of coastal sedimentation (e.g., erosion) need to be assessed and brought into discussions that decide the future of energy supply in the UK.

To contribute to these discussions Liverpool University gathered an inter-disciplinary consortium composed of universities (Universities of Plymouth, Loughborough, Southampton, Stirling, St Andrews and Salford Manchester), research institutions (National Oceanography Centre), end-users drawn from the energy sector (EDF, National Grid, Electricity North West), government agencies and regulators (National Decommissioning Authority and Environmental Agency), environmental engineering (Royal Haskoning) and NGOs (e.g., BECC Working Group, RSPB), and started the ARCoES project - Adaptation and Resilience of Coastal Energy Supply (<https://www.liv.ac.uk/geography-and-planning/research/adaptation-and-resilience-of-coastal-energy-supply>). Funded by an EPSRC (Engineering and Physical Sciences Research Council) grant, this 5 year research project (from March 2011 to March 2016) aims to provide evidence and guidance to enable effective adaptation to the consequences of climate change at the coast, thus enhancing the resilience of coastal energy supply.

To achieve its overall aims the ARCoES project consists of three main strands (Figure 1.1), representing distinct work packages:

- 1) **Field data collection (WP1):** acquisition of field measurements during storm events at each of the pilot sites in order to characterize their resilience to extreme impacts (e.g., erosion, flooding).
- 2) **Numerical Modelling (WP2):** forecast future scenarios of coastal erosion and flooding using present projections of sea level rising and storminess, and quantify their respective economic impact.
- 3) **Decision support tool (WP3):** develop a decision support tool, based on GIS software, which allows the visualization of the modelling scenarios (e.g., flood maps) together with economic impacts and mitigation scenarios.

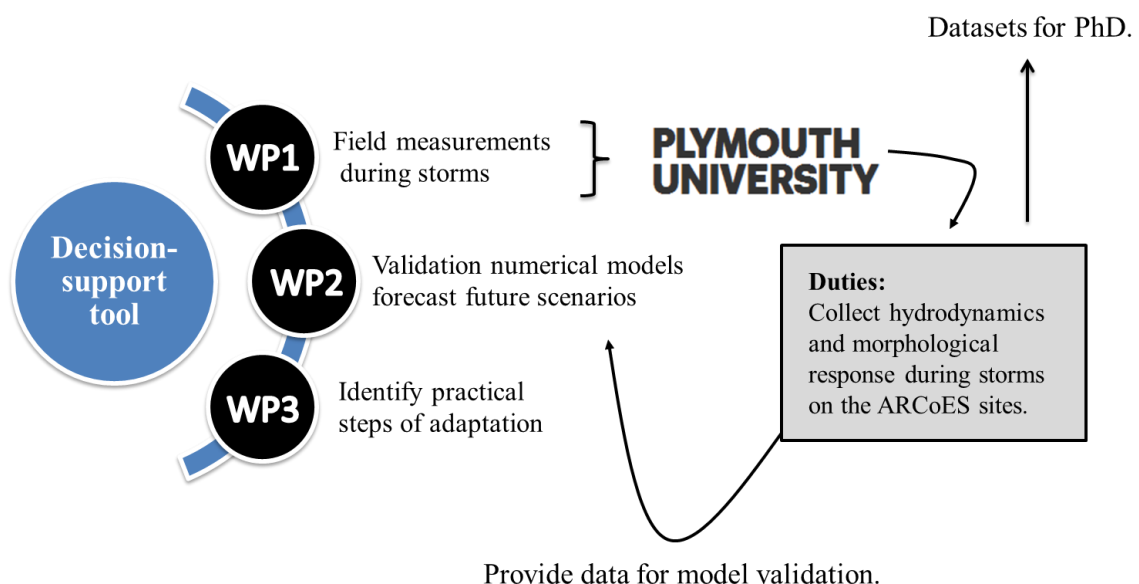


**Figure 1.1** Diagram showing the organization of ARCoES project.

Plymouth University, leader of WP1, was assigned to collect field measurements at each of the ARCoES pilot sites during storms, in order to characterize the resilience of these sites to extreme events, and provide storm datasets to WP2 (see Figure 1.1).

The present PhD research project, “Swash zone morphodynamics on coarse-grained beaches during energetic wave conditions”, was designed to incorporate the objectives of WP1; namely, the planning and execution of the field experiments. In addition to contributing to ARCoES, the PhD project also had to meet its own scientific aims and objectives.

Three ARCoES pilot sites (all adjacent to nuclear power stations – Seascale, Sizewell and Hinkley Point) were selected to be monitored during storms. Unfortunately the wave conditions were not sufficiently energetic to justify carrying out extensive and sophisticated field campaigns at these three sites, thus only one data set was collected (Seascale).

Additional sites and associated data sets were required to meet the scientific aims and objectives of the thesis. For this purpose the present research project was aligned with another ongoing research project, NUPSIG – New understanding and prediction of storm impact on gravel beaches ([www.research.plymouth.ac.uk/coastal-processes/projects/nupsigsite/home.html](http://www.research.plymouth.ac.uk/coastal-processes/projects/nupsigsite/home.html)), and a new set of field sites was added to the present thesis.

Funded by EPSRC, the NUPSIG project is a research collaboration between Plymouth University (project leader) and several governmental (e.g., Channel of Coastal Observatory, Environmental Agency) and private partners (e.g., Deltares, HR Wallingford), with a general aim to obtain new understanding of how gravel beaches are affected by storms, and to develop coastal management tools to help protect the coast of the UK against storms and rising sea levels. The structure of NUPSIG project (Figure 1.2) relies on the collection of detailed field measurements on gravel

beaches during storms, fundamental for the calibration and validation of a newly developed numerical model XBeach-G (McCall et al., 2014).

This numerical model is the basis of an end-user tool that this project will provide for predicting the impact of storms on gravel beaches (Masselink et al., 2014).



**Figure 1.2** Diagram showing the organization of NUPSIG project.

Since both ARCoES and NUPSIG project share a common aim, to improve our understanding of coarse-grained beaches response to storms, the merging of both projects field efforts was greatly beneficial for both projects.

The field sites (Figure 1.3) used in the present thesis (from both ARCoES and NUPSIG projects) are located on the West coast of Cumbria district (Seascale), along the South coast of Hampshire (Hayling Island), Dorset (Chesil), Devon (Slapton), Cornwall (Loe Bar) and North coast of Devon (Westward Ho!), all with different levels of exposure to the Irish Sea, North Atlantic and English Channel wave climate.



**Figure 1.3** ARCoES and NUPSIG project study sites around UK. The ARCoES sites with a red cross were not used in the present research project.

## 1.2 Scientific context

The selected ARCoES and NUPSIG sites offer a wide variety of morphologies and sediment composition which according with Jennings and Schulmeister (2002) classification cover the full range of coarse-grained beach types (Figure 1.4):

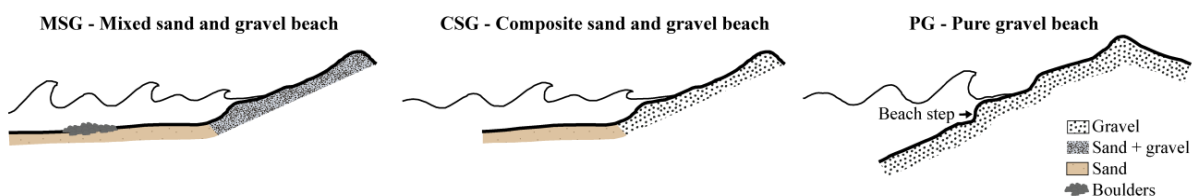


**Figure 1.4** Sketch of the three types of coarse grained beaches (adapted from Jennings and Schulmeister, 2002).



- **Pure gravel (PG):** the entire beach profile is dominated by gravel sediments ( $> 2$  mm); traditionally present very steep shoreface, offering reflective conditions at all stages of the tide (Carter and Orford, 1993). A key aspect of PG beaches is the development of a very narrow surf zone, adjacent to the swash zone, controlled by the beach step (Buscombe and Masselink, 2006). The sites within this class are: Loe Bar, Chesil and Slapton.
- **Composite sand and gravel (CSG):** due to hydraulic sorting these beaches present a profile with two distinct sections: the sandy and low-gradient lower profile section and an upper part composed of 'pure' gravel (Carter and Orford 1993). The two zones intersect at a distinct break in slope, although with no clear evidences of a beach step. The sites within this class are: WestwardHo! and Hayling Island.
- **Mixed sand and gravel (MSG):** the top of the profile is composed by a mixture of sand and gravel. Grain size can vary from sand to very coarse gravel, and on macrotidal beaches in UK, notably different from New Zealand settings (Kirk, 1980), MSG beaches are generally characterised by large intertidal terraces with mixed sand and gravel. Seascale is the only site that sits within this beach type.

Insights into shorter term coarse-grained beach dynamics have lagged behind our understanding of sandy coastlines, mainly because of the logistical problems associated with field experimentation (Buscombe and Masselink, 2006). Very few instruments are capable of direct measurements in an energetic swash zone in which large cobbles and gravels are moving (Osborne, 2005).

Under storm conditions, the levels of energy in the swash increase significantly prohibiting the deployment of *in-situ* instrumentation. Such logistic problems represent an extremely important

limitation regarding the assessment of the swash hydrodynamics and morphological response of a coarse-grained beach during a storm. Remote sensing instrumentation emerges in this context as the most adequate solution to perform field measurements during storms since they have the ability to perform measurements without being deployed *in-situ*.

From all the existing and emerging methods, laser technology (e.g., terrestrial laser-scanner or industrial laser-scanners) is the candidate with the greatest potential to overcome the present field limitations. The key aspects of this technique are the capacity to measure continuous (during daylight or night or raining conditions) and simultaneous measurements of the swash hydrodynamics and morphological evolution at very high frequencies (e.g., Blenkinsopp *et al*, 2010 or Brodie *et al.*, 2012).

On a short-term scale (hours), extreme storms are one of the most important agents of beach erosion and are also responsible for the destruction of coastal properties and engineering structures (e.g., Almeida *et al.*, 2012). The magnitude of the sediment exchanges between subaerial and subaqueous zones of the beach during a storm are dictated by the interaction between the hydrodynamics and morphology in the swash zone. It is generally recognized that the swash zone, region defined between minimum and maximum runup and rundown levels, is the most dynamic area of the nearshore, where strong unsteady flows, high levels of turbulence, large sediment transport rates and rapid morphological changes can occur at a wave-by-wave time scale (Butt and Russell, 2000; Elfrink and Baldock, 2002).

The swash zone plays a key role on the nearshore region since it represents the landward boundary for breaking wave energy dissipation and turbulence generation. Breaking wave-generated turbulence is exchanged between the surf zone and the swash zone, with the former acting as a sink for surf zone turbulence (Sou *et al.*, 2010). This turbulence is dissipated in the swash zone in the

form of wave runup, and can lead to important morphological changes such as dune erosion (Stockdon et al., 2006).

Wave runup is a key hydrodynamic parameter affecting coastal flooding and erosion, and is a function of the quasi-steady wave setup and the vertical extent of the fluctuating swash motion. The limit of wave runup is also a key parameter in the application of the storm-impact scale by Sallenger (2000). The Sallenger scale categorizes four levels of morphologic impact by storms through comparison of the highest elevation reached by storm water (combined storm surge and wave runup) and a representative elevation of the barrier island (*e.g.*, the top of the foredune ridge). Quantification of wave runup and its relationship to the upper limit of morphologic change are required for understanding and predicting beach-profile changes.

On coarse-grained beaches and barriers the conceptual understanding of the morphological impact of a storm is provided through consideration of the degree of freeboard available (*i.e.*, the difference between the elevation of the barrier crest and runup limit – Orford et al., 2003, Matias et al., 2012). This conceptual framework defines qualitatively the morphological impact of a storm under three hydrodynamic regimes (Figure 1.5):

- **Positive freeboard:** occurs when the runup is confined to the foreshore, and traditionally associated to the berm development or erosion (Buscombe and Masselink, 2006);
- **Zero freeboard:** occurs when runup exceeds the crest barrier elevation and promotes crest build-up (overtopping - Orford and Carter, 1982) resulting in increased barrier crest elevation;
- **Negative freeboard:** occurs when overwash takes place, causing crest lowering which in turn can promote barrier transgression via rollover (Carter and Orford, 1993).

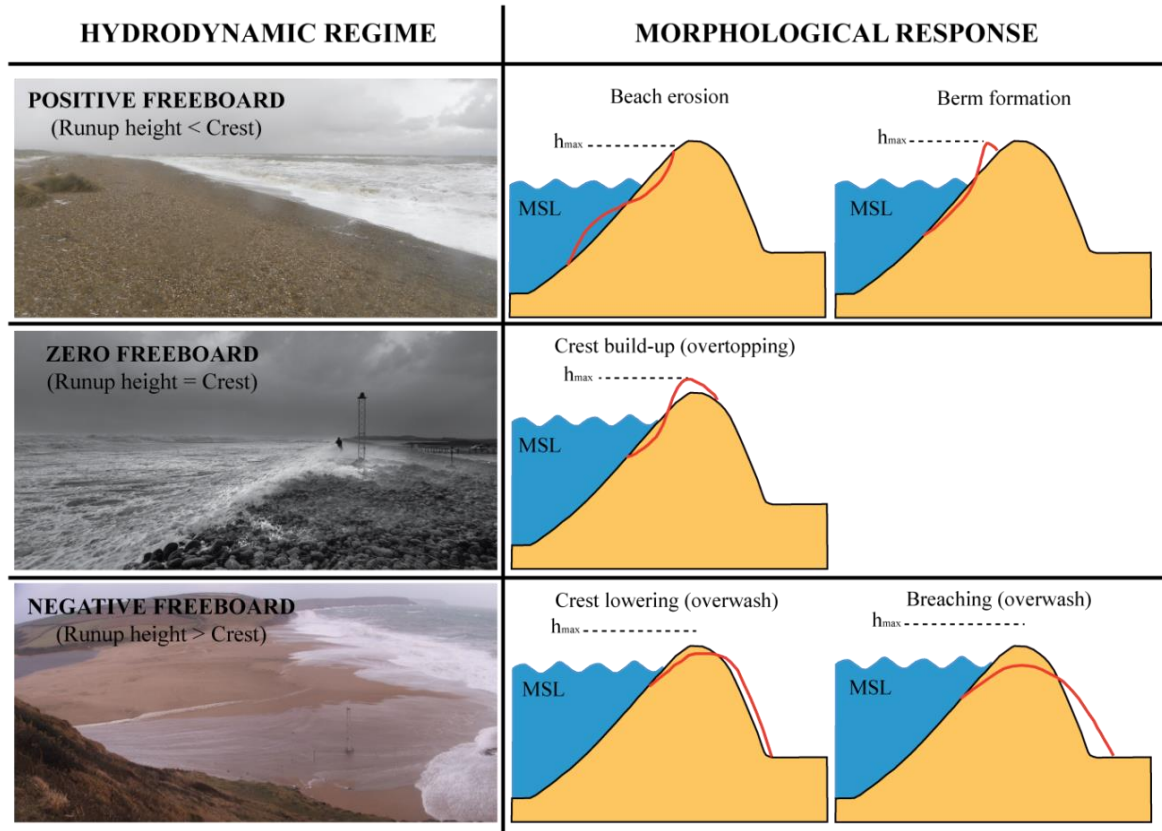


**Figure 1.5** Sketch of the three impact regimes of storms on coarse-grained beaches (adapted from Orford et al., 2003)

### 1.3 Project Aim and Objectives

The aim of the present research project is to investigate the *Swash zone morphodynamics on coarse-grained beaches during energetic wave conditions*, covering the full range of conditions defined by the conceptual storm impact regimes presented in Figure 1.5. To achieve this, the following specific objectives are defined:

- Development and validation of a 2D Laser-scanner methodology to measure swash hydrodynamics and morphological response on coarse-grained beaches during energetic wave conditions.

- Comparison of laser-scanner measurements with traditional field instruments and present a demonstration of the capabilities of this new technique to assess the swash dynamics of a gravel beach during energetic wave conditions.
- Characterize the swash zone morphodynamics and runup of different types of coarse-grained beaches under energetic wave conditions under positive freeboard regime.
  - Measure the swash dynamics during energetic wave conditions in different coarse-grained beaches and assess their morphological response to energetic wave conditions.
  - Explore the relationship between different morphodynamic regimes and extreme runup and quantify the effect of groundwater processes and morphological evolution on the extreme runup of coarse-grained beaches.
- Measure and model the impact of overtopping and overwash events on a gravel barrier (zero and negative freeboard regimes)
  - Measure the morphological response and hydrodynamics of a gravel barrier during overtopping and overwash events with the laser-scanner.
  - Validate XBeach-G hydrodynamics and morphological response with field datasets.
  - Investigate the effect of the groundwater, wave period and wave spectrum shape on the definition of the impact regimes.

## **1.4 Project Structure**

The development of a new technique (2D laser-scanner) to measure the swash zone of coarse-grained beaches during storms is a key element of the present research project, thus it was defined as the first task to be accomplished on the present research project (Chapter 2). The swash zone response during storms was investigated under the full range of hydrodynamic conditions (positive, zero and negative freeboard) using a combination of detailed field measurements, performed with the 2D laser-scanner, and numerical model XBeach-G. Data analysis was divided in two Chapters: Chapter 3) the swash zone response under storms with positive freeboard and Chapter 4) the swash zone response under zero and negative freeboard conditions. Finally the conclusions of each result chapter was combined and discussed together in Chapter 5 and final conclusion of the thesis presented.

A broad outline of the structure of this research project, and the subsequent chapters which make up the thesis is summarised in Figure 1.6.

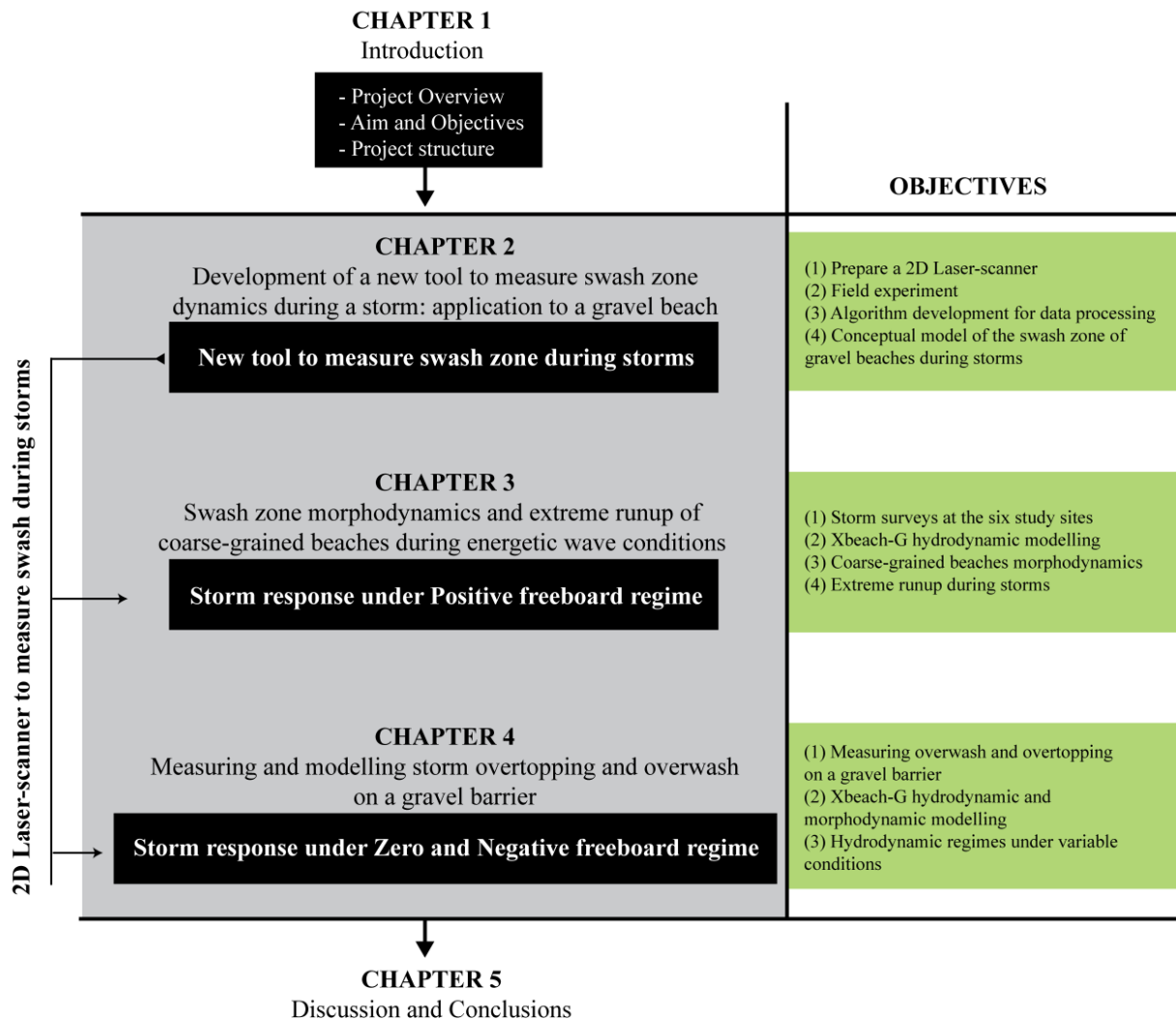


**Figure 1.6** Summary structure of the thesis including the bold objectives (black boxes) and specific objectives (green boxes) of each chapter.

## **2. Development of a new tool to measure swash zone dynamics during a storm: application to a gravel beach**

This chapter presents the development of a new field technique to measure swash zone hydro- and morphodynamics during storms – 2D laser-scanner. Details on how to deploy and process measurements are provided together with the comparison with traditional field techniques. The hydrodynamics and morphological evolution of a fine gravel beach (Loe Bar) under energetic wave conditions is investigated during a tidal cycle and a conceptual morphodynamics model presented. This Chapter is a result of a combination of two journal publications: Almeida et al., 2013, published in *Journal of Coastal Research* and Almeida et al., 2015, published in *Geomorphology*.

### **2.1 Introduction**

Gravel beaches and barriers occur typically along paraglacial coasts (e.g., Canada, UK, Ireland) or coastlines backed by mountains (e.g., Mediterranean, New Zealand), and according to Jennings and Schulmeister (2002) they can be found in nature mainly in three different forms: (1) pure gravel beach; (2) mixed sand and gravel; and (3) composite gravel beach. Pure gravel beaches (hereafter referred as ‘gravel beach’) are characterised by steep reflective profiles and prominent secondary morphological features, such as ridges, berms, step and cups, but without nearshore bars (Buscombe and Masselink, 2006). During highly energetic wave conditions (e.g., storms), gravel beaches typically dissipate most of the offshore wave energy across a narrow cross-shore section next to the swash zone (Buscombe and Masselink, 2006; Ruiz de Alegria-Arzaburu and Masselink, 2010;



Poate et al., 2013). The absence of an offshore bar promotes large collapsing/plunging waves to break on the lower beach face (step) creating extremely energetic boundary conditions for swash motions and enhancing highly turbulent flows capable of mobilizing significant amounts of gravel at individual swash time scales (Austin and Masselink, 2006; Austin and Buscombe, 2008; Masselink et al., 2010). Under such energetic conditions, the complex interactions between the swash hydrodynamics and the beach morphology dictate the occurrence and extension of hazardous events like barrier overtopping or overwashing (Orford et al., 2003 and Matias et al., 2012). The acquisition of full-scale, hydro- and morpho-dynamic measurements is essential in order to provide new insights into the fundamental processes driving coastal change, overtopping and flooding. However, the deployment of any kind of *in-situ* measurements in such energetic conditions is extremely challenging. Of particular importance to the study of sediment transport in the swash zone is the development of instruments with the ability to acquire reliable measurements of both swash hydrodynamics and bed changes at wave-by-wave time-scales.

Recently, a method based on ultrasonic technology brought the innovative capability to quantify bed changes and water motions at a frequency of individual uprush-backwash events with the accuracy of  $\pm 1$  mm (Turner et al., 2008). This method is typically mounted on a scaffold frame with a large number of ultrasonic units (bed-level sensors - BLS), equally spaced at a certain elevation ( $\sim 1.5$  m) from the bed, allowing the acquisition of the bed changes, swash position and volume at 4 Hz (Turner et al., 2008). The capability of this method has been very well demonstrated in several field (e.g., Masselink et al., 2009, 2010; Blenkinsopp et al., 2011; Poate et al., 2013) and laboratory applications (e.g., Masselink and Turner, 2012; Williams et al., 2011; Masselink et al., 2013).

A limitation of having to use a large scaffold frame for mounting the large number of sensors required to obtain data of sufficient spatial coverage is that the methodology is only possible for mild wave conditions. This logistical problem is exacerbated on gravel beaches where typically most of the offshore wave energy is dissipated over the swash zone and the breaker region just seaward of the swash zone (Buscombe and Masselink, 2006; Ruiz de Alegria-Arzaburu and Masselink, 2010; Poate et al., 2013).

Remote sensing methods emerge in this context as the most appropriate solution for this type of field measurements, especially under energetic wave conditions that lead to the most dramatic morphological changes. During the last three decades video imaging has been the most applied remote sensing method to nearshore surveying. The estimation of intertidal topography (e.g., Plant and Holman, 1997), nearshore bar location (e.g., Lippmann and Holman, 1989) or subtidal bathymetry (e.g., Stockdon and Holman, 2000) are all examples of the wide variety of applications that video can offer. Video data are also extensively used in runup studies and several runup parameterizations (e.g., Holman, 1986; Stockdon et al., 2006) are based on video measurements. Despite the high spatial and temporal resolution video runup data can offer, video imaging does present some significant limitations regarding their use during storms, such as the inability to record useful data during low light (e.g., during the night) or rainy and foggy conditions (typical conditions during storms). In addition, conversion of video data from image coordinates to real-world coordinates requires information on the beach morphology and this is not a constant during a storm.

Recent studies reporting the use of laser-scanners on natural beaches (Blenkinsopp et al., 2010; Brodie et al., 2012; Almeida et al., 2013) and laboratories (Blenkinsopp et al., 2012) have demonstrated the ability of the laser technology to measure swash hydrodynamics, as well as bed evolution, on the swash event time scale remotely (i.e., without the need to deploy the instrument

within the region of interest). The versatility and precision of 2D laser-scanners has enabled the development of a large range of useful non-contact measurement applications ranging from medicine (e.g., Palleja et al., 2009), forestry (e.g., Miettinen et al., 2007), to robotics (e.g., Vásquez-Martín et al., 2009). Using a simple ‘time of flight’ working principle to compute the distance between the laser sensor and the ‘target’, this method allows the acquisition of high-frequency and fine spatial resolution measurements along a swath line within the laser beam range.

Comparison between 2D laser-scanner and state-of-the-art instrumentation, such as ultrasonic altimeters or video cameras are scarce and only present in preliminary tests performed during mild hydrodynamic conditions (Blenkinsopp et al., 2010, 2012). The lack of field comparisons together with the lack of important methodological details on aspects such as the instrument deployment and data processing represent a significant limitation for the systematic application of this method in the field.

The aim of the present chapter is to provide a guidance on how to deploy a 2D laser-scanner in the field to collect high-frequency topographic and hydrodynamic data from the swash, together with methods to process the raw laser measurements. Comparison of the laser-scanner measurements with state-of-the-art instrumentation is presented and to demonstrate the capabilities of this instrument its also presented an detailed analysis of the morphodynamics of a gravel beach (Loe Bar, UK) during an representative energetic tidal cycle.

## 2.2 Methods

### 2.2.1 Study site and field deployment

A field experiment was conducted between 23 February and 28 March 2012 at Loe Bar in the southwest of England (Fig. 2.1) with the aim of monitoring the response of a gravel beach to varying wave conditions (cf. Poate et al., 2013). Loe Bar is part of a 4.3-km long gravel beach ( $D_{50} = 2\text{--}4\text{ mm}$ ) that extends from Porthleven, in the north, to Gunwalloe, in the south (Figure 2.1).

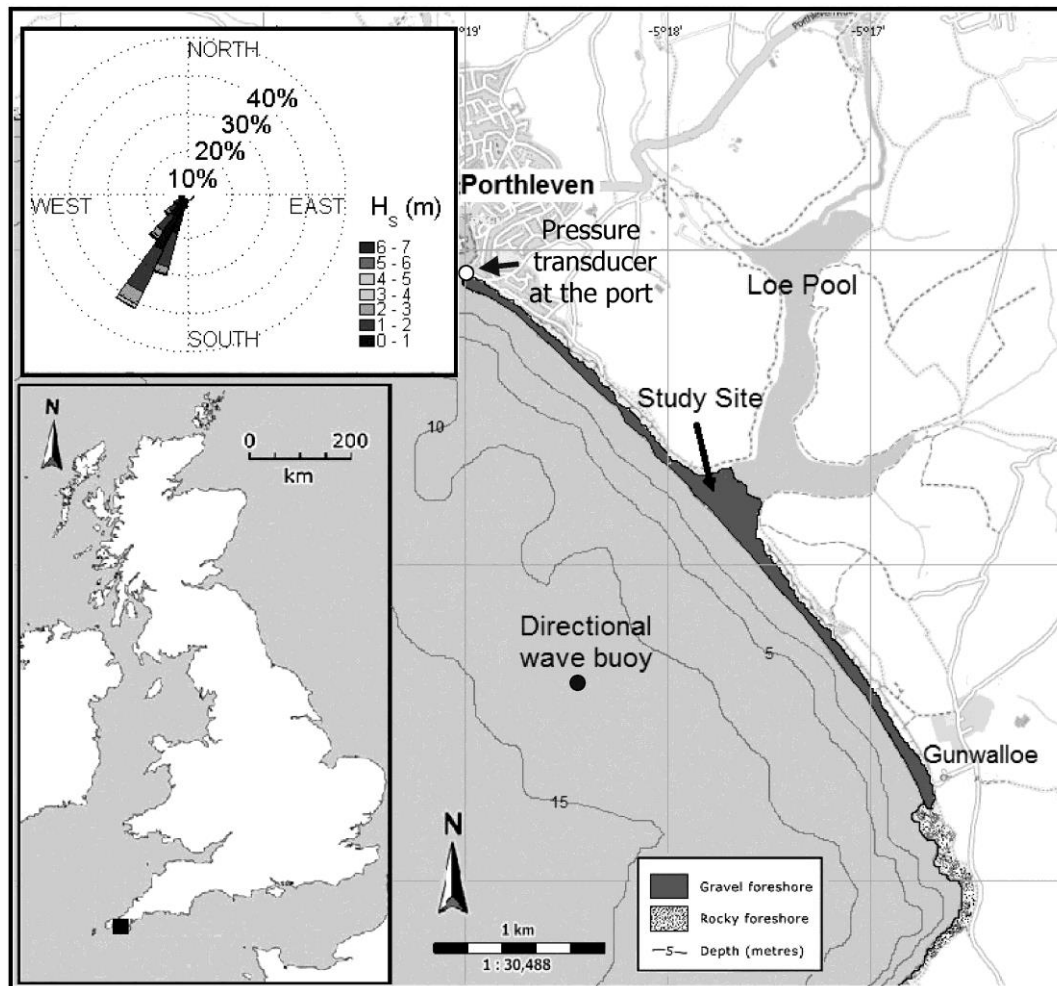


**Figure 2.1** Map showing the location of the study site (Loe Bar), the location of the offshore wave buoy and bathymetry. The wave rose represents 1 year (from October 2011 to October 2012) of directional wave buoy data.

Loe Bar barrier fronts Loe Pool and extends 430 m between the adjacent headlands, with an average width of 200 m and a typical seaward gradient of 0.1. With a NW-SE shoreline orientation, the barrier faces south-west and is exposed to energetic Atlantic swell with an annual average significant wave height ( $H_s$ ) of 1.2 m, an average peak period ( $T_p$ ) of 9.1 s and a direction ( $\theta_{wave}$ ) of 235° (wave statistics were derived from Porthleven wave buoy measurements from October 2011 to October 2012; data it can be freely downloaded at <http://www.channelcoast.org>).

The tidal regime is macrotidal with MHWS (mean high water spring) and MLWS (mean low water spring) at, respectively, 2.5 m and -2.2 m ODN (Ordnance Datum Newlyn; 0 m ODN ~ 0.2 m above mean sea level in UK coastal waters).

A 2D laser-scanner (SICK - LD-OEM3100) was deployed on the top of an aluminium tower (5.2 m high), fixed to a scaffold frame inserted into the beach around the high tide runup level and stabilized by guy ropes (Figure 2.2). External power supply (28 volts) is provided to the scanner during operation and measurements are streamed to a laptop, by an RS422 cable, where data are recorded using SOPAS (SICK) software interface.

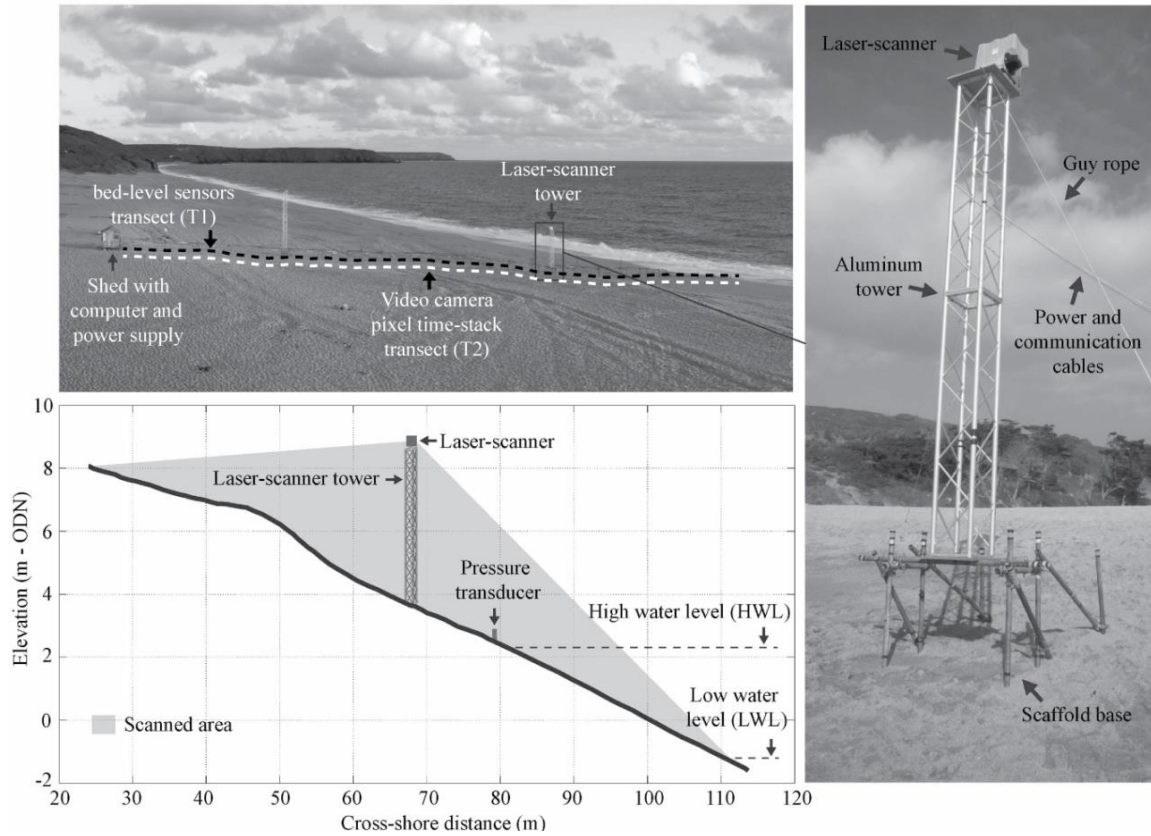


**Figure 2.2** Photos showing the deployment of the laser-scanner tower in the field (top and right panels), with the indication of the video camera pixel time-stack transect (T2) and bed-level sensors transect (T1). Lower left panel shows the beach profile with locations of the equipment used during the survey.

Two cross-shore transects (T1 and T2) alongshore spaced by 5 m were established at the central area of the barrier (Figure 2.2). On T1 an array of 45 bed-level sensors mounted on a large scaffold frame (70 m long and 2.5 m wide) was deployed from the MHWS to the crest of the bar (Figure 2.3). Following the methodology outlined by Turner et al. (2008), the sensors were mounted ~ 1.5 m above the bed with cross-shore spacing of 1.5 m (Figure 2.3) and programmed to record at 4 Hz.

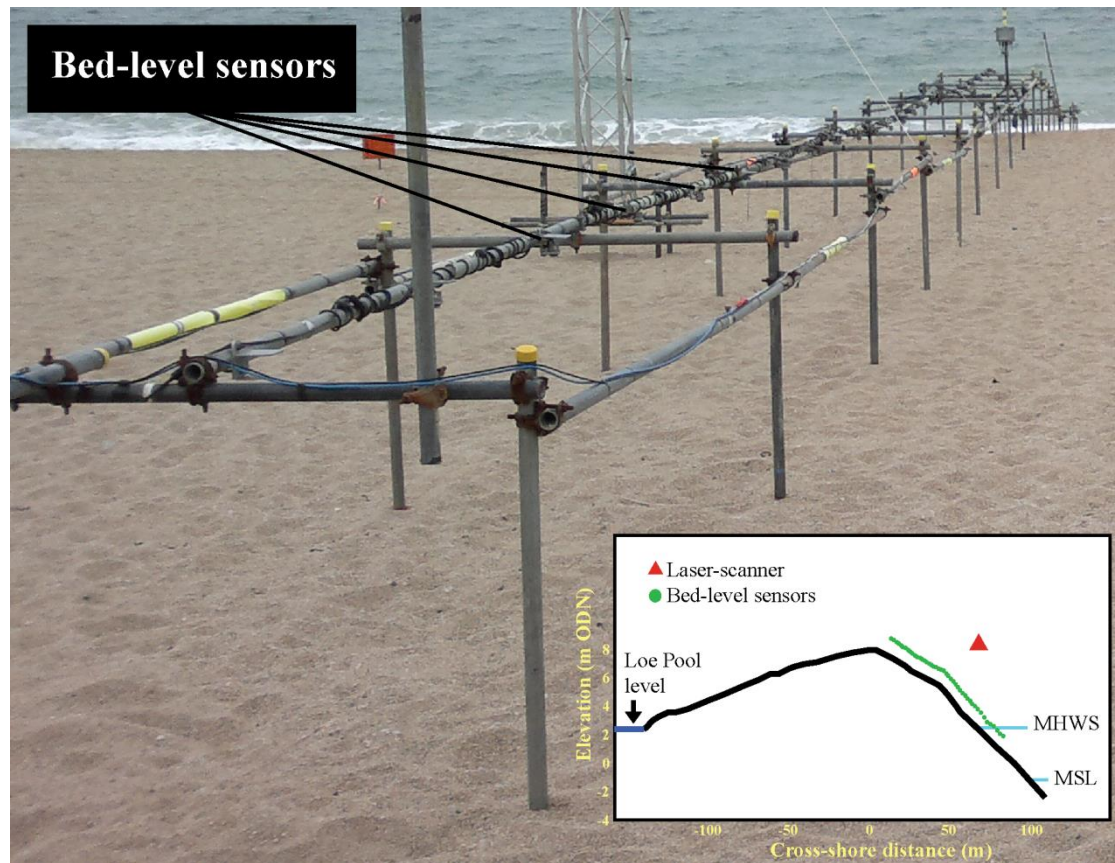


**Figure 2.3** Photo showing the scaffold frame with ultrasonic bed-level sensors covering of the gravel barrier.

On T2 the 2D Laser-scanner and one video camera, deployed at the top of the headland, logged swash dynamics during the entire experiment. A Pointgrey Grasshopper 2MP CCD camera with a zoom lens (25 mm) was programmed to collect pixel time stacks (15 minutes duration) every 30 minutes at 3 Hz.

Topographic surveys were undertaken every low tide using real-time kinematic DGPS (RTK-DGPS – Trimble 5800) along the T1 and T2 transects and using a local coordinate system, where the cross-shore origin ( $x = 0$ ) is at the top of the barrier and the vertical datum is referred to the Ordnance Datum of Newlyn (ODN).

A pressure transducer was deployed just above high water level (Figure 2.2) to measure swash/wave conditions (at 4 Hz) in the lower swash zone during mid and high tide conditions, and offshore wave conditions were measured by the Porthleven directional wave buoy located in approximately 15 m water depth at low tide (Figure 2.1). Tide measurements were performed at Porthleven port (Figure 2.1) by a pressure transducer deployed around the MLWS level.

### **2.2.2 2D Laser-scanner and working principle**

The LD-OEM3100 laser scanner model was selected for the present work. This model is a two-dimensional mid-range (maximum range  $\approx 100$  m; SICK, 2009) laser-scanner that emits pulsed laser beams (infrared light;  $\lambda = 905$  nm) that are deflected on an internal mirror (inside the scanner head) that rotates at regular angular steps and scans the surroundings ( $360^\circ$ ) in a circular manner (Figure 2.4). The scanner head rotates at 2.5 Hz with an angular resolution of  $0.125^\circ$  and the distance to the target is calculated from the propagation time that the light requires from emission to reception of the reflection at the sensor.



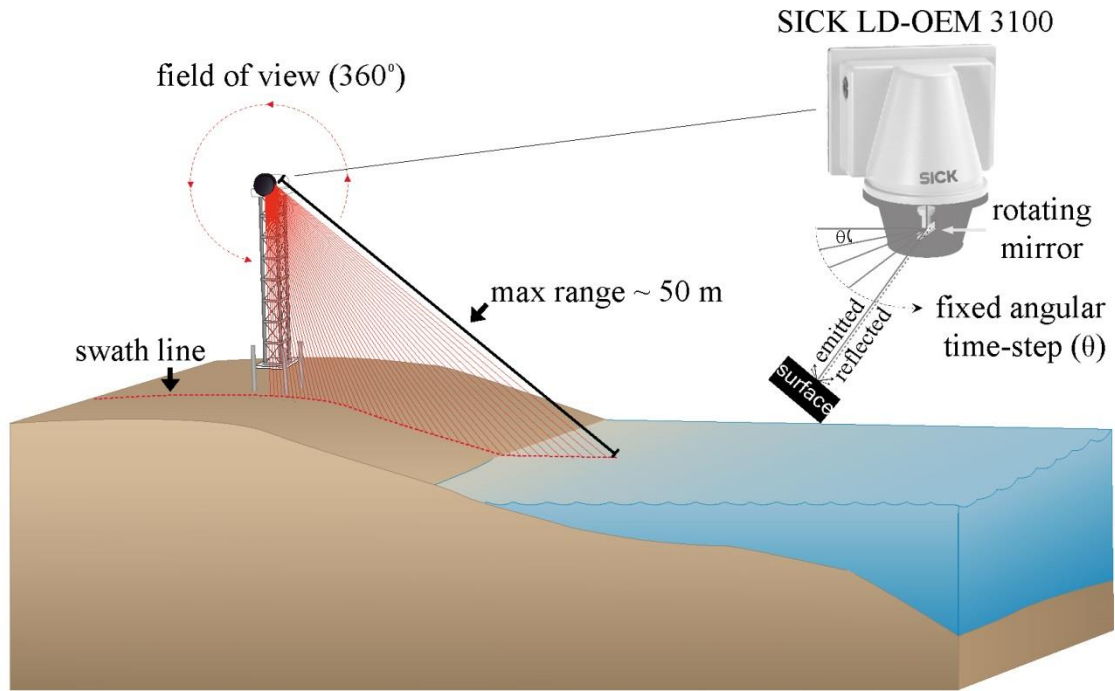


**Figure 2.4** Diagram of the 2D laser-scanner LD-OEM3100 (SICK) showing working principles in the field.

The measurements are logged at 2.5 Hz and consist of two dimensional polar coordinates  $(d_i, \alpha_i)$ , where  $i$  is the scan number (complete cycle of scanner field of view),  $d$  is the distance measured between the laser-scanner and the target and  $\alpha$  is the relative angle of the measurement. The number of measurements per scan is given by the scan angle divided by the angular resolution, e.g., for a scan angle of  $120^\circ$ , the number of measurements is 960.

## 2.3 Results

### 2.3.1 Processing and validation of Laser-scanner measurements

#### 2.3.1.1 Correction of the laser measurements position and orientation

Laser polar measurements ( $d_i$ ,  $\alpha_i$ ) are initially converted to Cartesian coordinates ( $x_i$ ,  $z_i$ ), where  $x$  is the cross-shore position and  $z$  elevation, by applying a polar transformation.

It is extremely difficult in the field to deploy the laser tower perfectly vertical; therefore, the laser measurements are characterised by an orientation offset with respect to ground level. A beach profile derived from the laser scanner data will therefore have inaccuracies when compared with the real profile (Figure 2.5).

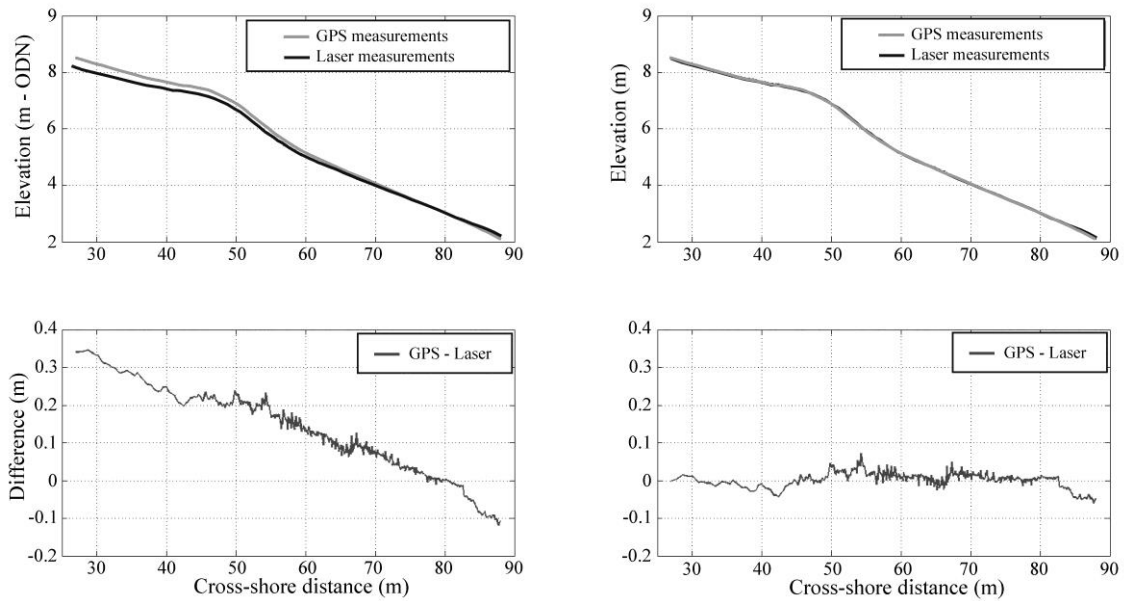


**Figure 2.5** Comparison between laser-derived beach morphology and that measured using dGPS. Upper panels show comparison between dGPS profile and raw laser-derived profile (upper-left panel) and between dGPS profile and laser-derived profile corrected for mis-orientation and translation (upper-right panel). The lower panels show the associated residuals (difference between dGPS profile and laser-derived profile).

To correct this orientation problem, the Horn's quaternion-based method for absolute orientation (Horn, 1987) is implemented. This method minimizes the sum of the squared distances between two datasets of points, and for the present purpose the laser measurements were corrected using differential DGPS (dGPS) measurements (performed on the swath line of the laser) by applying the following equation:

$$\sum_{j=1}^n \|r(X_{laser_j}, Z_{laser_j}) + t - (X_{gps_j}, Z_{gps_j})\|^2 \quad (2.1)$$

where  $r$  is the unknown rotation matrix (due to orientation problem) and  $t$  the unknown translation vector (position of laser coordinate system relative to that of local DGPS coordinate system),  $X_{laser_j}$  and  $Z_{laser_j}$  are the laser coordinates,  $X_{dGPS_j}$  and  $Z_{dGPS_j}$  are the DGPS coordinates, and  $j = 1 \dots n$  represent the number of points.

As evident from Figure 2.5, after applying equation 1 to the laser measurements, this angular offset is eliminated and the remaining residuals are within the accuracy of the dGPS (approximately  $\pm 5$  cm in vertical).

### 2.3.1.2 Scanning coverage and horizontal resolution

With the present deployment (5.2 m tower elevation) the laser-scanner covered approximately 90 m of a cross-section of the beach with an average horizontal resolution of 6 cm (Figure 2.6). On the upper and lower part of the profile (landward from the berm crest and lower shoreface) the horizontal resolution was lower (between 20 cm and 1 m), due to the low angle of incidence that increased significantly the space between measurements (Figure 2.6). Better average horizontal

resolution could be attained by lowering the laser-scanner tower (e.g., 1 m elevation – see Figure 2.6), although this would reduce dramatically the number of measurements on the top of the berm and on the bottom of the shoreface, reducing the scanning coverage.

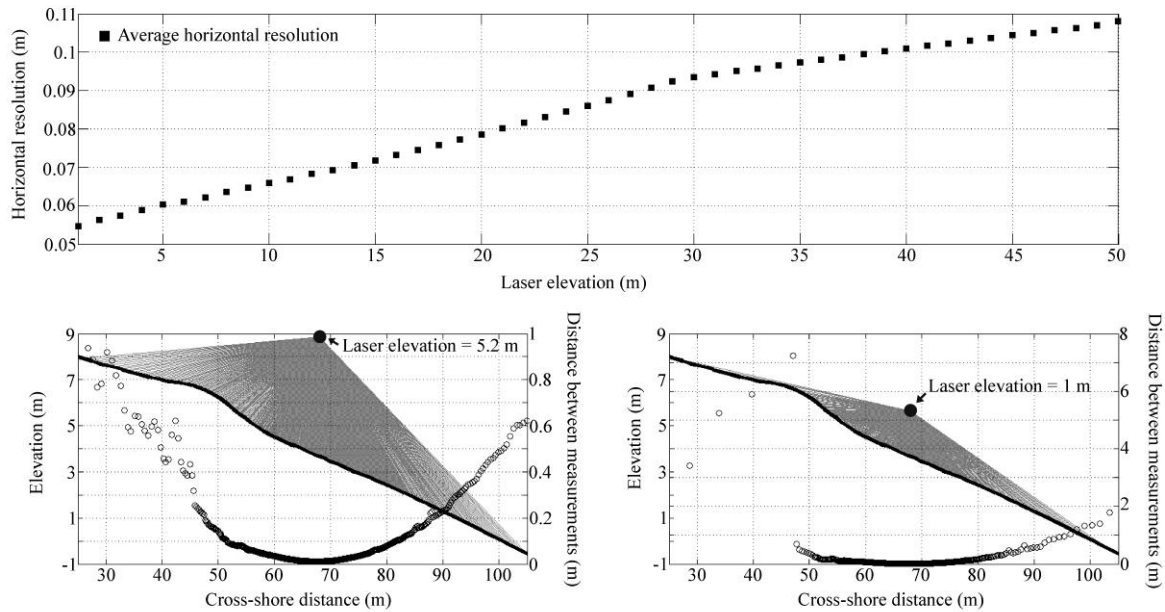


**Figure 2.6** Average horizontal resolution of the laser-scanner measurements computed for different tower elevations, assuming 0.125 angular resolution and the same cross-shore position (top panel). Example of the laser-scanner horizontal resolution (black dots) computed for the laser-scanner beams (grey lines) using different laser-scanner elevations (5.2 – bottom left panel; and 1 m – bottom right panel).

By elevating the laser-scanner tower, the swath line coverage would increase, although reducing the horizontal resolution. In this case the distance would affect the angular step (e.g., with the same angular step the horizontal resolution decreases with distance) and reduce the horizontal resolution, although other problems such as the tower stability or the reduction of the power of the reflected beam (Pallejà et al., 2009) would affect the measurements with the raised tower. For all these reasons the present tower elevation and cross-shore location was found to be optimal for data collection on the swash zone of this site.

### 2.3.1.2 Separation between bed level and water surface

The raw laser measurements represent reflection of the laser beams from the beach topography as well as the water surface, without any distinction between the two (Figure 2.7).

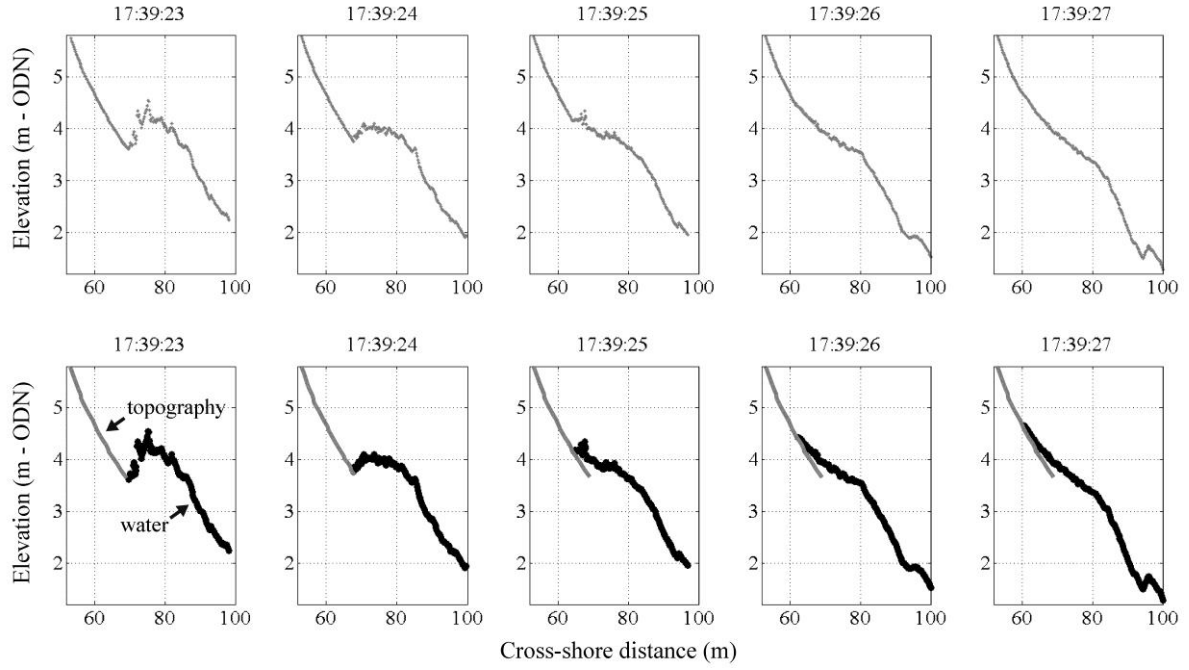


**Figure 2.7** Raw laser-scanner measurements without the separation between beach topography and water (top panels), and after applying the separation methods (lower panels).

To separate topography from the water at each cross-shore position, and over time, a moving-average time window with a variable variance threshold is applied to all measurements (equation 2.2).

$$Z_{topo}(\Delta t) = \overline{Z_{laser}(\Delta t)} \quad \text{if} \quad \sigma^2(Z_{laser}(\Delta t)) \leq \sigma_{threshold}^2 \quad (2.2)$$

where  $\Delta t$  is the time window length (4 s – period of time required for the natural variance of the signal to stabilize after the passage of a wave, defined empirically),  $\sigma^2_{threshold}$  is the variance threshold (see next section).

This method of separating the stationary bed level from the non-stationary water surface (wave or swash) is similar to that used by Turner et al. (2008) for data collected using ultrasonic bed-level sensors (BLS). The time-varying vertical position of the water's edge on the foreshore of the beach (runup) is then obtained by subtracting the extracted topography ( $Z_{topo}$ ) from the raw measurements ( $Z_{laser}$ ), and using a threshold water depth (0.02 m) to define the instantaneous shoreline. By applying this separation method, the raw laser measurements are separated in two distinct time series of topographic measurements and hydrodynamics (Figure 2.6), and can then be independently analysed.

### **2.3.1.3 Defining the separation threshold**

Following Turner et al. (2008), a 40-min segment of laser measurements was analysed in order to perform an adequate selection of the variance threshold in equation 2 (Figure 2.8). The selected data were obtained from a section of the beach profile landward of the swash zone and it can be assumed that no morphological change occurred over that period (Figure 2.8).

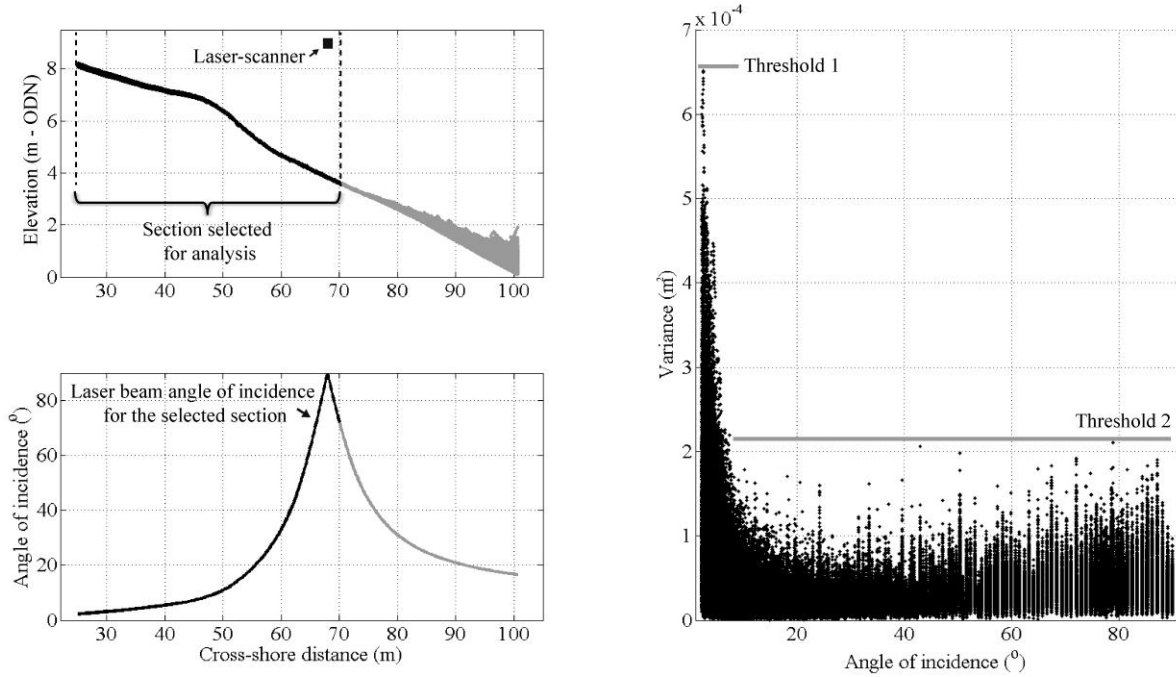


**Figure 2.8** Section of the beach profile analysed during 40 minutes of laser-scanner measurements and the respective angles of incidence (left panels); variance computed for each angle of incidence (right panel). The two horizontal lines in the right panel represent the two variance thresholds computed for two groups of angles of incidence.

The variance was computed for segments of 4s ( $\Delta t$  used in equation 2) of measurements and for different angles of incidence of the laser beam within the selected section of the profile (Figure 2.8). The results of this analysis indicate that for low angles of incidence ( $< 7^\circ$ ) the variance of the measurements increases significantly compared with the variance observed for large angles of incidence ( $> 7^\circ$ ).

Based on these results two variance thresholds were defined:  $6.6 \times 10^{-4} \text{ m}^2$  for angles  $< 7^\circ$ ; and  $2.2 \times 10^{-4} \text{ m}^2$  for angles  $> 7^\circ$ . These values are used in equation 2 to separate the stationary bed level from the non-stationary water surface. Because these thresholds are likely to depend on the nature of the bed material and the averaging interval, this procedure should be carried out for every deployment.

#### 2.3.1.4 Comparisons between laser-scanner measurements and state-of-the-art techniques

To evaluate the capabilities of the 2D Laser-scanner on the collection of swash morpho- and hydrodynamics a set of field measurements performed with state-of-the-art instrumentation (video cameras, bed-level sensors and dGPS) were used to compare with the processed laser measurements. Figure 2.9 shows the observed offshore wave conditions (measured by Porthleven wave buoy) and tide (measured at Porthleven harbour) during the period of time where coincident measurements were performed with all the instruments.

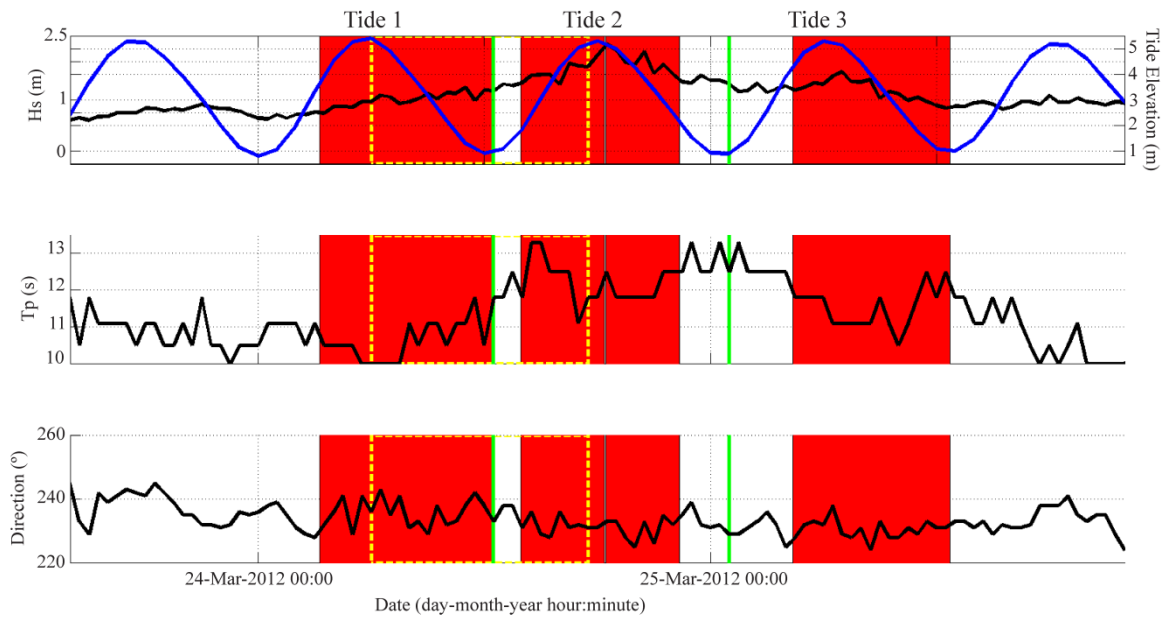


**Figure 2.9** Offshore wave conditions (black line) and tide (blue line) for the survey period with the indication of measurements performed with the different instruments: DGPS (green vertical lines); laser-scanner and bed level sensors (red areas); video (box with yellow dashed line);

Offshore wave observations indicate that during the three measured tides the maximum  $H_s$  reached 2.5 m (Tide 2) with a peak of period of approximately 12 seconds from SW direction (waves approaching the shore with a perpendicular angle).

The comparisons of the DGPS surveys with the bed level sensors and laser-scanner measurements (Figure 2.10) indicate that both remote sensing instruments present a very good agreement with the



*in-situ* measurements performed with the DGPS. The obtained residuals (Figure 2.10) did not present bias and show that the computed differences are within the order of magnitude of the DGPS accuracy ( $\pm 5\text{cm}$ ). The highest residual was obtained between the laser-scanner and DGPS for Tide 2 on the lower beach face (between  $x = 85\text{m}$  and  $x < 100\text{m}$  – see Figure 2.10). This result is likely to be due to the fact that the topography measured with the laser-scanner and used to compare with the DGPS measurement for Tide 2 was collected before the tide had completely retreated, whereas the DGPS data were collected at low tide. The difference between the bed-level sensors and laser-scanner topographies are very low until approximately the cross-shore position  $x = 40\text{m}$ , and increase towards the lower part of the beach.

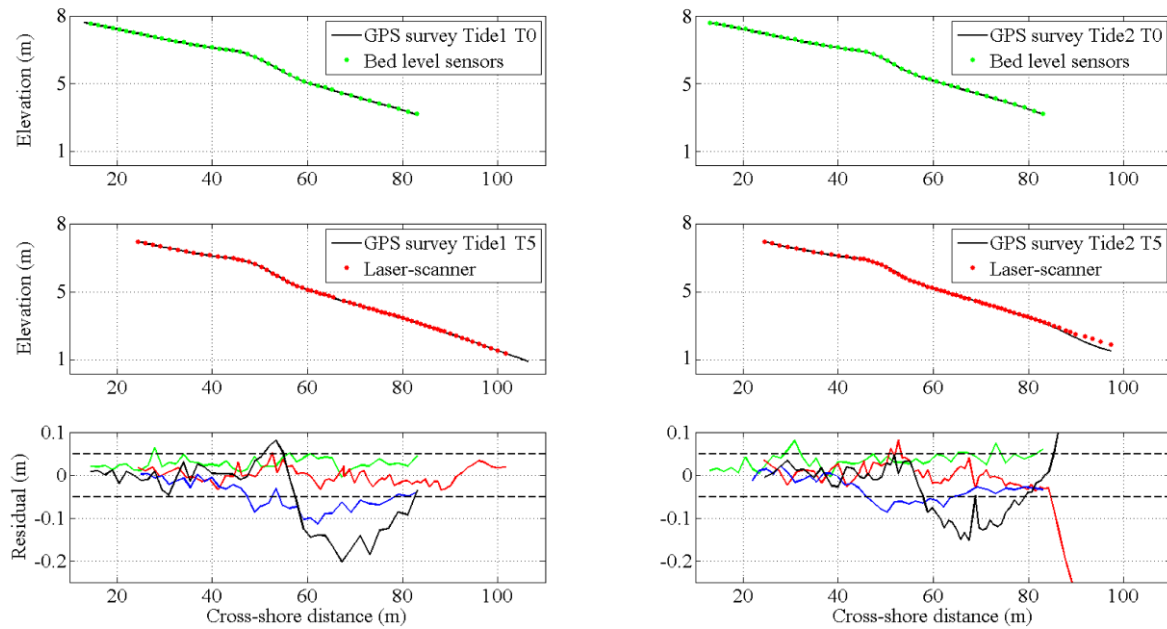


**Figure 2.10** Comparison between DGPS measurements made on T0 and bed level sensors for the tides 1 and 2 (two figures on the top); comparisons between DGPS measurements made on T5 and the laser-scanner scan for the tides 1 and 2; residual between all the instruments: DGPS vs bed level sensors (green line), DGPS vs laser-scanner (red line), Laser vs bed level sensors (blue line) and DGPS vs DGPS (black line) (lower figures).

This trend can be observed for both tides and is attributed to alongshore variations in the beach profile because the profiles were measured in different locations (see Figure 2.2). To support this

suggestion, Figure 2.10 presents the differences between the DGPS surveys taken at along different alongshore transects and which shows the same trend in the cross-shore differences.

A proxy of the extreme runup, the 2% of exceedance of the runup maxima ( $R_{2\%}$ ), was chosen to evaluate the performance of the 2D Laser-scanner hydrodynamic measurements. This statistical parameter was computed following the method presented by Stockdon *et al.* (2006), and using 15 minutes of coincident runup measurements performed with the laser-scanner and video camera.

The computed  $R_{2\%}$  for both video and laser-scanner runup datasets are presented in Figure 2.11. Despite some occasional differences where the residual exceeds 0.5 m both instruments present similar temporal trends. The good correlation between both  $R_{2\%}$  datasets ( $r^2 = 0.7$  and  $rmse = 0.26\text{m}$ ) consolidates the general good agreement that both instruments present in quantifying the runup evolution over time.

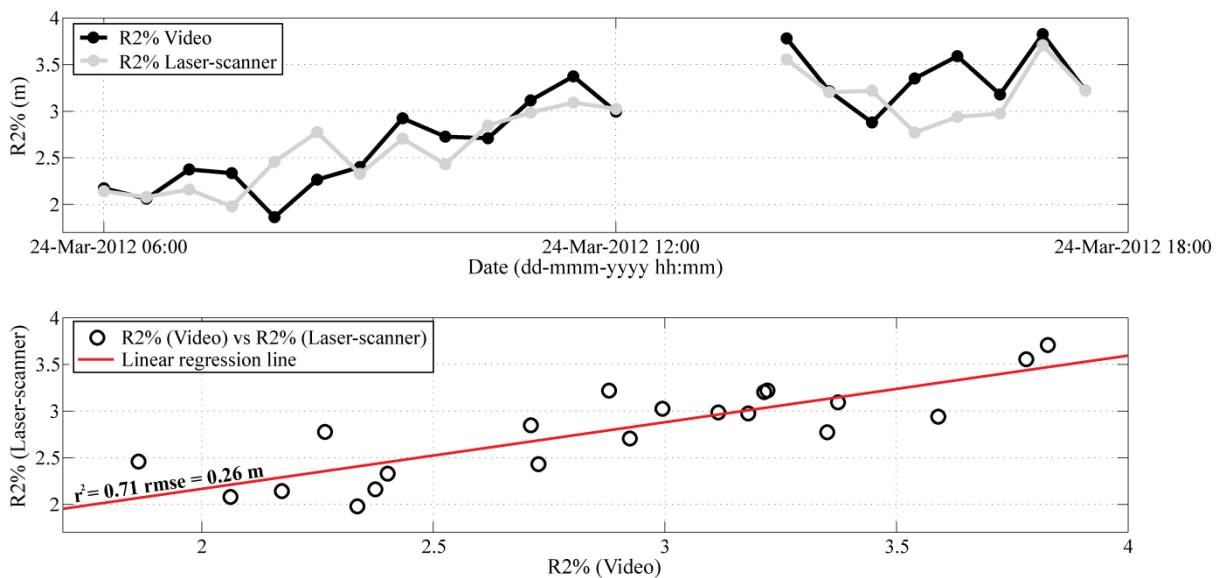


**Figure 2.11** Comparison between the  $R_{2\%}$  computed with the laser-scanner and video camera (upper panel); scatter diagram of the measured  $R_{2\%}$  with video vs.  $R_{2\%}$  measured with Laser-scanner (bottom panel), with the linear regression line (red line).

## 2.3.2 Insight into the swash zone morphodynamics of gravel beach

### 2.3.2.1 Wave and tide records

To demonstrate the capability of the 2D Laser-scanner to investigate the dynamics (both morphological response and hydrodynamics) of gravel beaches during energetic wave conditions one tide cycle of measurements was selected (Tide 2 - the most energetic tide) to develop detailed analysis.

Field measurements obtained during Tide 2 covered the peak of an energetic swell event (Figure 2.12) on 24 March 2012. The offshore wave conditions observed at the peak of the event showed waves from the southwest with significant wave height ( $H_s$ ) of 2.5 m and a peak period ( $T_p$ ) of 12 s (Figure 2.12). This event occurred during spring tides (tidal range of approximately 4 m) and the maximum offshore wave conditions occurred just after high tide (Figure 2.12).

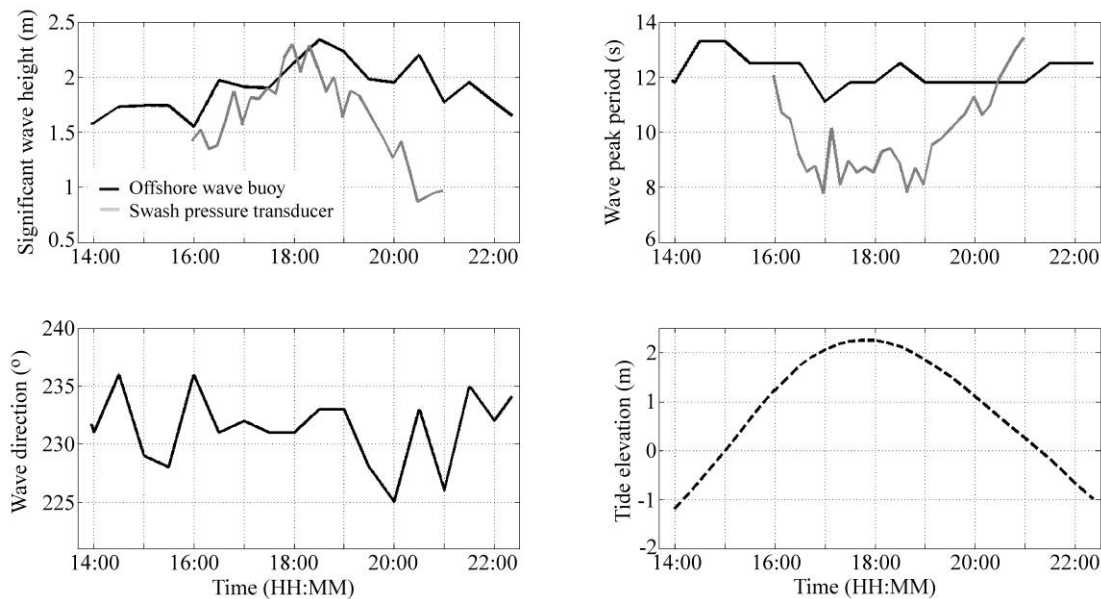


**Figure 2.12** Time series of significant wave height (upper left panel), peak wave period (upper right panel), wave direction (lower left panel) and tide elevation (lower right panel). Solid black lines represent offshore wave conditions measured by the offshore wave buoy, solid gray lines are measurements made by the pressure transducer on the beach deployed just above high tide level, and the dashed line represents tide measurements performed at Porthleven by a pressure transducer deployed around the MLWS level.

Also shown in Figure 2.12 are comparative wave statistics measured in the swash zone obtained from the PT sensor deployed around the MLWS level. These show a strong tidal modulation of  $H_s$  and  $T_p$  relative to the offshore values. During mid-tide, the PT was in the mid to lower swash zone and mainly recorded large swash bores with the occasional breaking wave. The larger  $T_p$  values observed at this tidal stage are therefore due to the low-pass filtering effect that the breakpoint (Waddell, 1973) has on the offshore boundary of the swash. During high tide, the PT sensor was located at the transition of the lower swash and breakpoint, and recorded mostly breaking waves. Therefore, at this tidal stage every wave was recorded and  $H_s$  was larger and  $T_p$  shorter than the offshore measurements.

### 2.3.2.2 Data analysis

Swash hydrodynamics measured by the laser-scanner were analysed through the calculation of the following statistical parameters from the runup elevation time-series ( $R$ ): (1) 2% exceedence of the runup maxima ( $R_{2\%}$ ); (2) standard deviation of the vertical runup ( $R_\sigma$ ); (3) runup vertical excursion ( $R_{exc}$ ); (4) runup spectra; and (5) swash flow velocity skewness ( $\langle u^3 \rangle$ ) computed as:

$$\langle u^3 \rangle = \frac{\langle u^3 \rangle}{\langle u^2 \rangle^{1.5}} \quad (2.3)$$

where  $u$  is the cross-shore instantaneous velocity of the runup edge, computed through the first derivative of the runup elevation time series (Figure 2.13).

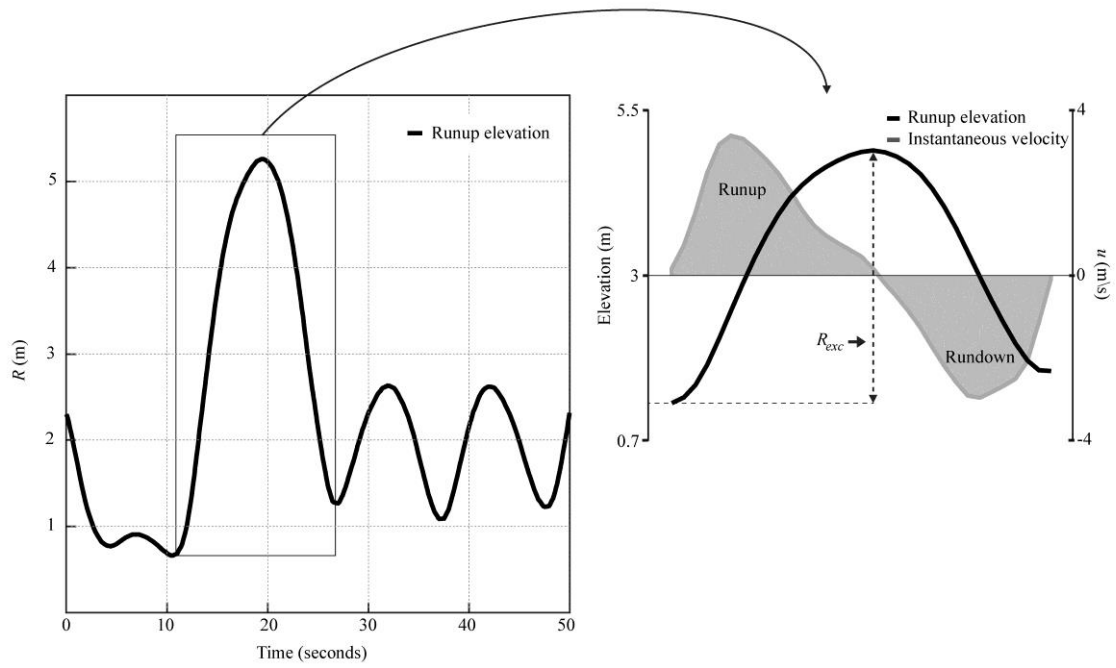


**Figure 2.13** Time series of runup elevation ( $R$ ) and explanation for deriving swash instantaneous velocities ( $u$ ) and vertical runup excursions ( $R_{exc}$ ).

Wave dependence was removed from the first three runup parameters ( $R_{2\%}$ ,  $R_{\sigma}$  and  $R_{exc}$ ) by normalizing by the significant offshore wave height.

Swash morphological response was analysed by computing: (1) cumulative vertical difference between consecutive beach profiles measured with the laser-scanner; (2) beach gradient (slope of the region constrained by the upper runup and lower rundown limit); and (3) maximum elevation of the step deposit (maximum elevation of the deposition recorded in the lower swash zone). All hydrodynamic and morphological parameters were computed for continuous segments of 15 minutes of data.

### 2.3.2.3 Swash hydrodynamics

The complete  $R$  time series derived from the laser-scanner data includes 4 hours at either side of high tide and is presented in Figure 2.14.

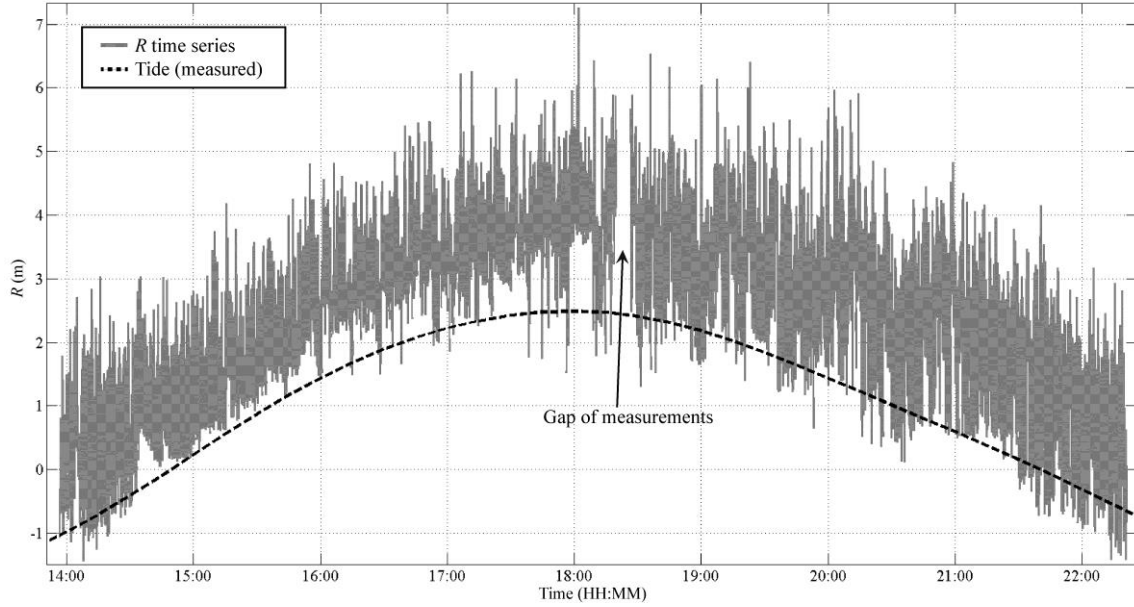


**Figure 2.14** Time series of runup elevation ( $R$ ) measured by the laser-scanner (gray line) during Tide 2 and the measured tide elevation (dashed black line).

The  $R$  was obtained by corresponding the instantaneous shoreline (or the water's edge) to the cross-shore elevation at each time step. At first inspection, the runup motion during the rising tide appears less dynamic than during the falling tide. This tidal asymmetry is explored further below using runup statistics computed over 15-min data segments (Figure 2.15).

The normalized 2% exceedence of the runup maxima ( $R_{2\%}/H_s$ ) show some variation over time with lower values ( $< 1.7$ ) occurring between the mid rising and high tide (between 16:30 and 19:00), higher values ( $> 2.1$ ) mainly around the falling tide (between 19:00 and 22:30), but with also some peaks during the rising tide. The velocity skewness ( $\langle u^3 \rangle$ ), which is considered an indicator of the potential sediment transport direction, varied greatly during the entire tide cycle (Figure 2.15).

Strong runup dominance occurred during the initial rising tide phase (from 14:00 to 16:00), followed by an hour and half of short periods of alternated flow direction dominance (first rundown and after runup).

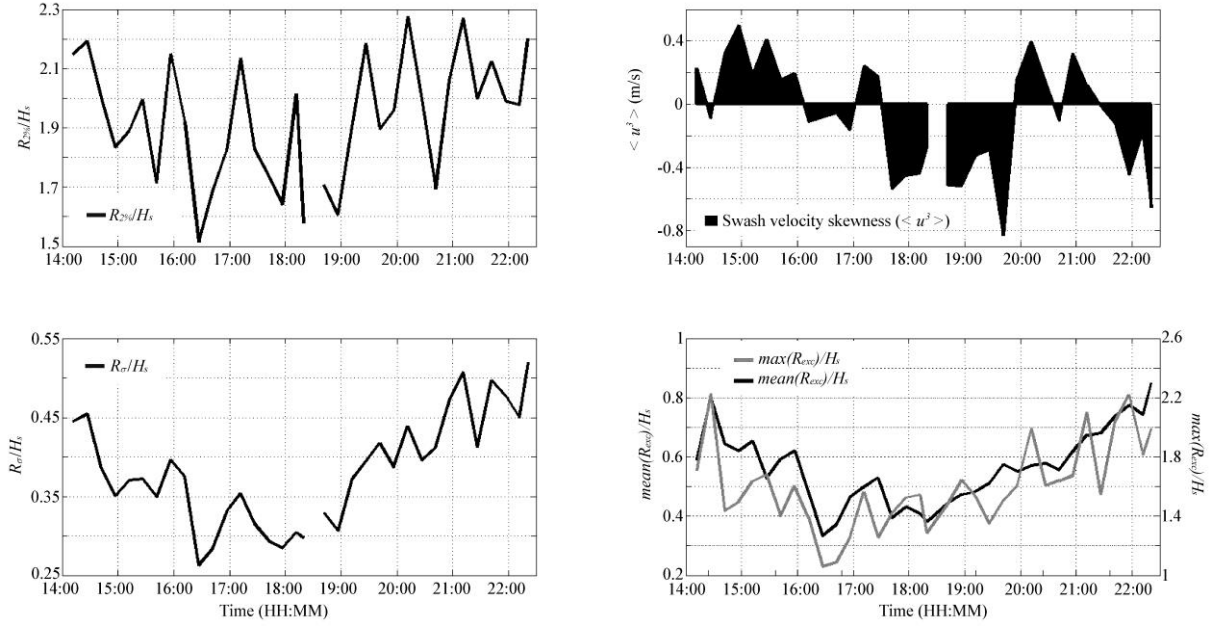


**Figure 2.15** Swash hydrodynamics calculated from the laser-scanner measurements: the normalized 2% exceedence of the runup maxima ( $R_{2\%}/H_s$  - top left panel), swash velocity skewness ( $\langle u^3 \rangle$  - top right panel), normalized runup standard deviation ( $R_{\sigma}/H_s$  - bottom-left panel), and normalized mean and maximum runup vertical excursions ( $mean(R_{exc})/H_s$  and  $max(R_{exc})/H_s$  - bottom-right panel).

On the first two hours of ebb there was a strong rundown dominance, followed by two hours and half of alternated flow dominance.

The normalized standard deviation of the runup elevation ( $R_{\sigma}/H_s$ ) represents the runup energy and shows a gradual decrease over the rising tide and an increase over the falling tide (Figure 2.15). The time series of the normalized mean and maximum runup vertical excursions ( $mean(R_{exc})/H_s$  and  $max(R_{exc})/H_s$  respectively) mirrors that of the runup standard deviation (Figure 2.15).

Runup power spectra computed for 15 minute segments of  $R$  were averaged for the rising and falling tide phases (Figure 2.16) and present two distinct peaks of energy at infragravity ( $f < 0.05$

Hz) and incident ( $f > 0.05$  Hz) frequencies during the two tidal phases. The peak around 0.08 Hz (12 s) in the incident band is in agreement with the offshore wave buoy and the inshore PT (Figure 2.12), while a peak at 0.018 Hz (55 s) was found during both tidal phases in the runup spectra, which was not present in the offshore wave spectra (not shown). Runup spectra show that during the falling tide the amount of energy in the infragravity band is significantly higher than during the rising tide, while the incident energy peak is smaller during the falling tide compared to the rising tide (Figure 2.16).

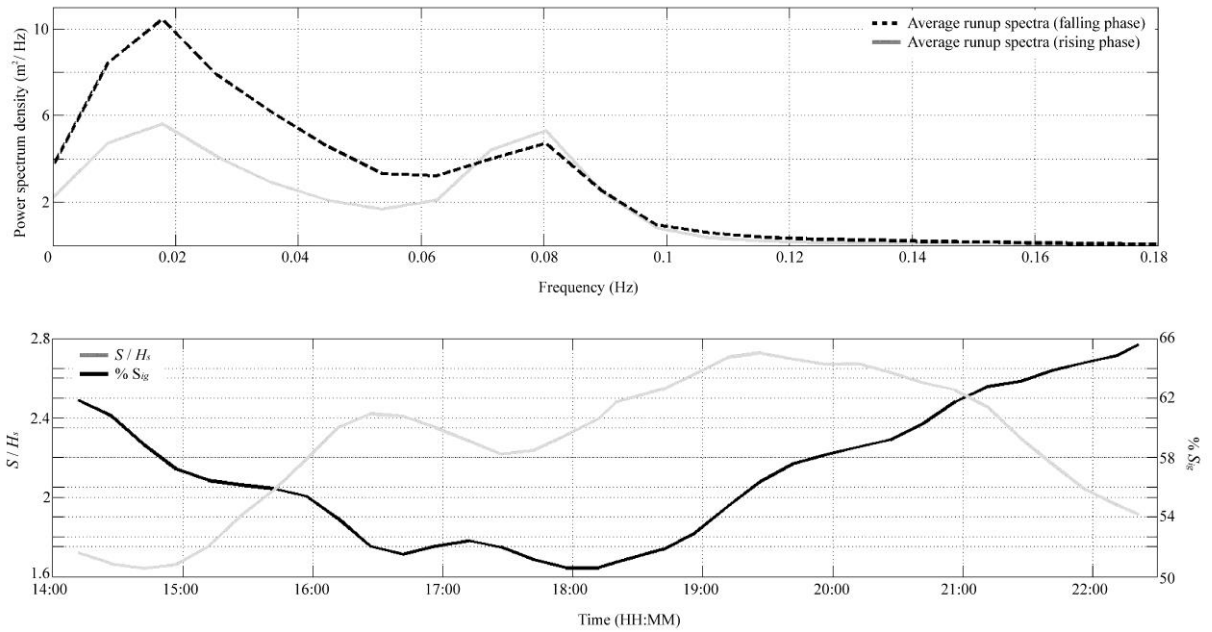


**Figure 2.16** Runup power spectra (top panel) averaged for the rising (gray line) and falling tide (dashed line). The spectra have 16 degree of freedom and the frequency resolution is 0.0089 Hz. Significant normalized runup elevation (black line), normalized by the offshore significant wave height ( $S/H_s$ ) and the percentage of the significant infragravity runup elevation ( $\%S_{ig}$  – gray line) to the total runup energy (bottom panel).

The significant runup elevation ( $S$ ), computed for 15 minutes segments of  $R$  following the method proposed by Stockdon et al. (2006), was normalized by the offshore  $H_s$  ( $S/H_s$ ; Figure 2.16) and shows a similar behaviour to the runup standard deviation and excursions, with lower values during the mid- and high tide stages and higher values at the beginning of the rising and from mid- to low tide of the falling. The significant infragravity runup elevation ( $S_{ig}$ ), computed for  $f < 0.05$  Hz band, is the dominant contributor to the total significant runup elevation ( $> 50\%$ ) during all the tidal



stages (Figure 2.16). The infragravity contribution is most important during mid and low tide stages, and less dominant during low tidal levels, although higher on the falling than during the rising tide.

#### **2.3.2.4 Swash morphological response**

Figure 2.17 shows the morphological change over the recorded tide within the swash zone relative to the initial beach profile ('cumulative change') obtained from the laser scanner. The net morphological change over the tide was modest and characterised by c. 0.10 m accretion over most of the swash zone; however, the maximum cumulative change exceeded 0.6 m.

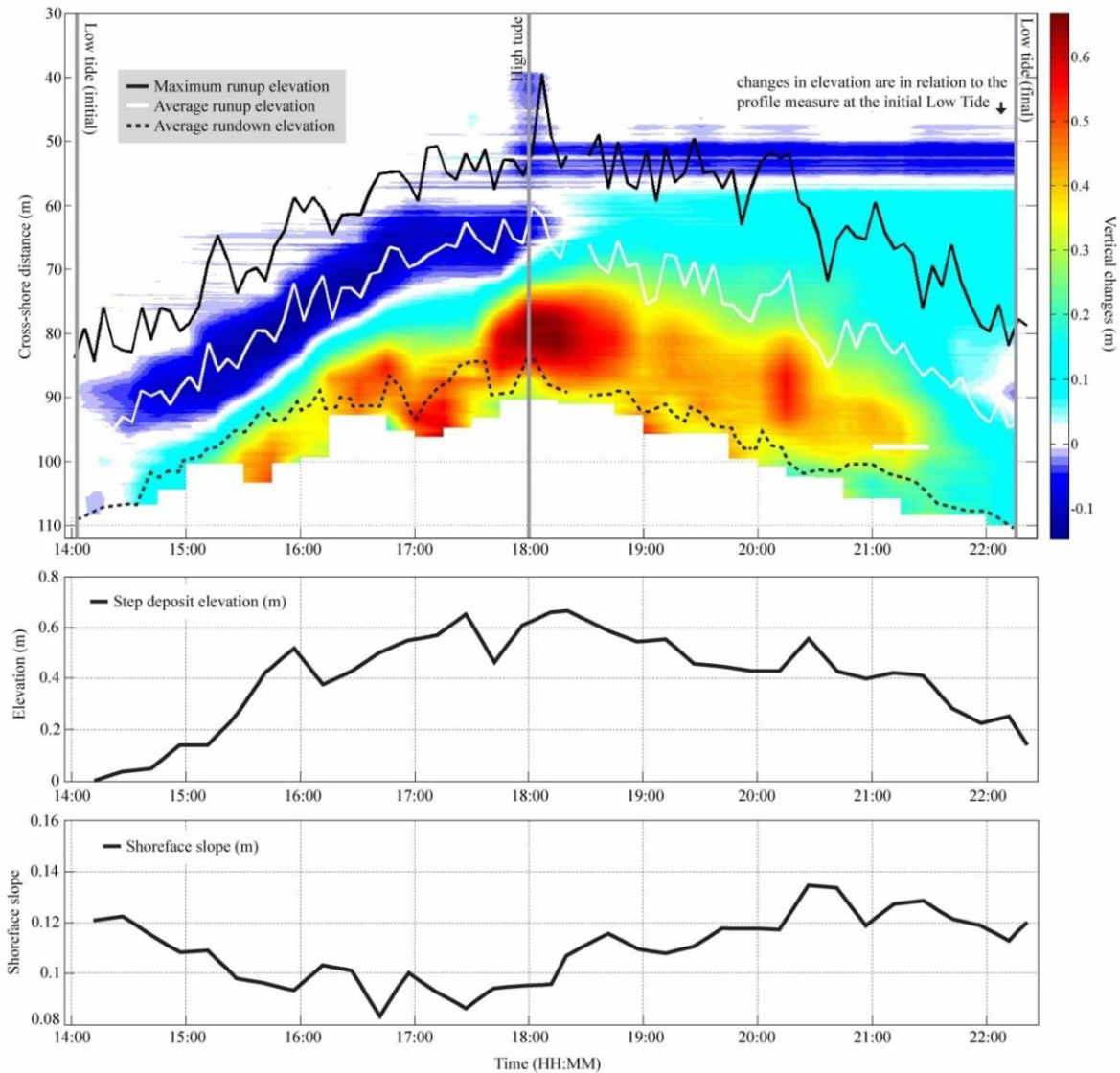


**Figure 2.17** Colour plot showing morphological change relative to the initial beach profile ('cumulative change') obtained from the laser-scanner during the tide cycle (top panel). The white and black line represent the average and maximum runup elevations and the black dashed line represents the average rundown minima computed for consecutive segments of 15 minutes of measurements. Step deposit elevation (mid panel) and shoreface slope (lower panel) during the tide cycle.

The morphological response shows a distinct tidal asymmetry, with the rising tide being characterised by accretion on the lower beach face and erosion dominating the falling tide.

During the initial stage of the rising tide (from 14:00 to 15:00) erosion occurred around the mid-swash zone (cross-shore distance = 90 m) and accretion took place over the lower swash zone (Figure 2.17). This erosion/accretion pattern was sustained over the entire rising tide and by high

tide (18:00) the deposit in the lower swash zone had attained its maximum thickness (c. 0.6 m). Because the sediment accumulation across the lower beach face significantly exceeded the amount of eroded material from the upper swash, it is likely that the source of this gravel was offshore and/or from alongshore transport. Field photos and visual observations indicate that the lower swash deposit was present along the entire beach, but was best developed within beach cusp troughs (Figure 2.18).

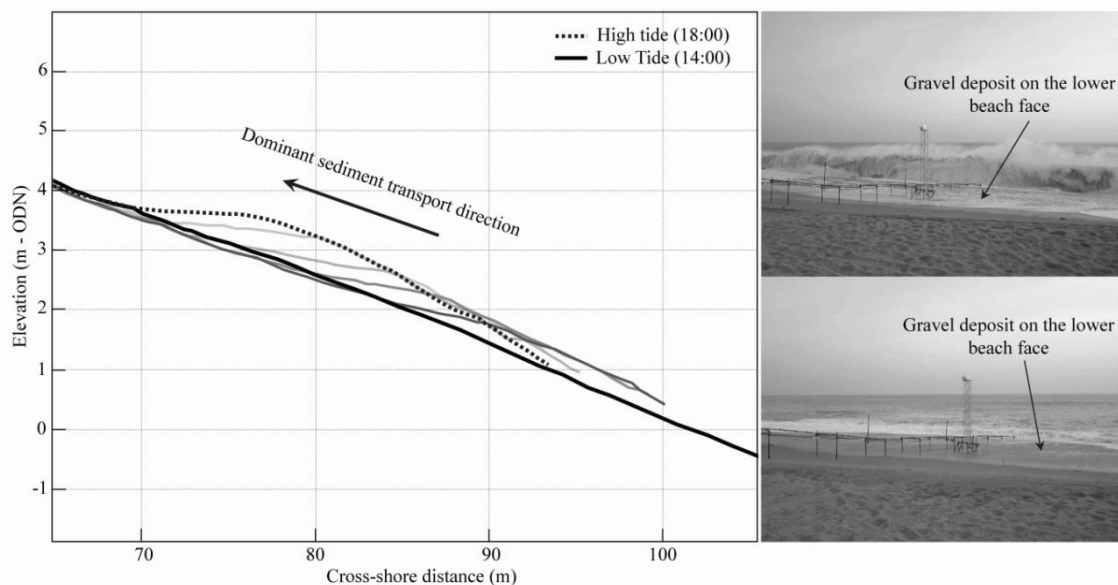


**Figure 2.18** Field photos taken at high tide showing the lower swash gravel deposit (right); several beach profiles showing several stages of growth of the lower beach face deposit during the rising tide phase (left).

The longshore consistency of this deposit during the rising tide phase provides strong evidence of a seaward source of this material (Figure 2.18). Similar to underwater bedforms such as ripples, the shape of deposit is characterised by a gentle up-current slope on the seaward face and a steeper slope on the landward face which suggests that the dominant flows were from seaward to landward, and the gravel was sourced from offshore.

At high tide the lower swash deposit reached its maximum vertical elevation (approximately 80 cm), but during the falling tide the feature progressively reduced in size. It appears that briefly after high tide, some of the material from the lower swash deposit is pushed onshore resulting in c. 0.1 m deposition in the upper swash region, but most of the sediment is taken offshore.

During the rising tide the average runup position correlates closely with the area of erosion in the upper swash zone (Figure 2.17). During this stage of the tide, both the average and maximum runup position follow the same trend with the same spacing between the two runup lines (c. 10 m). The rundown limit also follows the same trend until 16:00 when then it stabilizes and maintains approximately the same elevation until the high tide peak (18:00). At high tide there is a distinct drop in the average runup and rundown position; however, the maximum runup remains at the similar cross-shore position (at  $x = c. 55$  m) until 19:30. During the falling tide both average and maximum runup and rundown position decrease with a relatively constant spacing between the two lines (c. 15 m between average and maximum runup; and 25 m between average runup and rundown limit), but the distance between the lines is significantly larger than during the rising tide (Figure 2.17).

An important consequence of these morphological changes observed on the swash zone is the flattening of the beach face. During the early stages of the rising tide, and until the peak of the high tide, the beach face slope reduces significantly (from 0.12 to 0.08; see Figure 2.17). Initially (from 14:00 to 15:20) this occurs due to the erosion on the upper shoreface and accumulation on the lower part of the profile. Following this initial adjustment, the formation and development of the gravel deposit (from 15:30 until 18:00) significantly increases the elevation of the bed of the lower part of the profile, further decreasing the beachface slope (Figure 2.17). At the peak of the high tide (around 18:00), the gravel deposit reached its maximum elevation (Figure 2.17). After high tide, the shift in swash hydrodynamics from onshore to offshore transport changes the sedimentation pattern

and leads to the loss of sediment mainly towards the offshore. The significant lowering of the bed level across the lower shoreface increases the beachface gradient, which returns to its initial value (0.12; Figure 2.17).

## **2.4 Discussion**

The present chapter describes the deployment of a 2D laser-scanner on a natural gravel beach to perform measurements of the morphology and hydrodynamics in the swash zone during an energetic wave event. The first part of this chapter details the approach used to process the raw laser measurements, including a method to separate the beach topography from the water surface based on a variance threshold, and presents a comparison between the laser measurements and state-of-the-art instruments. The second part of this chapter demonstrates the capabilities of the technique to investigate the swash morphodynamics during energetic conditions when *in-situ* instrumentation is unlikely to survive, let alone yield meaningful data.

### **2.4.1 Deployment and data analysis using a laser scanner**

Only a few field experiments have used laser-scanner technology to perform similar types of measurements as that reported here (Blenkinsopp et al., 2010; Brodie et al., 2012; Almeida et al., 2013), and, as a consequence, very little is known about specific aspects, such as behaviour of the laser measurements for different angles of incidence. The variability in the laser-scanner output was investigated for different angles of incidence during a period where no morphological changes occurred to provide insight into the vertical resolution of the data (Figure 2.8). The results indicate

that for angles lower than  $7^\circ$  the variance in the signal is larger than for high angles of incidence. Taking in consideration that the reflecting angle of the laser beam is the same as the angle of incidence, there is a loss in energy and scanning range with decreasing incidence angle (SICK, 2009).

This characteristic is important for data processing, since the proposed method for separating the raw measurements into bed level and water surface data is based on the identification of a variance threshold that defines the transition between stationary stages (e.g., detection of the bed) to non-stationary stages (e.g., vertical changes induced by the water motions). For the deployment described in this paper, this variance threshold for angles higher and lower than  $7^\circ$  was 1.5 cm and 3 cm, respectively, but this will depend on the type of scanner used and the beach sediments. The present deployment allowed complete coverage of the swash zone, spanning a cross-section of 90 m, and with an average horizontal resolution of 6 cm (Figure 2.6).

## **2.4.2 Comparison of laser measurements and state-of-the-art instruments**

Topographic and runup measurements performed by the laser-scanner were compared with traditional field techniques and show in general a good agreement indicating that the laser-scanner performs these two tasks very well. This result reinforces the good preliminary results obtained in the laboratory and in the field with mild wave conditions by Blenkinsopp et al, (2010, 2012) using similar laser instruments. Some advantages and disadvantages can be mentioned between the laser-scanner and the other remote sensing instruments, regarding the measurements and logistic. Comparing with the bed level sensors, the laser tower requires much less scaffold to be mounted,

the sensor is less exposed to the wave action and the range of the scanner allowed to reach lower regions in the beach where it was impossible to deploy any other instrument.

Regarding the video cameras, one of the main advantages of the laser technology is the fact that it can perform measurements during day and night, which traditional video cameras cannot do. During a storm, the morphological changes occur very fast, as Figure 2.17 demonstrates, and for this reason it is fundamental to have instruments that can track the changes continuously to better understand the underlying processes.

The main disadvantage of the laser-scanner compared to the video is the alongshore limitation of the measurements since it only can survey along a single scan line, while the video cameras can cover a much wider area. Despite these differences, it was clear from the results in Figure 2.11 that the laser-scanner technique has the ability make very good coverage of the swash zone during storm events.

### **2.4.3 Insight into gravel beachface morphodynamics gained using the laser scanner**

The field measurements presented here describe the swash hydrodynamics and morphological response over a tidal cycle (Tide 2) during energetic wave conditions on a gravel beach. The observations indicate that, despite the limited net morphological change over the tidal cycle, significant sediment mobilization occurred during the tide cycle. This result itself demonstrates the importance of being able to make high-frequency measurements on dynamic environments, such as gravel beaches. Such measurements would not be possible using conventional survey methods (e.g., low tide dGPS surveys). The morphological response recorded over an 8-hour period centred

around high tide can be summarised by limited erosion in the upper swash zone and significant accretion in the lower swash zone during the rising tide, and limited accretion in the upper swash zone and significant erosion in the lower swash zone during the falling tide. A comprehensive interpretation of the laser-scanner measurements is presented in Figure 2.19 and provides new insights into the morphodynamics of gravel beaches during energetic wave conditions ( $H_s > 2$  m), whilst complementing previous similar measurements made under mild wave conditions ( $H_s < 1$  m; Kulkarni et al., 2004; Ivamy and Kench, 2006; Austin and Buscombe, 2008; Masselink et al., 2010).

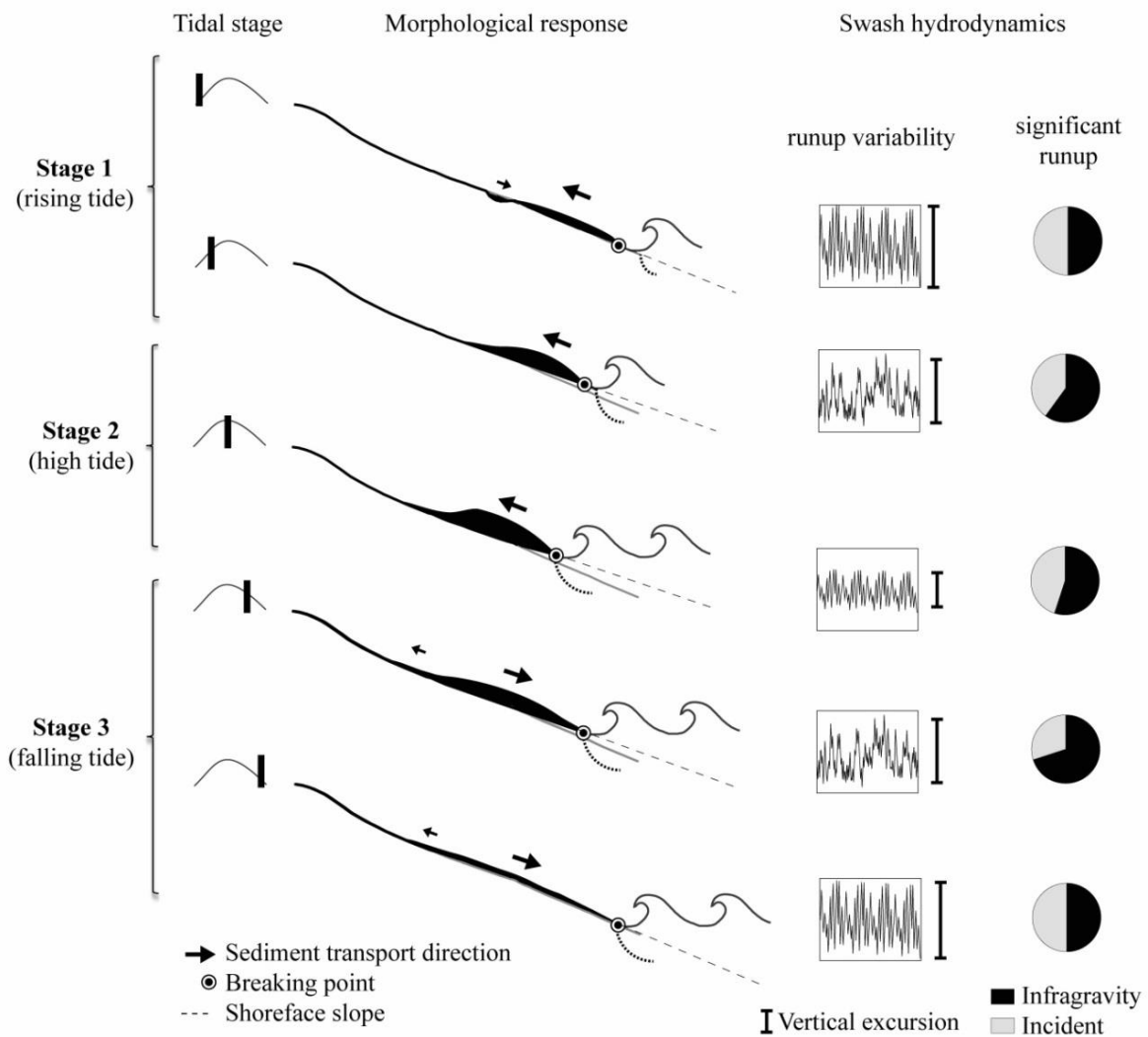


**Figure 2.19** Sketch of the morphological response and runup characteristics of a gravel beach, over a tidal cycle during energetic wave conditions.



**Stage 1** – During the early stage of the rising tide, a sediment deposit forms in the lower swash zone, just above the still water level. The deposit is related to the development and onshore migration of the beach step, a relatively small and steep morphological feature at the base of the foreshore that forms a submerged break of slope at the base of the swash zone which appears to adjust to nearshore hydrodynamics regime (e.g., Hughes and Cowell, 1987). Advection of sediment entrained at the wave breaking point is the most likely mechanism (Voulgaris and Collins, 2000; Brocchini and Baldock, 2008; Alsina et al., 2009) to explain the source of the accumulated material because the amount of eroded material from the upper swash is significantly less than the total amount accumulated on the lower swash. Since the contribution by longshore sediment transport processes is limited (the feature was present along the entire beach), the principal source of this material is considered to be the region just offshore of the step, as observed previously in field experiments with mild wave conditions (Strahler 1966; Austin and Buscombe, 2008; Masselink et al., 2010). It is suggested that the net onshore sediment transport within the swash zone is the combined result of positively-skewed runup flows (predominantly landward) and enhanced sediment suspension in the lower swash due to waves plunging directly onto the beachface while the step deposit is not very pronounced (cf. Masselink et al., 2010).

**Stage 2** – As the tide progresses and approaches high tide, the deposit in the lower swash zone continues to grow and migrate onshore, and the beach gradient in the swash zone decreases. This has a profound impact on the swash hydrodynamics through morphodynamic feedback not previously observed. Specifically, the swash dynamics become less energetic (as quantified by the decreasing trend in all runup parameters) and increasingly dominated by infragravity frequencies. The reason for this change in swash morphodynamics is that as the step feature continues to grow it becomes increasingly a focal point for wave breaking. In other words, the swash region is becoming a dissipative environment with the step feature filtering short period waves as they

transform, break and release their energy at the toe of beach (Ivamy and Kench, 2006). The short wave decay (due to breaking), allows bound long waves to become free to propagate into the swash zone, increasing the energy in the infragravity band (Longuet-Higgins and Stewart, 1962). Although plausible this assumption requires further research in order to eliminate other possible sources for the development of infragravity frequencies in the swash zone (e.g., edge waves). The role of the step as an offshore energy dissipator, akin that of nearshore bars on sandy beaches, has also been alluded to by several authors (Kulkarni et al., 2004; Buscombe and Masselink, 2006; Austin and Buscombe, 2008; Masselink et al., 2010). Interestingly, during this stage of the tide, the skewness of the runup flows switches from positive to negative. By the end of this stage, at high tide, the deposit in the lower swash zone has reached its maximum thickness (0.6 m), the swash zone its minimum gradient (0.09) and the runup parameters (normalised by the offshore  $H_s$ ) their minimum values; this indicates that the protective role of the step deposit is maximized at the high tide.

**Stage 3** – As soon as the tide begins to fall, onshore sediment transport in the swash zone and beachface accretion switches to offshore sediment transport and erosion. This stage is initially characterised by negatively-skewed flows (from 18:00 to 20:00) and in combination with relatively limited sediment suspension during the uprush (because wave dissipate their energy on the step feature) is suggested to be driving sediment offshore, resulting in erosion of the step deposit. A similar control of the step on the swash zone sediment transport processes was also observed in a gravel (Masselink et al., 2010) and a mixed sand/gravel beach (Ivamy and Kench, 2006), during mild wave conditions. Another potentially important process contributing to offshore sediment transport in the swash zone during the falling tide is the change of the watertable slope from landward to seaward, initiating groundwater seepage and promoting offshore sediment transport. This process has been observed in sandy (e.g., Turner, 1990; or Masselink and Turner, 2012) and mixed sand and gravel beaches (e.g., Kulkarni et al., 2004), however recent observations of water

table across this barrier (Loe Bar) indicate a seaward-directed hydraulic gradient is present all the time, thus indicating that independently of the tide stage the slope of the water table will be towards landward (Austin et al., 2013). Erosion during the falling tide gradually removes the step deposit and leads to an increase in the beach gradient in the swash zone. In turn, this results in an increase in the (normalised) runup energy and a decrease in the importance of infragravity frequencies.

The interpretation of the laser-scanner data synthesised in Figure 15 is based on the assumption that the beachface morphology responds instantaneously to the hydrodynamic conditions (swash dynamics). However, it is important to recognise the existence of relaxation times and that it takes a finite amount of time for the morphology to adjust to the changing hydrodynamic conditions imposed by the tide. The tidal translation around mid-tide for the tidal cycle described in this paper represents a horizontal migration rate of 0.1 m per minute (6 m per hour). It is therefore not unlikely that the evolving step deposit (growing or shrinking) is at all time out of equilibrium with the swash and breaker conditions. During the rising tide this means that the deposit is likely to be too low on the beach (lagging behind the rising tide), while during the falling tide it is likely to be too high on the beach (lagging behind the falling tide). It is not appropriate to speculate further on the potential implication of this process using the present data set, but numerical modelling can be used to investigate the importance of relaxation time further. Future laser-scanner deployments on other beaches with different morphology and sedimentology, and varying forcing conditions should also provide further insights.

## 2.5 Conclusion

In this chapter a 2D laser-scanner was deployed on a gravel beach to remotely measure high-frequency swash morphological change and hydrodynamics during an energetic wave event. This innovative method allowed the complete coverage of the swash zone with a vertical accuracy of approximately  $\pm 1.5$  cm and average horizontal resolution of 6 cm, during the entire tide cycle and showed consistent results comparable with traditional field techniques (e.g. video cameras, ultrasonic bed-level sensors or dGPS). Detailed analysis of the laser-scanner measurements provided new insights into the swash morphodynamics of gravel beaches during energetic wave conditions. Results indicate that despite the small net of morphological changes over the tide cycle, significant sediment mobilization occurred during the tide cycle. A clear asymmetrical morphological response was found during the different tidal phases: the rising tide is dominated by onshore sediment transport (accretionary phase), the falling tide by offshore sediment transport (erosional phase). The main factor controlling this asymmetrical morphological response is the step migration that, depending on the tide phase, dictates the wave breaking point and consequently the amount of advected sediment provided to the uprush. The balance between the uprush and downrush decides the dominant direction of the swash sediment transport. During the rising tide the dominant accretion (step deposit development) decreases the shoreface slope and reduces the runup energy, while during the falling tide the dominant erosion (step deposit remobilization) increases the shoreface slope and increases the runup energy.

### **3. Swash zone morphodynamics and extreme runup of coarse-grained beaches during energetic wave conditions**

This chapter presents an investigation of the swash zone hydrodynamics (extreme runup) and morphodynamics on different coarse-grained beaches during storms under positive freeboard conditions. The analysis presented in this chapter was performed using detailed field measurements (2D laser-scanner) and extended using a numerical model (Xbeach-G). This Chapter is an extension of a conference proceedings publication (International Coastal Engineering conference - Almeida et al., 2014) with the addition of two field datasets and numerical modelling.

#### **3.1 Introduction**

Coarse grained beaches are common at high latitudes (e.g., Canada, UK, and Ireland) and at many locations elsewhere, although on a world-wide scale they are relatively scarce. The composition, size and form of these beaches varies widely; however, according to Jennings and Schulmeister (2002) they can be classified into three categories: (1) pure gravel beaches (PG), composed of particle sizes ranging from fine gravel to coarse pebbles, with minimal sand; (2) mixed sand-gravel beaches (MSG), with high proportions of both coarse particles and sand, with thorough mixing of the two size fractions in the beach deposit; and (3) composite sand-gravel beaches (CSG), with an upper foreshore composed of gravel and cobbles, and a lower foreshore of sand, generally with a distinct boundary between them.

The vast majority of research into the swash morphodynamics of coarse-grained beaches has been concerned with PG beaches, particularly of relatively small-scale processes during mild wave conditions (e.g., Horn et al., 2003; Austin and Masselink, 2006; Ivamy and Kench, 2006; Pedrozo-Acuña et al., 2006; Austin and Buscombe, 2008; Masselink et al., 2010) and, more recently, during energetic wave conditions (Poate et al., 2013). Typically PG beaches are different in form to MSG and CSG, and the morphodynamics of MSG and CSG are distinct and potentially more complex than either pure sand (PS) or PG beaches (Kirk, 1970; Jennings and Shulmeister, 2002; Kulkarni et al., 2004; Pontee et al., 2004; Ivamy and Kench, 2006). There is further evidence to suggest that the hydrodynamic regimes and morphological response of MSG and CSG beaches will be different from PG and PS beaches, largely due to the differences in the transport and permeability characteristics of sand and gravel (Pontee, *et al.*, 2004).

Sand is moved predominantly by saltation and suspension, by both currents and waves, while gravel is moved by sliding and rolling (and saltation to a lesser extent) primarily by waves (Carter and Orford, 1984). Thus, gravel has a propensity for onshore movement due to its high threshold of motion and the asymmetry of swash zone action (Carr, 1983). Sand, on the other hand, can move onshore or offshore under wave action.

The higher permeability of PG beaches encourages swash infiltration and this forms the basis for the mechanism of slope development under swash asymmetry. On PS beaches the swash infiltration mechanism responsible for onshore swash transport is considered to be insignificant due to the low levels of infiltration (Masselink and Li, 2001). On MSG and CSG beaches, the water table response is controlled by the underlying sand content, which can lead to a similar behaviour to a PS beach and the development of lower slopes (Orford and Carter, 1984). While steep berms can form on PG beaches, the higher hydraulic conductivity permits greater energy dissipation than occurs on a

similarly steep MSG beach, where even 20% sand content reduces the hydraulic conductivity by an order of magnitude (Mason *et al.*, 1997).

The hydraulically rough and permeable nature of the coarse sediments ( $D > 2$  mm), together with their ability to develop a steep beach-face (reflective), provide coarse-grained beaches with efficient mechanisms for wave energy dissipation and therefore a natural means of coastal defence (Carter and Orford, 1993; van Wellen *et al.*, 2000; Buscombe and Masselink, 2006; Moses and Williams, 2008). These aspects have raised a recent interest in these environments for engineering applications such as beach nourishment (e.g., Moses and Williams, 2008); however, there are important limitations in understanding the behaviour of these beaches under energetic wave conditions (i.e., storms).

The lack of field measurements provides the main reason for this knowledge gap and stems from the lack of suitable instruments capable of making direct measurement in an energetic swash zone in which large clasts are moving and where significant morphological changes occur in a very short period of time (Osborne, 2005).

Remote sensing methods emerge in this context as the most appropriate solution for this type of field measurement, and recent developments on the use of 2D laser-scanners (Blenkinsopp *et al.*, 2010, 2012; Brodie *et al.*, 2012; or Almeida *et al.*, 2015) to perform high frequency measurements of swash zone dynamics (including morpho- and hydrodynamics) have proved to be one of the most suitable tools for this propose.

In line with these aforementioned justifications, the aim of present chapter is to improve the understanding of swash zone morphodynamics of coarse-grained beaches during energetic wave conditions using field measurements performed with a 2D laser-scanner. To accomplish this, four field experiments were performed on different coarse-grained beaches under energetic wave conditions ( $H_s > 2$  m). The unique datasets were analysed to characterize and compare the

morphological responses of the gravel beaches and hydrodynamic characteristics under these conditions.

## **3.2 Methods**

### **3.2.1 Study sites and field deployments**

Six field experiments were conducted between March 2012 and November 2013 at six different coarse-grained beaches: 1) Westward Ho! in North Devon – CSG; 2) Chesil in Dorset – coarse PG; 3) Hayling Island in Hampshire – CSG beach; 4) Slapton in South Devon – PG; 5) Loe Bar in Cornwall – fine PG; and 6) Seascale in Cumbria – MSG beach. Figure 3.1 shows the location of each site and a sketch of the type of beach profile, while information about the tidal regime, wave climate, sediment size and survey dates is presented in Table 3.1.



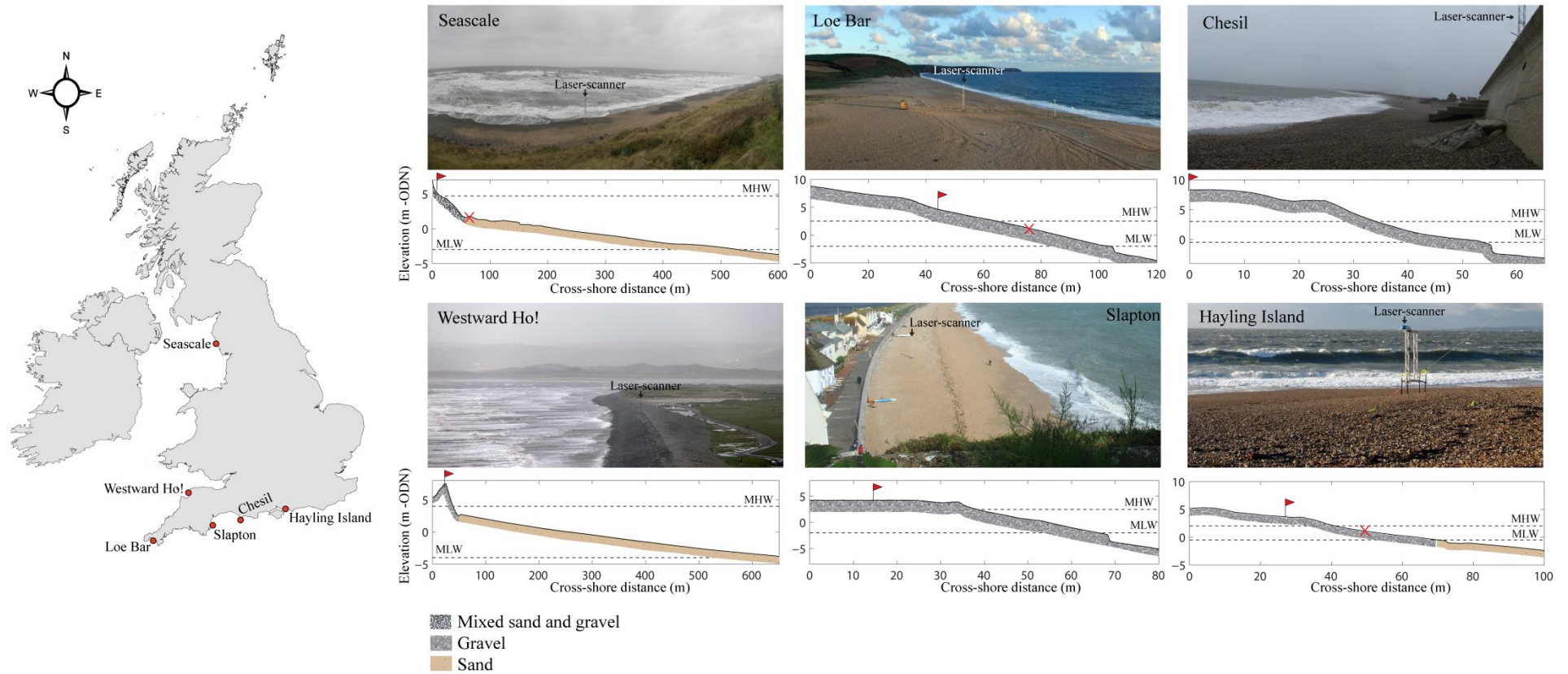


**Figure 3.1** Study site locations, field photo and sketch of the type of beach profile showing shape, composition, location of the laser-scanner (red flag) and inshore pressure transducer (red cross), and highest and lowest water level (HWL and LWL) observed during the field experiments.

	Westward Ho!	Chesil	Hayling Island	Slapton	Loe Bar	Seascale
Survey dates	2nd and 3rd November 2013	16th and 17th December 2012	27th and 28th October 2013	20th to 22nd October 2013	23rd to 25th March 2012	28th and 29th January 2013
Spring Tidal range (m)	7	3.5	4.6	4.4	4.5	7
Mean annual $H_s$ (m)	1.1	1	0.7	0.65	1.2	1
Mean annual $T_p$ (s)	9.8	8	7.6	7.8	9.1	3.5
Mean annual $\theta_{wave}$ (quad)	W	SW	S	S	SW	SW
$D_{50}$ (mm)	170	50	16 (gravel) and 0.15	6	2 to 4	2 to 60 (gravel) and 0.24 (sand)

**Table 3.1** Wave climate, tides and sediment characteristics of the study sites.

### **Westward Ho! – cobble CSG beach**

Westward Ho! is a cobble ridge that extends northwards across the mouth of the Taw-Torridge estuary (approximately 3 km long). The north section of the ridge is composed of sand dunes (near the estuary) while the southern section is formed by a cobble ridge. The coarse upper section of the beach contrasts with the wide (about 500 m wide) sandy intertidal terrace. The deployment at this site was performed on the central section of the cobble barrier (Figure 3.1). The mean spring tidal range measured at Bideford is 7 m, the average significant wave height 1.1 m and peak period of 9.8 seconds from the west (Table 3.1).

### **Chesil beach – coarse PG beach**

Chesil beach is a long (18 km), linear, coarse PG beach that extends from Abbotsbury in the west to Chesilton in the east, where it is backed by a seawall (Figure 3.1). With a systematic long-shore size-grading, the mean size of the pebbles increases from the west ( $D_{50} = 25$  mm at Herbury Point)

towards the east, Chesilton ( $D_{50} = 50$  mm), while beach width decreases from west (150 to 200 m wide) to a width of 40–60 m at its eastern end (Carr, 1969). The present deployment was performed at the eastern end of Chesil beach, in front of the seawall, where the beach profile is characterised by a narrow berm attached to the toe of the structure and a very steep beach face with a pronounced beach step at the bottom of the profile (Figure 3.1). The mean spring tidal range at Bridport is 3.5 m and waves from the south-west have an average annual significant height around 1 m with 8 seconds of peak period (Table 3.1).

#### **Loe Bar – fine PG beach**

Loe Bar is part of a 4.3-km long gravel beach ( $D_{50} = 2\text{--}4$  mm) that extends from Porthleven, in the north, to Gunwalloe, in the south (Figure 3.1). Loe Bar barrier fronts Loe Pool and extends 430 m between the adjacent headlands, with an average width of 200 m and a typical seaward gradient of 0.1. With a NW-SE shoreline orientation, the barrier faces south-west and is exposed to energetic Atlantic swell with an annual average significant wave height ( $H_s$ ) of 1.2 m, an average peak period ( $T_p$ ) of 9.1 s and a direction ( $\theta_{wave}$ ) of SW (Table 3.1 - Poate *et al.*, 2013). The tidal regime is macro-tidal with a mean spring tidal range of 4.5 m.

#### **Hayling Island – CSG beach**

Hayling Island is a CSG beach located in the East Solent and forms part of the much larger Solent estuarine system. The beach runs from the entrance to Langstone Harbour in the west, to Chichester Harbour in the east, over a distance of approximately 6 km. West of Chichester Harbour, for about 2 km, the beach is relatively narrow and many groynes have been constructed over the years to deal with erosion and flooding problems (Whitecombe, 1996). To the west of this area, the beach is much wider and unprotected, and this is where the field experiment was undertaken. At this location

the beach profile presents a steep upper foreshore composed of coarse gravel ( $D_{50} = 16$  mm) and a gently sloping sandy lower foreshore exposed at low water. The mean spring tidal range is 4.6 m and, due to the shelter provided by the Isle of Wight, the mean annual significant wave height of this area is only 0.7 m with peak periods of 7.6 s (Table 3.1).

#### **Seascale – MSG beach**

Seascale is a MSG beach located on the Cumbria coastline and part of a 9-km coastal segment running from Ravenglass, in the south, to Sellafield, in the north (Figure 3.1). This coastal section is formed by a high frontal dune ridge (approximately 10 m high), except in the front of the village of Seascale, where the dune ridge is absent and instead is occupied by human infrastructure (houses, car park and a seawall). The foreshore is composed of a narrow (between 50 to 70 m) and low-gradient mixed sand and gravel beach face (gravel size varies between  $D_{50} = 2$  to 60 mm; and sand with  $D_{50} = 0.24$  mm), fronted by a very large sandy intertidal terrace (approximately 500 m wide) with irregularly spaced patches of boulders. The mean spring tidal range is 7 m and the mean annual significant wave height of this area is approximately 1 m with peak periods of 7 s (Table 3.1).

#### **Slapton – medium PG beach**

Slapton Sands beach is a 4.5-km-long pure gravel barrier ( $D_{50} = 2$ -10 mm) located in Start Bay (SE Devon). With an average crest elevation of 7 m (ODN Datum), the barrier is backed by a shallow freshwater lagoon (Slapton Ley) on the southern section. The barrier shoreline orientation is north-south and the barrier width increases from south to north. Despite a small sediment gradient from the south to the north of the barrier (the northern end of the beach is consistently finer than the southern), the sediments along this barrier are well-sorted. The field deployment was performed at the southern section of the beach where a seawall can be found in the upper part of the beach and

the beach width is relatively narrow. Slapton Sands is exposed to a low-to-medium energy wave climate (mean  $H_s = 0.65$  m and  $T_p = 7.8$  s), comprising a mixture of southerly swell and easterly wind waves (Ruiz de Alegria-Arzaburu and Masselink, 2010). The tidal regime is macrotidal with spring and neap ranges of 4.3 m and 1.8 m, respectively (Admiralty Tide Tables, 2009).

### 3.2.3 2D Laser-scanner

Field experiments were performed during energetic wave conditions ( $H_s > 2$  m) and measurements included the characterization of the offshore and inshore wave conditions (obtained from offshore wave buoys and inshore pressure transducers deployed at some of the sites) and high-frequency swash morphological changes and hydrodynamics measured with a 2D laser-scanner. The working principles of this instrument and details regarding the data processing are described in Chapter 3. After initial data processing, the laser measurements are separated in two distinct time series (Figure 3.2): (1) continuous beach topography and (2) swash hydrodynamics (including water elevation and runup edge). These time series form the basis of the analysis in the present work.

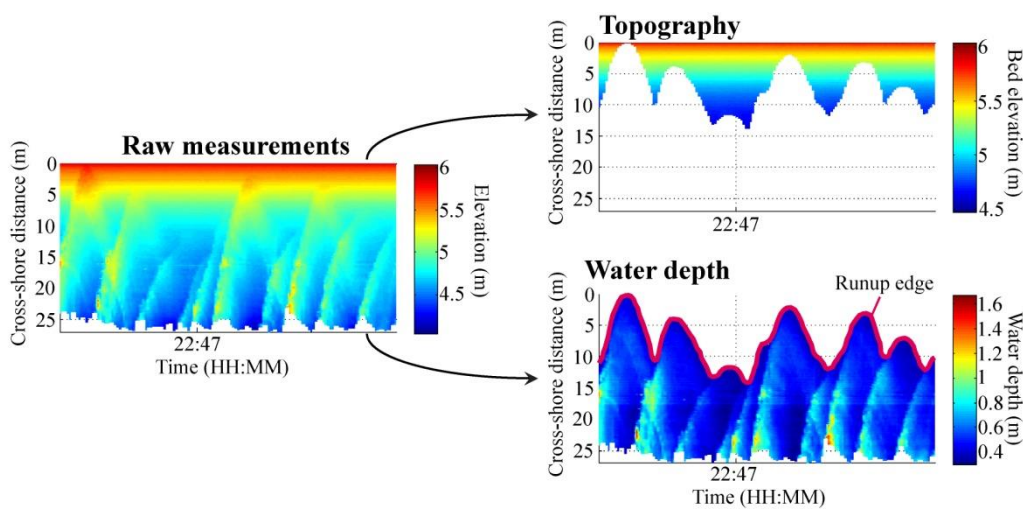


**Figure 3.2** Raw measurements obtained from the laser-scanner (left panel) and the two types of time-series obtained after the data processing: 1) continuous topographic measurements (top-right panel) and 2) swash hydrodynamics (bottom-right panel).

### 3.2.3 Xbeach-G model

To complement the field-based analysis of the swash hydrodynamics, a process-based model capable of simulating the hydrodynamics and hydrology on gravel beaches during storms, Xbeach-G, (McCall et al., 2014), was used. Xbeach-G is an extension of the existing open-source, process-based, storm morphodynamic model called Xbeach (Roelvink et al., 2009), which simulates the hydrodynamics of gravel beaches and barriers. In contrast to Xbeach, Xbeach-G uses a one-layer, depth-averaged, non-hydrostatic scheme, similar to the SWASH model (Smit et al., 2013), which allows it to solve wave-by-wave flow and surface elevation variations due to short waves in the nearshore zone. This aspect is particularly important for coarse-grained beaches, where a swash motion is mainly at incident frequencies, and infragravity is expected to be less important (Buscombe and Masselink, 2006).

Depth-averaged flow due to waves and currents is computed in Xbeach-G using the non-linear shallow water equations, including the exchange with the groundwater from:

$$\frac{\partial \zeta}{\partial t} + \frac{\partial h u_z}{\partial x} + s = 0 \quad (3.1)$$

where  $x$  and  $t$  are the horizontal spatial and temporal coordinates, respectively,  $\zeta$  is the free surface elevation above an arbitrary horizontal plane,  $u_z$  is the depth-averaged cross-shore velocity,  $h$  is the total water depth ( $h = \zeta - \xi$ , where  $\xi$  is the elevation of the bed above an horizontal plane) and  $s$  is the surface water-groundwater exchange flux.

The non-hydrostatic pressure term is also included on the non-linear shallow water equations using the following solution:

$$\frac{\partial u}{\partial t} + u \frac{\partial u}{\partial x} - v_h \frac{\partial^2 u}{\partial x^2} = -\frac{1}{\rho} \frac{\partial(\bar{q} + \rho g \zeta)}{\partial x} - c_f \frac{u|u|}{h} \quad (3.2)$$

where  $v_h$  is the horizontal viscosity,  $\rho$  is the density of water,  $\bar{q}$  is the depth-averaged dynamic pressure normalized by the density,  $g$  is the gravitational constant and  $c_f$  is the bed friction factor (computed using Chézy formula for turbulent flow, where roughness height is computed as  $3D_{90}$ ).

The model accounts for upper swash infiltration losses and exfiltration effects on the lower swash using a newly developed groundwater model coupled to Xbeach (McCall et al., 2012). Due to relatively large hydraulic conductivity of coarse sediments, infiltration/exfiltration can become significantly important process (e.g., Masselink and Li, 2001). Horizontal groundwater flow in the aquifer is computed following the law of Darcy (1856) and assuming incompressible flow, using the following solutions:

$$\frac{\partial h_{gw} u_{gw}}{\partial x} + w_{gw,s} = 0 \quad (3.3)$$

$$u_{gw} = -K \frac{\partial \bar{H}}{\partial x} \quad (3.4)$$

where  $u_{gw}$  is the depth-averaged horizontal groundwater velocity,  $h_{gw}$  is the height of the groundwater surface above the bottom of the aquifer,  $w_{gw,s}$  is the vertical groundwater velocity at the groundwater surface, which includes the surface water-groundwater exchange flux ( $s$ ),  $K$  is the hydraulic conductivity of the aquifer and  $\bar{H}$  is the depth-averaged hydraulic head.

### 3.3 Results

#### 3.3.1 Wave and tide records

Wave (offshore) and tide measurements obtained during the field experiments at each site are presented in Figure 3.3. The largest offshore wave conditions were observed at Westward Ho! with maximum significant wave heights ( $H_s$ ) reaching 4 m, with average peak period ( $T_p$ ) of 13 s. Two tidal cycles were measured by the Laser-scanner at this, the most energetic site. At Chesil Beach, measurements were performed during a single tide cycle, covering an energetic SW (wave direction normal to the shoreline orientation) swell event with the offshore wave buoy recording waves with  $H_s$  of approximately 2.5 m and  $T_p$  around 10 seconds (Figure 3.3). A similar SW swell event, with slightly longer wave periods ( $T_p$  were between 10 and 13 s) and less steep waves, was recorded at Loe Bar during three tide cycles. Despite the similarities between these two SW events, the measured wave spectra (Figure 3.3 bottom) show that the swell event measured at Loe Bar was characterized by well-defined unimodal spectra, while at Chesil there was some mixture of long-period swell with short waves. At Hayling Island an extreme wind event (with gusts above 150 km/h – measured at the Isle of Wight) with a southerly direction was responsible for the generation of 3.5 m ( $H_s$ ) waves with wave periods between 10 and 20 seconds, during which two tide cycle of measurements were performed. At Slapton a combined S-SE short period energetic wave event, with  $H_s$  of approximately 2 m and  $T_p$  between 6 and 12 s was measured during 4 complete tide



cycles. Finally, at the Seascare one tide cycle was measured during a wave event with average offshore  $H_s$  of 3 m and  $T_p$  of 8 seconds (Figure 3.3).

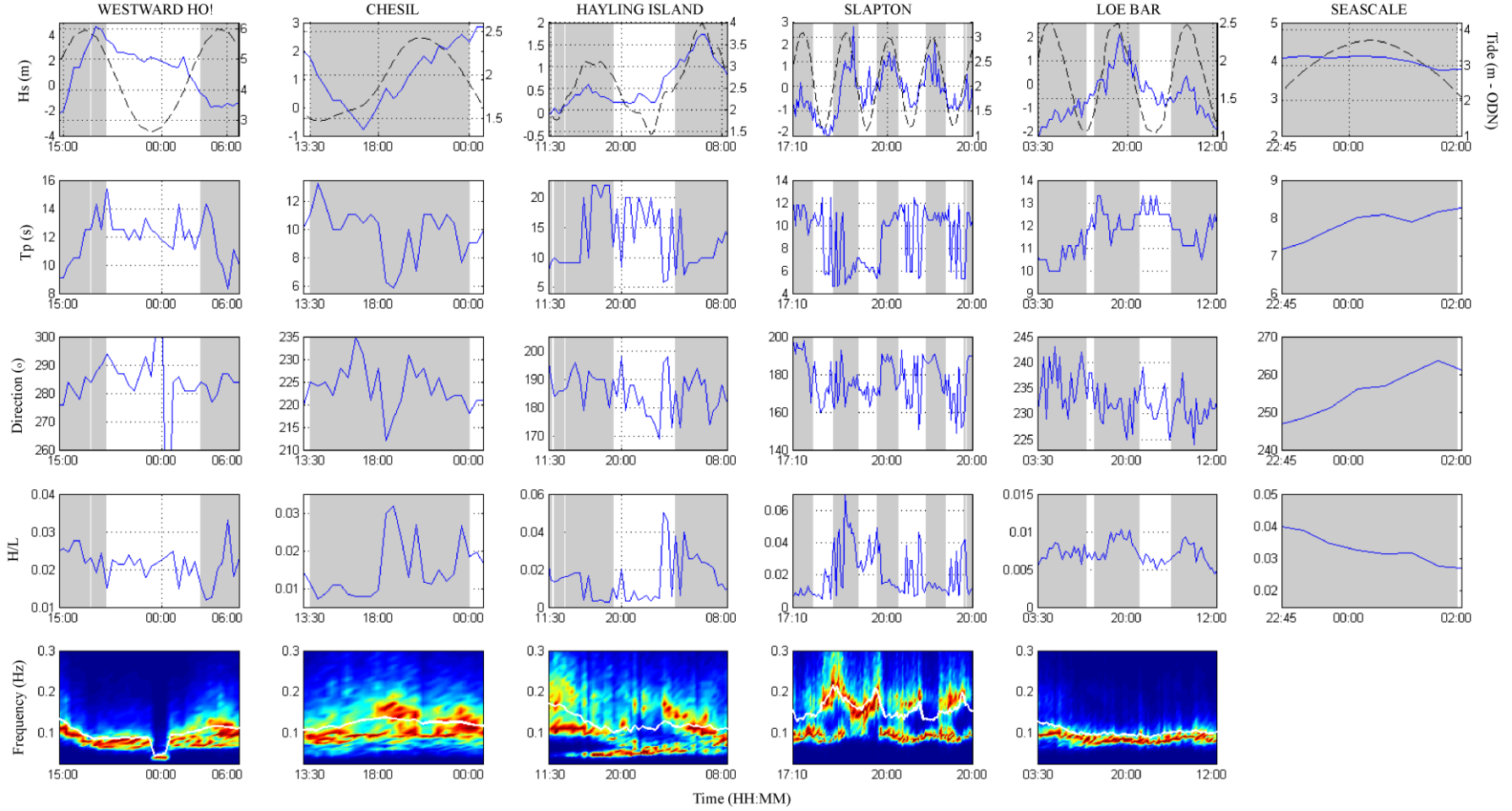


**Figure 3.3** Tide height relative to ODN datum (black dashed line), offshore significant wave height (blue line – top panels), peak period, wave direction, wave steepness and normalized wave spectra with the overlap of the mean period ( $T_{m-10}$ ) measured by the offshore wave buoys during the laser measurements (grey areas).

### 3.3.2 Field data analysis and Xbeach-G modelling

#### Wave conditions on the swash

Wave observations performed by the inshore PTs were compared with offshore wave measurements to assess the amount of wave dissipation on the surf zone and the boundary conditions of the swash zone at these different sites. The wave breaking conditions at each site were assessed by field photographs and the calculation of the surf similarity parameter ( $\xi$ ), computed as:

$$\xi = \frac{\tan \alpha}{\sqrt{H/L_0}} \quad (3.5)$$

where  $L_0$  is the offshore wave length ( $= g / 2\pi T^2$ ).

#### Swash hydrodynamics

Swash hydrodynamics, measured by the laser-scanner at the different sites, were analysed through the calculation of the following statistical parameters from the runup time-series ( $R$ ): (1) 2% exceedance of the runup maxima ( $R_{2\%}$ ); and (2) swash flow velocity skewness ( $\langle u^3 \rangle$ ), computed as:

$$\langle u^3 \rangle = \frac{\langle u^3 \rangle}{\langle u^2 \rangle^{1.5}} \quad (3.6)$$

where  $u$  is the cross-shore instantaneous velocity of the runup edge, computed through the first derivative of the horizontal runup ( $R_x$ ) time series (Figure 3.4).

The concept of swash velocity skewness is explored here as a proxy for the swash flow dominance, and a potential indicator of the sediment transport direction. For instance, a positively skewed

result indicates uprush flow dominance due to the dominance of short period and faster uprush flows in relation to longer and slower backwashes (Figure 3.4 – left). Negatively skewed results, on the other hand, indicate backwash flow dominance, with swash flows showing opposite characteristics to what was explained for positively skewed flows (Figure 3.4 – right).

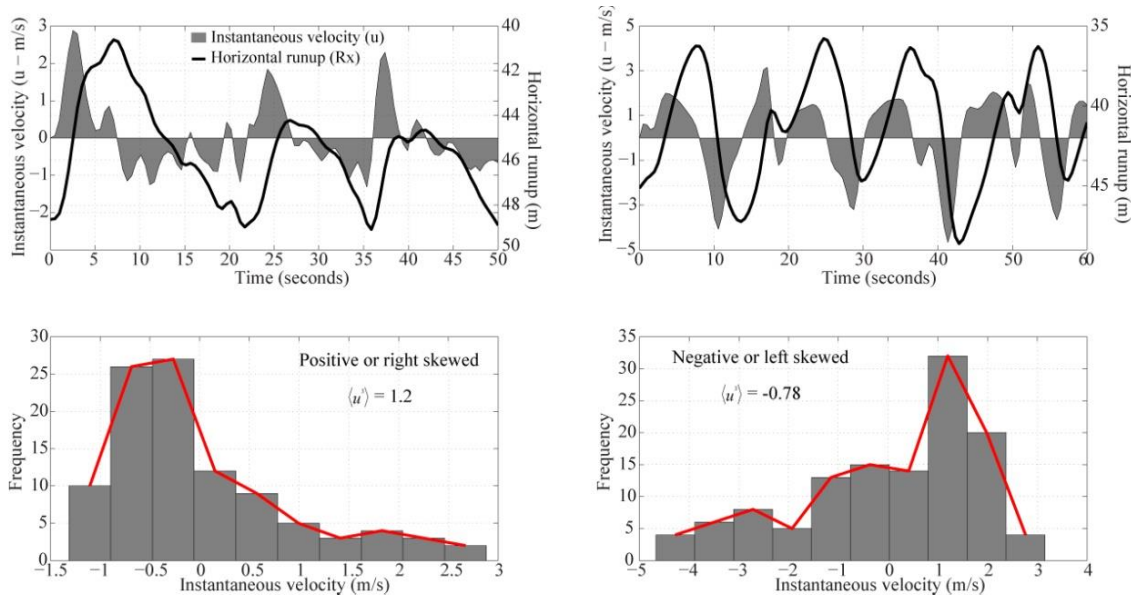


**Figure 3.4** Two examples of swash velocity skewness results: left) time series of horizontal runup and respective instantaneous velocity (top), and resultant positively skewed velocity distribution (bottom); right) time series of horizontal runup and respective instantaneous velocity (top), and resultant negatively skewed velocity distribution (bottom).

## Swash morphological response

Swash morphological response was analysed by computing the cumulative vertical difference between consecutive beach profiles measured with the laser-scanner and the beach gradient (slope of the region constrained by the upper runup and lower rundown limit). All hydrodynamic and morphological parameters were calculated for continuous segments of 15 minutes of data.

## Swash morphodynamics and extreme runup

The morphodynamic status of the beach was determined using the surf-scaling parameter (Guza and Inman, 1975),  $\varepsilon$ :

$$\varepsilon = \frac{\pi^2 H_s}{g T_p \tan^2 \beta} \quad (3.7)$$

where  $\tan \beta$  is the beach gradient and  $g$  is gravity. This morphodynamic index was used to explore the relationship between the different beach morphodynamics states of the beach and the extreme runup during energetic wave conditions. In order to test different beach slope types and wave periods on equation (3.7), four different calculations were performed: 1) using peak period  $T_p$ ; 2) using the mean period  $T_{m-10}$  computed as:

$$T_{m-10} = \frac{m_{-1}}{m_0} \quad (3.8)$$

where  $m$  represents the different spectral moments; 3) using the slope of the swash zone ( $\beta_{swash}$ ) 4) and the "effective" slope (Saville, 1958) of the entire active section of the profile, extending between the wave breaking point and the maximum runup limit ( $\beta_{effective}$  – Figure 3.5).

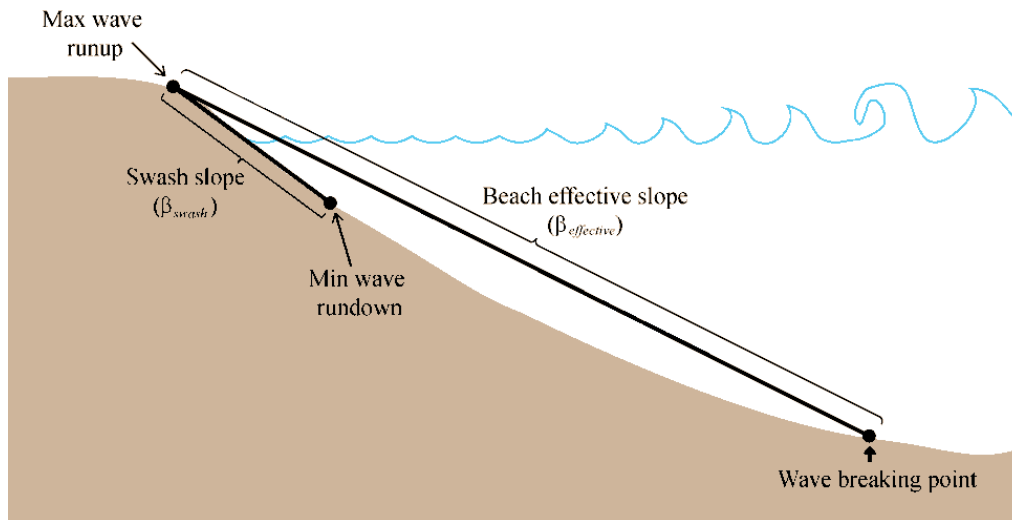


**Figure 3.5** Sketch of the swash and effective slope calculations.

### **Xbeach-G modelling**

In addition to the field data analysis, the numerical model Xbeach-G was used to explore the importance of high-frequency morphological changes and groundwater interaction on extreme runup during energetic wave conditions. For each site a cross-shore profile model was set up (1D) using the measured topography and bathymetry (at the same location as the laser-scanner profile) to create a numerical grid. The cross-shore resolution of the models was set to vary gradually in the cross-shore direction in order to correctly capture wave breaking and wave runup in the model (e.g. coarse resolution offshore and finer inshore).

All the models were forced using wave spectra measured at the nearest wave buoy along with measured or predicted tide measurements during periods around the high tide. The hydraulic conductivity and sediment size used for each model were derived from measurements or literature (McCall et al, 2014). In order to assess the importance of the fast morphological changes and groundwater effects on the extreme runup, four different setups of the model were tested: Setup 1) Fixed morphology (using a single initial profile during the entire simulation) and groundwater on;

Setup 2) Updating morphology (updating every 10 minutes the grid in the model, in a similar way to McCall, et al. (2014)) and groundwater on; Setup 3) Fixed morphology and groundwater off and Setup 4) Updating morphology and groundwater off. To avoid influence of simulated sediment transport and morphological changes, sediment transport and morphological modules of the model were turned off during all simulations.

### **3.3.3 Wave conditions on the swash**

A comparison between offshore and inshore wave measurements was performed to assess the amount of wave dissipation that occurred between the offshore wave buoy and the inshore PT (Figure 3.6). In order to remove the tidal modulation effect present in part of the PT measurements, only high tide measurements were used.

From this comparison it is possible to verify that at Loe Bar (fine PG beach) the wave height at the lower beachface was higher or proportional to the offshore measurements, while at Seascale and Hayling Island a significant reduction of the wave height was observed on the inshore PT measurements (Figure 3.6). This result is a consequence of the different mechanisms of wave dissipation induced by the different types of beach profile shape that these sites present. While at PG beaches the absence of the development of an offshore bar promotes the dissipation of most of the incoming waves on the beach step, on CSG and MSG beaches the wide and dissipative intertidal terrace reduces significantly the energy of the incident waves.

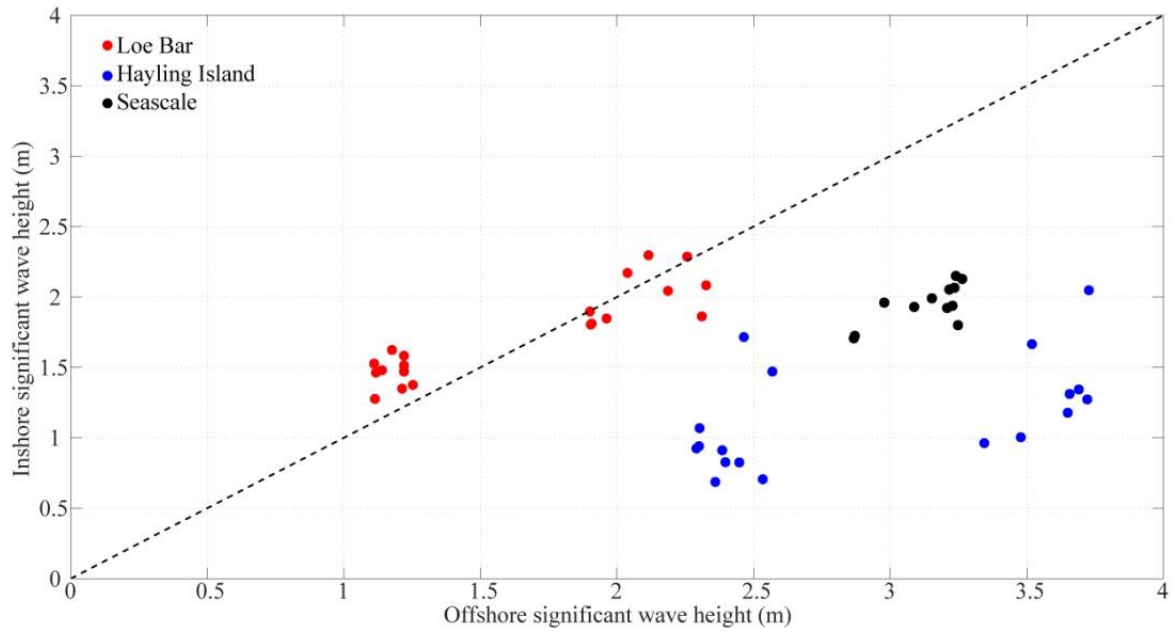


**Figure 3.6** Scatter diagram of the offshore significant wave height measurements versus the inshore significant wave height measurements for all the sites.

As a consequence of such differential surf zone wave dissipation, the breaker type and energy available for sediment transport will differ at all these sites. Figure 3.7 presents field photographs of the breaking conditions in the swash zone of all the study sites during the field experiments, together with the surf similarity values for the measured tides.



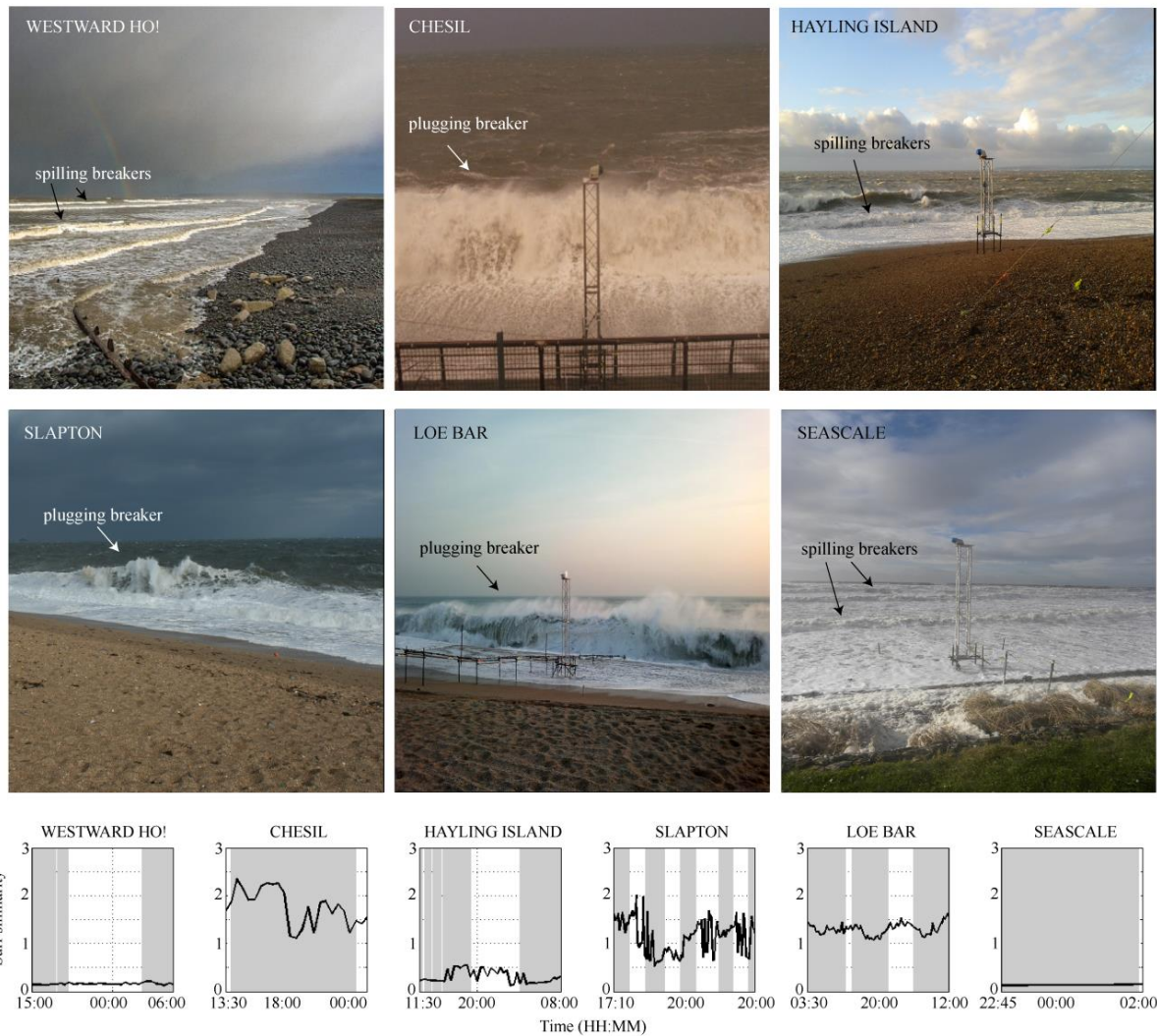


**Figure 3.7** Field photos showing the breaking conditions at each of the study sites during the field experiment; and surf similarity (black line) computed for the time when laser-scanner measurements were performed (grey areas).

Field photographs allow show that PG beaches (Chesil, Slapton and Loe Bar) develop a narrow surf zone on the seaward limit of the swash zone and the dominant wave breaking type is plunging. At Westward Ho! and Seascale, the flat intertidal sandy terraces promote the development of several breaker lines across the entire surf zone (Figure 3.7). Spilling breakers dominate the surf zone and waves approach the swash in the form of a broken bore.

In between these two types of surf zone types is Hayling Island, which presents a narrow intertidal sandy terrace and slightly different mechanisms of wave dissipation from the other sites. During

low tide, spilling breakers dissipate most of the energy on the sandy terrace, creating a dissipative surf zone, while at high tide some fraction of the incident waves reaches the steep (lower) beachface and creating under the form of a mix spilling/collapsing breaker (Figure 3.7).

### 3.3.4 Swash hydrodynamics

For all the sites the most energetic tide cycle (and representative) was selected to illustrate the swash hydrodynamics and time series of the vertical runup ( $R_z$ ),  $R_{2\%}$ , runup spectra and  $\langle u^3 \rangle$  are presented in Figure 3.8.

Extreme vertical runup, calculated here through the  $R_{2\%}$  and normalized by the offshore significant wave height ( $H_s$ ), shows that the highest runup levels were observed at Loe Bar, and Chesil, followed by Hayling Island and Slapton and finally Seascale and Westward Ho! with the lowest values (Figure 3.8, second row). The runup spectra (normalized by the total energy) were computed for each time series of vertical runup (Figure 3.8, third row) and show that different frequencies dominate the swash zone of these sites. At Westward Ho! and Seascale, the sites with the most dissipative surf zones, the peak of energy is in the infragravity band ( $f < 0.05$  Hz) while at Chesil, Slapton and Hayling Island the energy is mostly on the incident band of the swash ( $f > 0.05$  Hz – Figure 3.8). Interestingly, at Loe Bar (fine PG beach) it is possible to identify a peak of energy in the incident band, but most of the energy is in the infragravity band. This indicates that, despite the absence of a developed surf zone, there are mechanisms for the development of low frequencies (Figure 3.8).

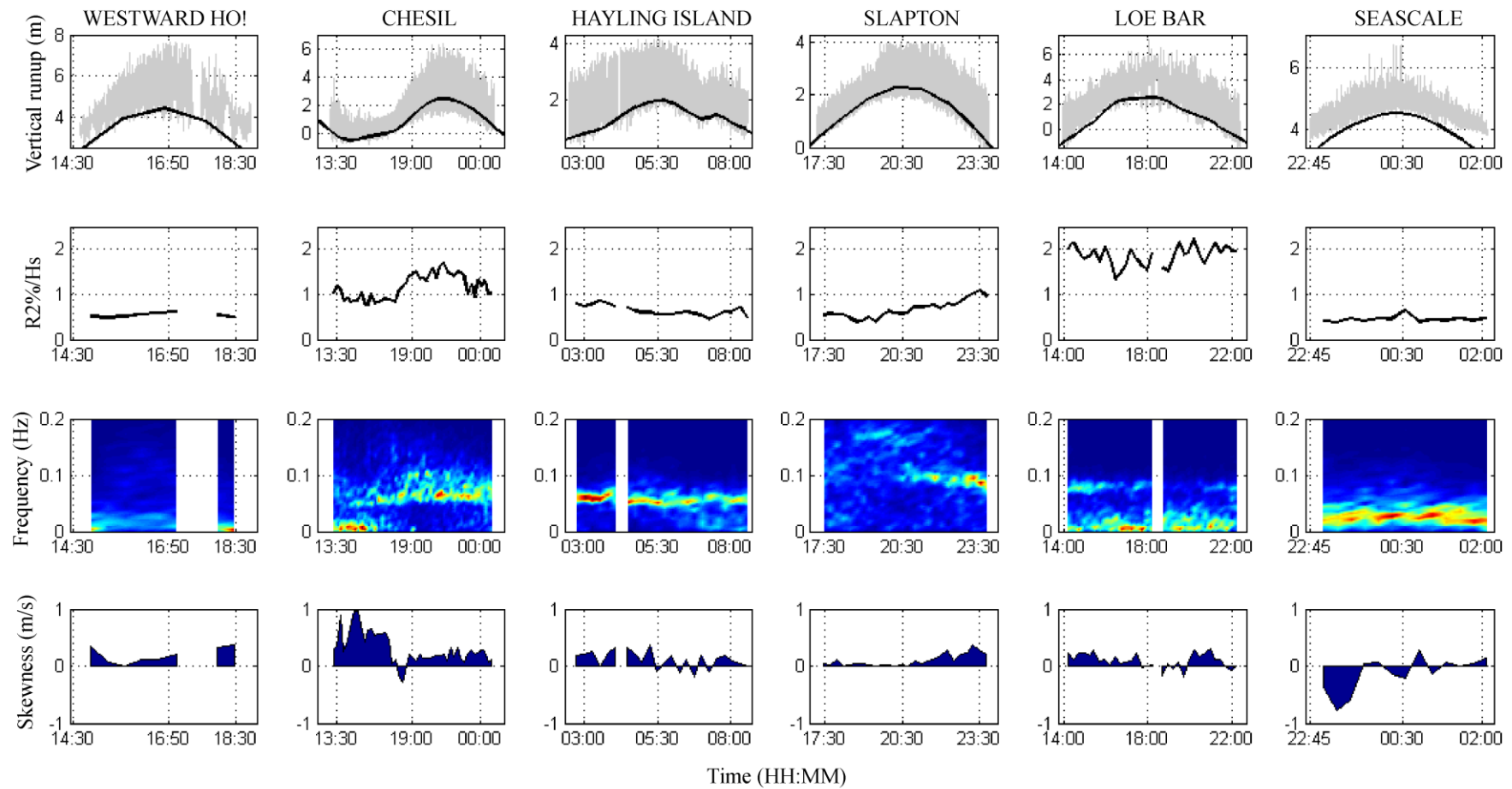


**Figure 3.8** Time series of vertical runup (grey) with the overlap of the tide elevation (black line – top panels); 2% exceedence of the runup maxima (second line of panels); vertical runup spectra, normalized by total energy (third line of panels); and swash flow skewness (bottom line of panels), computed for all the sites.

Swash flow asymmetry was assessed through velocity skewness  $\langle u^3 \rangle$  and results show that coarser foreshores (Westward Ho!, Chesil, Hayling Island and Slapton) show the highest asymmetries, with a clear dominance of onshore flow asymmetry (positive  $\langle u^3 \rangle$  values - Figure 3.8, last row). On the fine PG (Loe Bar) and MSG (Seascale) beaches, the values for  $\langle u^3 \rangle$  showed significant variability, indicating alternating onshore and offshore flow asymmetry (Figure 3.8).

### 3.3.5 Swash morphological response

To evaluate the morphological response of the different coarse-grained beaches, the cumulative topographic changes and the beach face gradient were determined (Figure 3.9). Interpretation of these results reveals that PG beaches are characterised by an asymmetrical morphological response during tidal cycles, while for the CSG and MSG beaches the changes are persistent through the entire tidal cycle (Figure 3.9, first row and bottom panels).

At both Chesil and Loe Bar the rising tide is characterized by dominant onshore sediment transport, with the development and onshore translation of a step deposit (Figure 3.9), an accretionary morphological feature linked to beach development (Poate et al., 2013). During the falling tide the step deposit gradually moves offshore, shifting the dominant sediment transport direction towards offshore (Figure 3.9). This process is also observed at Slapton, however with less magnitude. At Westward Ho! and Hayling Island the present observations showed persistent erosion on the upper beach face and berm, with the accumulation of the eroded sediment on the lower beach (Figure 3.9).

At Seascale the morphological changes observed were relatively small compared with the other sites and showed persistent erosion on the lower beach face accompanied by accumulation on the upper part of the profile (Figure 3.9).

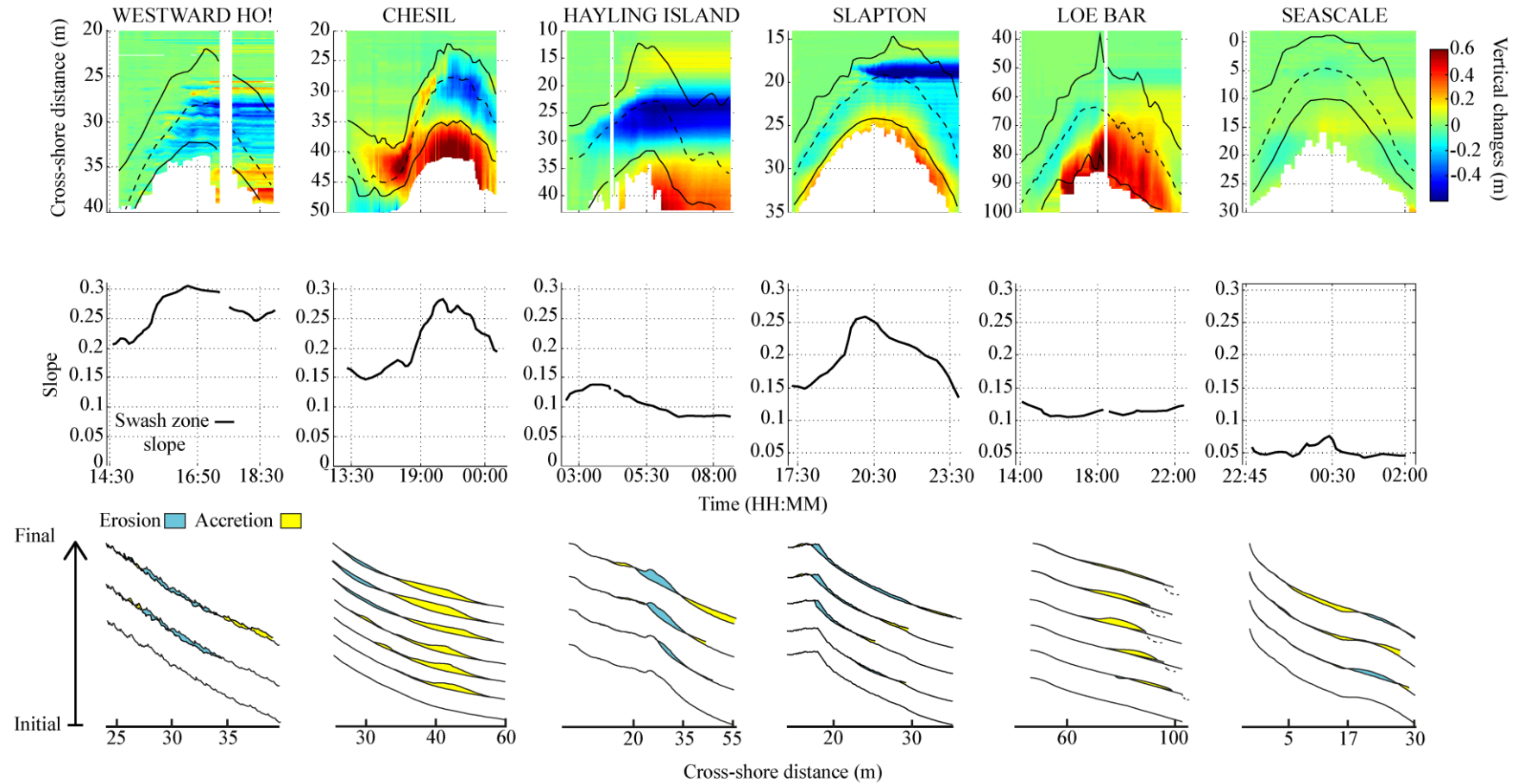


**Figure 3.2** Contour plots showing the cumulative topographic changes calculated from the laser-scanner observations (top panels) with the overlap of the maximum and mean runup and minimum backwash position (black lines); swash gradient (second row of panels); and a sketch of the representative morphological changes observed during a tide cycle (lower panels).

### 3.3.6 Beach morphodynamic states and runup

To compare and contrast the extreme runup characteristics of the different beaches and place them within a morphodynamics framework, the normalised extreme runup was plotted against the surf scaling parameter (Figure 3.10).

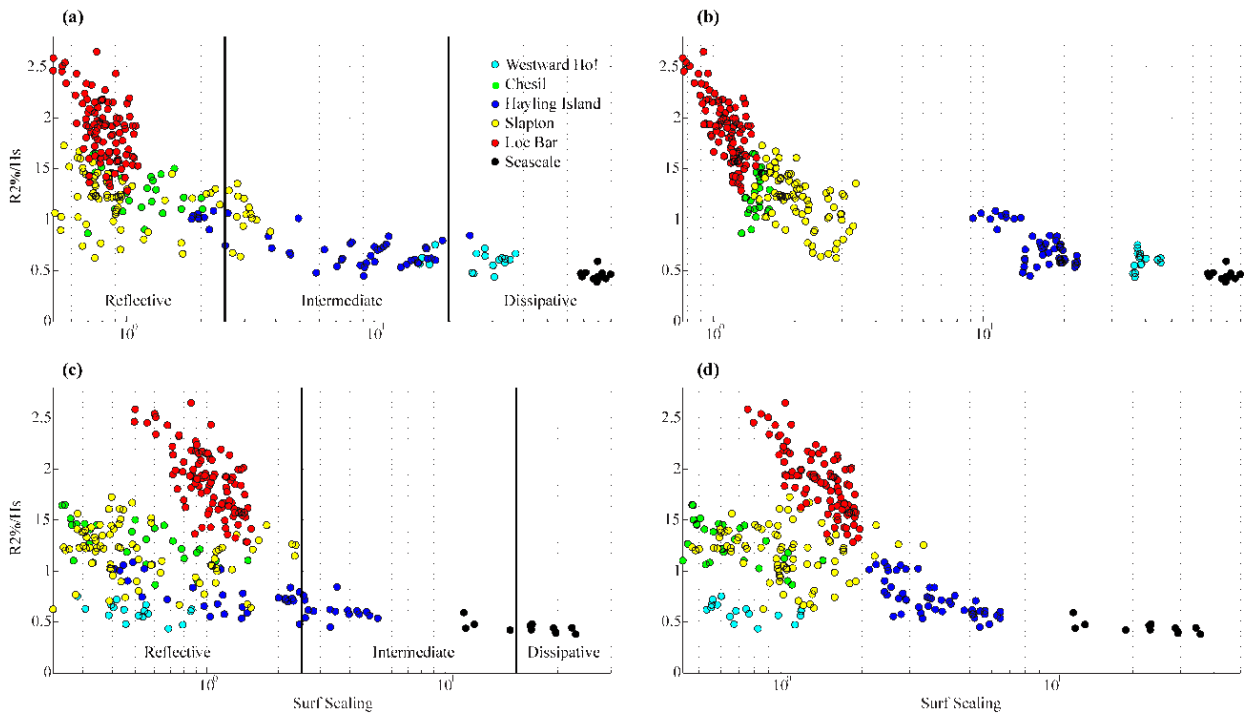


**Figure 3.3** Scatter diagram of the surf scaling parameter versus the extreme runup ( $R_{2\%}/H_s$ ) for all the sites. Surf scaling was computed using (a)  $T_p$  and  $\beta_{effective}$ , (b)  $T_{m-10}$  and  $\beta_{effective}$ , (c)  $T_p$  and  $\beta_{swash}$  and (d)  $T_{m-10}$  and  $\beta_{swash}$ .

The relationship between the beach morphodynamic state and extreme runup shows that lower runup elevations are linked to dissipative and intermediate beaches (e.g., Seascale, Westward Ho! and Hayling Island), while the highest runup values are associated with the reflective PG beaches (Loe Bar, Chesil and Slapton). From the four tests the best overall relationship with the extreme runup is found when the  $T_{m-10}$  and  $\beta_{effective}$  were used (Figure 3.10b). In the other tests (Figure 3.10a, c and d) a significant amount of scatter can be found under reflective states, with different PG

beaches showing different runup levels for the same values of  $\epsilon$ , using  $T_{m-10}$  and  $\beta_{effective}$  the scatter reduces significantly.

### 3.3.7 Xbeach-G modelling

Simulations were performed for all the six coarse-grained beaches and included four different model setups, as explained above. Time series of modelled vertical runup ( $R_{zmodel}$ ) were obtained for each site and used to calculate the 2% of the runup maxima ( $R_{2\%}$ ). To compare the modelled with the measured extreme runup, two statistical measures were computed:

$$RMSE(x) = \sqrt{\frac{1}{N} \sum_{i=1}^N (x_{i,modelled} - x_{i,measured})^2} \quad (3.9)$$

$$bias(x) = \frac{1}{N} \sum_{i=1}^N (x_{i,modelled} - x_{i,measured}) \quad (3.10)$$

Table 3.2 presents the results of the statistical measures computed for each model test for all the sites. The best model results (lowest *rmse*) were obtained using Setups 1 and 2, the ones where the groundwater module was on (Table 3.2), providing a clear demonstration that groundwater is an important parameter when predicting runup on coarse-grained beaches. As expected, the effect of the groundwater module is more evident on the coarser sites (Westward Ho!, Chesil or Hayling Island), where high hydraulic conductivity is expected to have an important effect on the runup excursions (Table 3.2).

The effect of updating the profile bed during the simulations (Setup 2 and 4), which should theoretically provide a more realistic morphology to the model, seems to make no clear improvement on the model results. The only exceptions were Hayling Island and Loe Bar, where the bed update improved the model results (Table 3.2), with a significant impact on the reduction of the overestimation of the runup (see *bias* difference between Setup 1 and 2 on Table 3.2).

Site	Model setup		Statistical measures	
	Morphological updating	Groundwater	<i>rmse</i> (%)	<i>bias</i> (%)
Westward Ho!	No	On	19.6	0.26
	Yes	On	19.5	0.29
	No	Off	30.6	0.61
	Yes	Off	29.7	0.58
Chesil	No	On	10.4	0.32
	Yes	On	13.9	0.44
	No	Off	22.5	0.85
	Yes	Off	23.9	0.88
Hayling Island	No	On	41.0	0.64
	Yes	On	23.2	0.34
	No	Off	50.2	0.90
	Yes	Off	34.8	0.58
Slapton	No	On	21.5	0.32
	Yes	On	24.8	0.39
	No	Off	27.1	0.41
	Yes	Off	24	0.37
Loe Bar	No	On	15	-0.23
	Yes	On	13.5	0.02
	No	Off	15.7	-0.06
	Yes	Off	18.6	0.21
Seascale	No	On	9.1	0.03
	Yes	On	12.2	-0.12
	No	Off	14.2	0.13
	Yes	Off	8.7	-0.01

**Table 3.2** Results of the statistical measures (*rmse* and *bias*) for the comparison between the measured (laser-scanner) and modelled  $R_{2\%}$ .

Despite the low values ( $< 0.3$  m), the results show a persistent overestimation of the runup predictions (positive *bias*), although with error values always under 23% (Table 3.2) indicating the



skill of Xbeach in predicting extreme runup on this type of environment and support for the present analysis.

## **3.4 Discussion**

### **3.4.1 Wave breaking and swash boundary conditions**

In the initial section of this work the dissipation of the offshore waves in the surf zone was assessed by comparing the offshore and inshore wave measurements, and a clear difference on surf zone dynamics was noticed between the different coarse-grained beaches. Field observations showed that the PG beaches (Chesil, Slapton and Loe Bar) develop very narrow surf zones with waves dissipating most of their energy on the beach step, a relatively small morphological feature at the base of the foreshore that forms a submerged break-of-slope at the base of the swash zone and which appears to adjust to the nearshore hydrodynamics regime (e.g., Hughes and Cowell, 1987). The beach step on PG beaches acts in an analogous way to a nearshore bar on sandy beaches by dissipating incident wave energy (Buscombe and Masselink, 2006); however, due to the very small distance between the beach step and swash zone, a large amount of wave energy still propagates into the swash zone. For this reason the inshore wave measurements were similar to or higher than the offshore wave measurements. Different surf zone mechanisms occur when the beach profile presents a wide and very dissipative intertidal terrace, such as at Seascale or Westward Ho! Here, most of the offshore wave energy is dissipated across a wide surf zone before reaching the swash zone; therefore, a significant reduction in the wave height was observed when comparing the inshore PT data with the offshore wave measurements.

Hayling Island (the CSG beach) occupies an intermediate position. Characterised by a small beach step and a narrow intertidal terrace, it develops a slightly wider surf zone than the PG beaches, but

narrower and less dissipative than the dissipative beaches (i.e., Westward Ho! and Seascale). The reduction in the wave height from offshore to inshore here was also significant, and with a similar ratio to that observed for Seascale. Nevertheless, it is important to take into consideration that the position of the inshore PTs at these two sites was different. At Seascale, the inshore PT was located on the lower beach face, and during mid- to high tide was measuring the surf zone processes, while the inshore PT deployed at Hayling Island was located on the middle beach face and during mid- to high tide was measuring mostly swash zone processes (e.g. swash bores).

### **3.4.2 Swash hydrodynamics and morphological response**

The different surf zone dynamics promote different boundary conditions for the swash zone and this has a direct effect on the sediment transport processes. The character of wave breaking is significant in the context of sediment transport, because the amount of turbulence reaching the bed depends on wave (breaker) type. For instance, the momentum impact of plunging breaker vortices on the seabed mobilizes larger amounts of sediment than spilling breakers (Aagaard and Hughes, 2010). This aspect is particularly important on these different coarse-grained beaches where major differences in the dominant breaker type were identified. At PG beaches the dominant plunging breakers are believed to represent a key mechanism to entrain sediment from the step into the water column (e.g. Brocchini and Baldock, 2008), from where it is subsequently advected into the uprush flow and transported onshore before settling down at flow reversal.

During the rising tide, the onshore translation of the breaking point, together with the unsaturated beach face, promotes onshore sediment transport and an important reduction of backwash flows due to the large amount of infiltration during the uprush. These processes are believed to contribute to the development of the beach step deposit during the rising tide (Kulkarni et al., 2004; Almeida et

al., 2015), while on the falling tide the offshore shift of the breaking point decreases the advected sediment into the uprush and creates a deficit in onshore sediment transport and favours offshore sediment transport through the backwash. The dynamic equilibrium between beach morphology and hydrodynamics provides PG beaches with an efficient mechanism of natural protection, but seems absent on the other types of coarse-grained beaches.

At Seascale and Westward Ho!, the presence of a very dissipative surf zone seems to be a fundamental aspect of their differentiation from the other sites since most of the offshore wave energy is dissipated before reaching the swash zone. When waves reach the swash zone they dissipate their energy with spilling breakers, or arrive in the form of a broken bore, and these tend to generate less turbulence on the bed (Christensen and Deigaard, 2001) and therefore less sediment is added to the water column and transported onshore. This is reflected in the small magnitude of morphological changes observed at Seascale and Westward Ho!, despite the energetic offshore wave conditions.

On Hayling Island beach, despite the presence of a small beach step, the mechanism of step translation found on the PG beaches did not occur. The persistent erosion of the upper beach face and berm crest during energetic wave conditions on CSG beaches has been observed elsewhere (e.g., Pontee et al., 2004), but continuous measurement of the morphology and swash hydrodynamics of this beach type during energetic conditions is absent in the literature. Present observations showed that the narrow intertidal sandy terrace on Hayling Island beach dissipates an important amount of the offshore wave energy, which induces waves to break before reaching the swash zone. Therefore the levels of energy in the swash zone and the potential onshore sediment transport decreases, favouring offshore sediment transport through the backwash. This process neglects any longshore contributions to sediment transport, which may be important aspect,

especially when offshore waves approach swash with oblique angles (e.g., Ruiz de Alegria-Arzaburu and Masselink, 2010).

Although these field observations provide new insights on the morphological response of coarse grained beaches during energetic wave conditions, they provide limited information regarding the importance of antecedent morphological conditions in affecting the future morphological response. A clear example of the importance of this aspect was recently demonstrated in the BARDEX experiment (Matias et al., 2012), where it was found that the morphological condition prior to extreme storm conditions can have an important impact on a gravel barrier response during the extreme storm (e.g., delaying the occurrence of overwash events).

### **3.4.3 Extreme runup on coarse-grained beaches**

The behaviour of runup under dissipative conditions is different than during reflective or intermediate conditions (Senechal et al., 2011). Present observations showed that dissipative states (Westward Ho! and Seascale) are associated with lower vertical runup levels and runup dominated by infragravity frequencies ( $f < 0.05$  Hz). These results resemble those from low-sloping sandy beaches, where typically during storms most of the swash energy is concentrated in the infragravity band (Ruggiero et al., 2004), due to the saturation of the incident band and release of the group-bound long wave in shallow water (Longuet-Higgins and Stewart, 1962).

On the other side of the morphodynamic spectrum are the reflective environments, mostly observed on the PG beaches (Loe Bar, Chesil and Slapton), where the highest vertical runup excursions were observed and where the swash was dominated by the incident band ( $f > 0.05$  Hz). Here very strong wave dissipation occur over a narrow area and on a short time scale (narrow surf zones dominated

by plunging breakers), with almost no time to build up significant non-linear processes (Ruessink et al., 2013) and therefore lacking the mechanisms for the development of infragravity waves. Interestingly, on the fine PG beach, Loe Bar, most of the runup energy was found in the infragravity band, indicating that swash hydrodynamics on this PG beach might be different from the others. As explained in Chapter 3, such energy development in the infragravity band can be result of a morphological feedback. With the onshore migration of the beach step during the rising tide and the consequent step deposit development, the step increasingly becomes a focal point for wave breaking and the swash region becomes a dissipative environment (due to the reduction of beach slope), leading to the development of infragravity energy (Almeida et al, 2015). Another possibility, independent from any morphological response, may be related to offshore forcing conditions. The offshore wave buoy at Loe Bar measured a very long period swell during the experiment. These waves are less steep and the wavelength and period of the incoming long wave may match the dispersion relationship, such that resonant forcing of a free long wave can occur (Contardo and Symonds, 2013).

Finally during intermediate states, found only at Hayling Island, the vertical runup level is also intermediate (in between the levels observed on the reflective and dissipative environments), although in contrast to the dissipative beaches the peak runup here was found on the lowest frequencies of the incident band. The presence of a narrow low-tide terrace could suggest that, similar to what was observed at Loe Bar, non-linear interactions due to wave breaking could generate a source for the development of infragravity waves. However, such interactions were not observed, perhaps due to the different forcing conditions observed at this site. While at Loe Bar a long period swell was observed, at Hayling Island the waves measured by the offshore wave buoy were associated with a very energetic local wind event. With short wind waves, bound long waves

are not released and therefore there can be no development of low frequency waves (Contardo and Symonds, 2013).

### **3.4.3 The effect of groundwater and morphological evolution on the runup**

Xbeach-G model was used in the present Chapter to extend the runup analysis, and in particular to investigate the importance of groundwater and morphological evolution in modelling extreme runup. Results from the present simulations show that, by turning on the groundwater in the model (Setup 1 and 2), the error on the extreme runup predictions reduces by about 5% for the fine gravel beaches and by 10% for the coarser beaches (Westward Ho!, Chesil and Hayling Island) when compared with the model results with the groundwater module off (Setup 3 and 4). These results are expected, since permeability increases with coarser grains, increasing infiltration (Masselink and Li, 2001) and friction forces (Horn and Li, 2006), thereby reducing velocity and runup elevation. Therefore the most pronounced effect of the groundwater in the model results is a significant reduction in the overestimation of the runup (positive *bias*) when this module was on (Table 3.2).

The effect of rapid morphological changes on the extreme runup predictions was also investigated with Xbeach-G by updating the bed of the model every 10 minutes during the simulations (Setups 2 and 4). The results show that, with the exception of Hayling Island and Loe Bar, the update of the bed during the simulations did not significantly improve or modify the results. One reason for this lack of improvement in the model predictions is the fact that at most of the sites the observed morphological changes were not significant and had limited impact on the runup processes. The only exception is the case of Chesil, where the development of the step deposit caused significant modification of the lower section of the beach profile (Figure 3.10). Here it would be expected that,

in a similar way to Loe Bar, step development could affect the runup predictions. However, there is an important difference in the swash hydrodynamics between these two PG beaches. While at Loe Bar the rundown limit was located seawards from the step deposit (Figure 3.10), at Chesil the average rundown limit was located landward from the deposit. This difference indicates that while at Loe Bar the step deposit is inside the swash zone and is likely to affect the runup, at Chesil the deposit is outside the swash zone and has limited influence on the runup excursions. Figure 3.11 shows the comparison between the measured and modelled (using results from Setup 2) runup and rundown limits, and demonstrates that the swash zone simulated by Xbeach-G is also within the same limits as the field observations. This reinforces the idea that updated morphology had little effect on the runup calculations in these simulations.

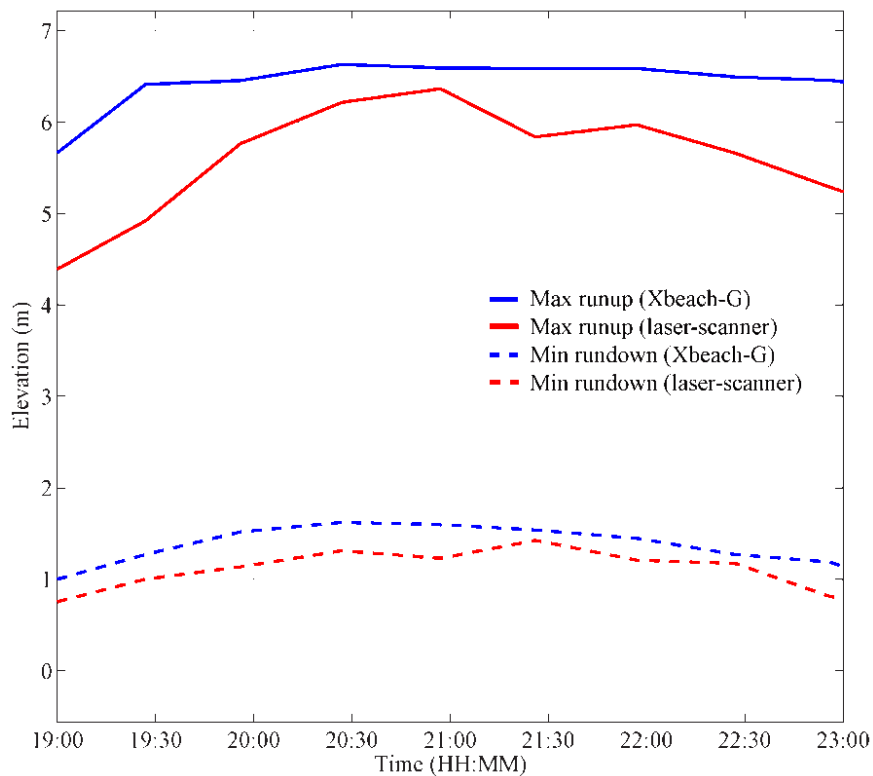


**Figure 3.11** Comparison between the measured (red) and modelled (blue) runup and rundown limits at Chesil Beach.

At Loe Bar and Hayling Island, important morphological changes occurred inside the active area of the swash zone; therefore the bed update resulted in improved runup predictions. This aspect reveals the importance of including rapid morphological changes when modelling extreme runup on coarse-grained beaches.

### 3.5 Conclusion

A 2D laser-scanner was deployed on four different coarse-grained beaches (three PG beaches, two CSG and one MSG beach) to measure swash zone hydrodynamics and morphological changes during energetic wave conditions. Contrasting mechanisms of wave dissipation in the surf zone seem to represent the key aspect of differentiation between all the coarse-grained beaches in regard to swash hydro- and morphodynamics. On reflective PG beaches, a narrow surf zone dissipates most of the offshore wave energy on the seaward boundary of the swash, promoting an energetic swash zone and large vertical runup excursions, while on intermediate and dissipative MSG and CSG beaches, a substantial amount of wave dissipation occurs before the waves approach the swash, therefore creating a less energetic swash zone with shorter vertical runup excursions. The morphological feedbacks occurring under such different swash hydrodynamics are also significantly different. PG beaches present an asymmetric morphological response during the tidal cycle (accretion during the rising and erosion during the falling tide) as a result of beach step adjustments to the prevailing hydrodynamics; whereas MSG and CSG beaches lack similar mechanisms and therefore morphological changes on these beaches tend to occur over the entire tidal cycle. Surf scaling parameters, parameterized with the beach effective slope ( $\beta_{effective}$ ) and mean period ( $T_{m-10}$ ), show a good relationship with the measured extreme runup ( $R_{2\%}$ ), although groundwater



interactions and swash morphological changes, not quantified by the effective slope, can improve the extreme runup predictions in these environments.

## **4. Measuring and modelling storm overwash on a gravel barrier**

This chapter presents an investigation of the gravel barrier response under zero and negative freeboard conditions (overtopping and overwash) based on field measurements and numerical modelling. This analysis thereby complements the full range of hydrodynamic regimes that the present research project aims to study.

### **4.1. Introduction**

Gravel barriers are widespread on many high-latitude, wave-dominated coasts around the world (e.g., USA, Russia, UK, Ireland or New Zealand). Their shape and long-term evolution are mainly controlled by three hydrodynamic regimes: (1) swash, when runup is confined to the foreshore (berm formation or beach erosion; e.g., Buscombe and Masselink, 2006); (2) overtopping, when runup exceeds the crest (crest build-up and lowering; e.g., Matias et al., 2012); and (3) overwash, when runup exceeds the crest and promotes major modifications over the entire barrier (barrier transgression via rollover; Carter and Orford, 1993).

Predicting long-term evolution of a gravel barrier requires, therefore, in-depth understanding of the conditions under which each of these regimes occur and their respective morphological impact.

Most of the research on gravel barriers has focused on hydrodynamic conditions within the swash regime, mostly during mild (e.g., Austin and Masselink, 2006; Masselink et al., 2010), but more recently also under energetic wave conditions (e.g., Poate et al., 2013; Almeida et al., 2015). Less

attention has been devoted to gravel barriers under overtopping or overwash conditions and, despite the importance of studies by Orford et al.(1999), Lorang (2002), Orford et al. (2003) and Bradbury et al. (2005), none performed detailed field measurements during these events.

Present understanding of hydro- and morphodynamics on gravel beaches under extreme regimes (overtopping and overwash) relies on qualitative or post-storm information. This reflects the extremely difficult and challenging conditions (typically associated with extreme storms) that these environments present to field instrumentation and field researchers.

To overcome this limitation, recent research effort has been devoted to the investigation of gravel barrier dynamics in controlled laboratory environments (e.g., Obhrai et al., 2008 or Williams et al., 2011). These experiments have provided important insights into the influence of infiltration and exfiltration processes for sediment transport within the swash zone (Masselink and Turner, 2012), the role of antecedent conditions (overtopping and crest build up) in reducing overwash likelihood (Matias et al., 2012), and the definition of thresholds for important morphological changes under varying wave conditions and water levels (Matias et al., 2012).

These laboratory datasets have also provided an important contribution to the development of the predictive skills of the process-based numerical model Xbeach (Roelvink, et al., 2009), initially developed for sandy beaches, but recently adapted for gravel beaches (Xbeach-G; McCall et al., 2014 and 2015). This model accounts for a large number of hydrodynamic processes (e.g., wave transformation, groundwater interactions, runup), together with sediment transport and morphological evolution, on a wave-by-wave time scale. It allows the forecast of the morphological evolution of a gravel barrier under the full spectra of hydrodynamic regimes (swash, overtopping and overwash), and represents a major improvement on existing predictive tools (McCall et al, 2013).

Recent developments in field instrumentation, particularly in remote sensing techniques, have demonstrated the potential to overcome traditional limitations of field experiments on gravel barriers during extreme storm conditions. More specifically, the use of 2D laser-scanners to measure nearshore processes enables the acquisition of high-frequency and high-resolution measurements of the hydrodynamics (e.g., water level and runup) and morphological evolution under extreme storm conditions (Almeida et al., 2013, 2014 and 2015).

The aim of the present Chapter is to present the application of a 2D laser-scanner to the measurement of the hydrodynamics and morphological response of a fine gravel barrier under extreme impact regimes (overtopping and overwash). These field measurements are compared with the predictions of Xbeach-G, and the validated model is used to explore which hydrodynamic conditions define the boundaries of each hydrodynamic regime and their respective morphological impact.

## **4.2. Methods**

### **4.2.1 Study site and field deployment**

The field experiment was conducted on the 1<sup>st</sup> of February 2014 at Loe Bar in the southwest of England (Figure 4.1) with the aim of measuring overwash dynamics (hydrodynamics and morphological response) on a gravel beach during extreme storm conditions.

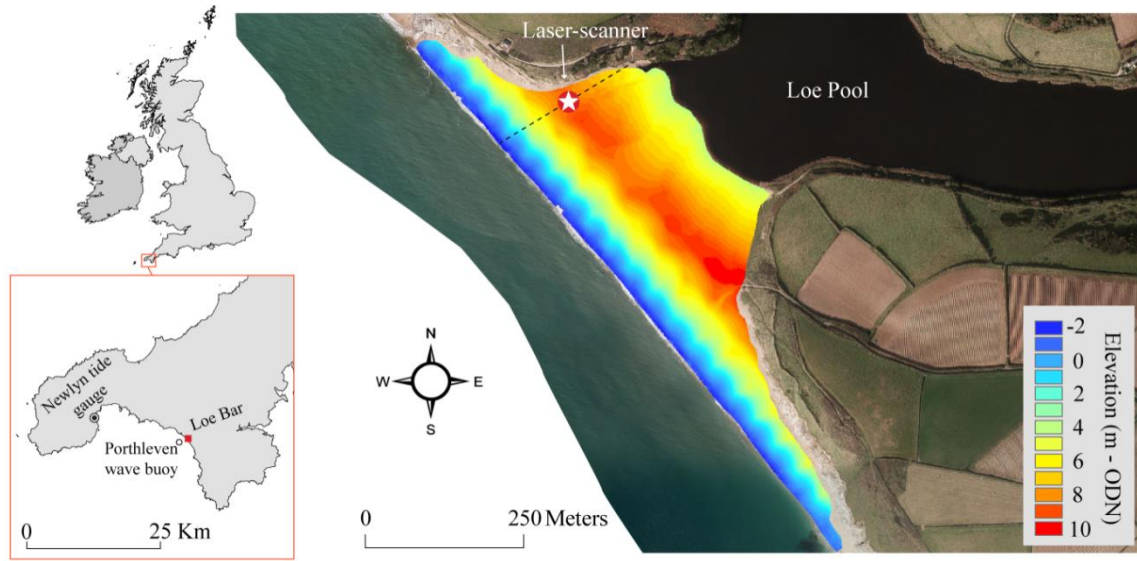


**Figure 4.1** Location of the Loe Bar study site, the Porthleven wave buoy and the Newlyn tide gauge (inset maps). Aerial photograph of Loe Bar with the overlap of the digital terrain model from a Lidar survey (survey performed by the Channel of Coastal Observatory in 2013) with the laser-scanner position and scan profile indicated.

Loe Bar is a fine gravel beach ( $D_{50} = 2\text{--}4\text{ mm}$ ), approximately 1 km long and of variable width (Figure 4.1). The central section of the beach fronts Loe Pool and extends 430 m between the adjacent headlands, with an average width of 250 m, a typical seaward gradient of 0.1 and average crest elevation and backslope of 8.7 and 0.02 respectively. The barrier faces south-west and is exposed to energetic Atlantic swell with an annual average significant wave height ( $H_s$ ) of 1.2 m, an average peak period ( $T_p$ ) of 10 s and a direction ( $\theta_{\text{wave}}$ ) of  $235^\circ$  (wave statistics derived from Porthleven wave buoy measurements, October 2011 to December 2014; data freely available from <http://www.channelcoast.org>). The tidal regime is macrotidal with MHWS (mean high water spring) and MLWS (mean low water spring) at 2.5 m and -2.2 m ODN respectively (Ordnance Datum Newlyn; 0 m ODN  $\sim$  0.2 m above mean sea level in UK coastal waters).

A 2D laser-scanner (SICK - LD-OEM3100) was deployed on the top of an aluminium tower (5.2 m high), fixed to a scaffold frame inserted into the beach near the barrier crest and stabilized by guy ropes (Figure 4.2).

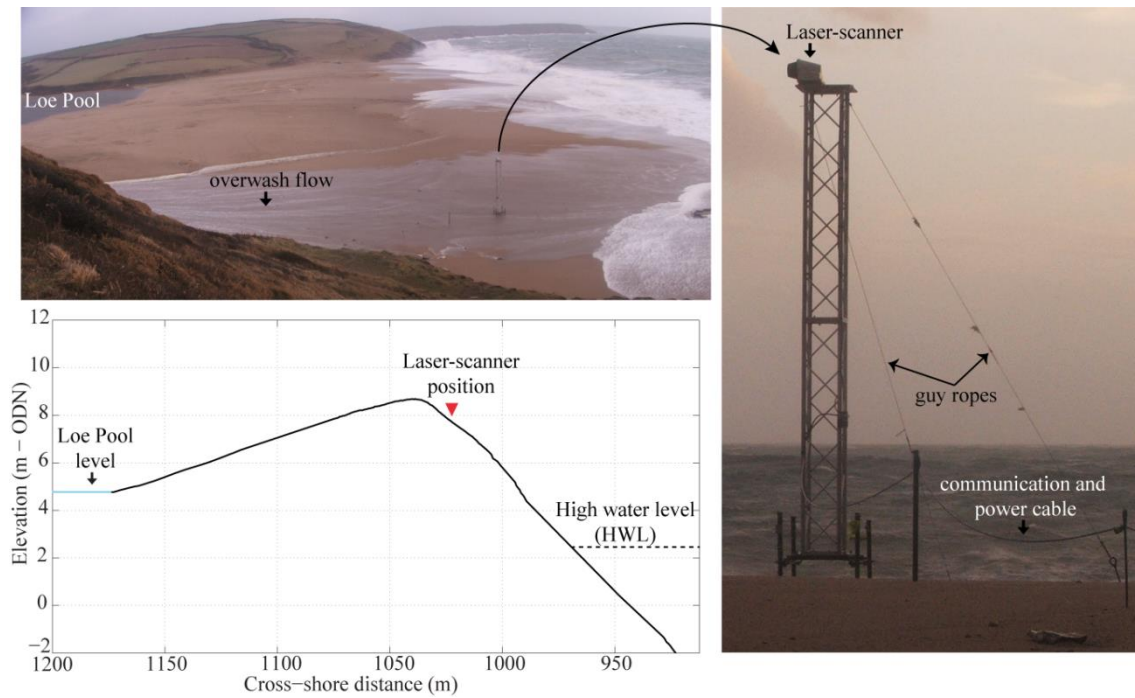


**Figure 4.2** Field photographs showing the laser-scanner setup (right panel) and the deployment of the scanner on the crest of Loe Bar during overwash conditions (top left panel), and detailed cross-shore profile of the barrier indicating position of the laser scanner and sea and lagoon water levels (bottom left panel).

External power supply (28 volts) was provided to the scanner during operation and measurements streamed by an RS422 cable to a laptop, where data were recorded using SOPAS (SICK) software interface. Offshore wave conditions were measured by the Porthleven directional wave buoy located in approximately 15 m water depth at low tide (Figure 4.1). Due to lack of local tide measurements, tide predictions for Porthleven harbour (2 Km northwest of the study site) were corrected by adding the meteorological tide (surge) computed from the difference between the measured and predicted tide at the Newlyn tide gauge (Figure 4.1).

#### 4.2.2 2D Laser-scanner

The LD-OEM3100 (manufactured by SICK) laser scanner model was selected for the present work. The description of the working principles and data processing are described in Chapter 2.

After this initial data processing, the laser measurements are separated in two distinct time series: (1) continuous beach topography; and (2) swash hydrodynamics (including water elevation and runup edge). These time series form the basis of the analysis of the present work. An example of the type of measurements performed during this field experiment is shown in Figure 4.3 and illustrates the ability of the laser-scanner in tracking the entire overwash process.

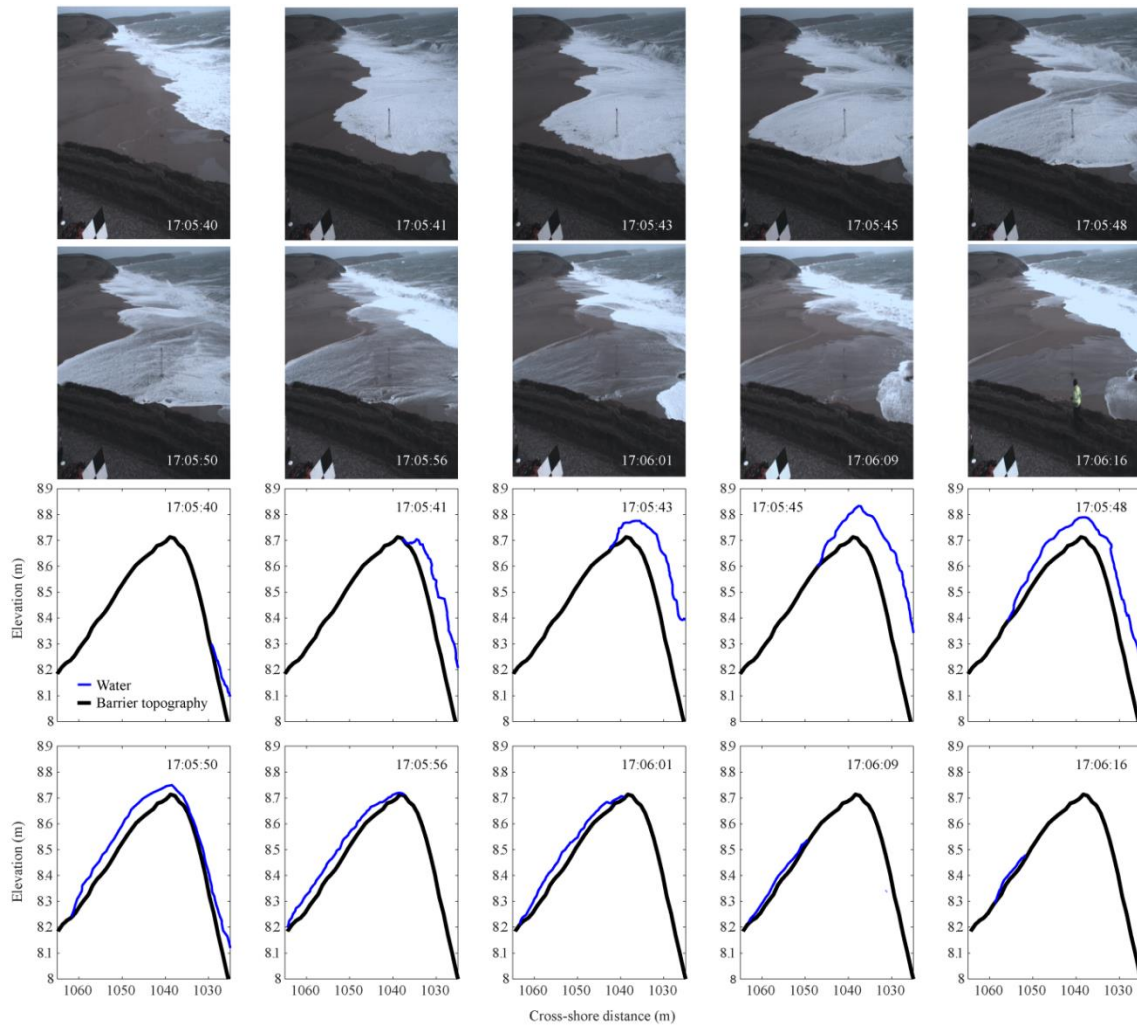


**Figure 4.3** Sequence of video snapshots (top) and corresponding laser-scanner measurements (bottom) during an overwash event over the barrier.

From these observations it is possible to quantify the free surface of the entire wave overwash event, including the wave runup on the beach face (17:05:40-41s – Figure 4.3), the overtopping of the crest (17:05:43s), the wave intrusion and propagation into the back of the barrier until reaching

the Loe lagoon (17:05:45-56s), and the infiltration on the overwash body into the gravel bed on the back of the barrier (17:06:01-16s). As the water body infiltrates into the bed or returns to the sea (backwash), the surface of the barrier becomes exposed, allowing the laser-scanner to quantify any morphological changes (e.g., 17:06:16 s).

### 4.2.3 Xbeach-G model description

To explore the morphological impact of the full range of hydrodynamic regimes under different freeboard levels on a gravel barrier, the process-based numerical model Xbeach-G (McCall et al., 2014) was first validated using the field data and then implemented to investigate different forcing scenarios. This model is an extension of the existing Xbeach open-source storm morphodynamic model (Roelvink et al., 2009), specifically adapted for gravel beaches. In contrast to Xbeach, Xbeach-G uses a one-layer, depth-averaged, non-hydrostatic scheme, similar to the SWASH model (Smit et al., 2013), that allows the solution of wave-by-wave flow and surface elevation variations due to short waves in the nearshore zone. This aspect is particularly important on pure gravel beaches where swash motion is mainly at incident frequencies (Buscombe and Masselink, 2006). The most important equations implemented in Xbeach-G to solve the nearshore hydrodynamics are described in Chapter 3. Here only the newly developed sediment transport and morphodynamic model of Xbeach-G (McCall et al., 2015) is described.

Sediment mobility is defined in XBeach-G by the Shields parameter ( $\theta$ ):

$$\theta = \frac{\tau_b}{\rho g \Delta_i D_{50}} \quad (4.1)$$



where  $\Delta_i$  is the effective weight of the sediment,  $\tau_b$  is the bed shear stress (see Chapter 3),  $\rho$  is the density of the water,  $g$  is the acceleration due to gravity, and  $D_{50}$  is the median grain size.

To account for vertical through-bed flow, the effective weight ( $\Delta_i$ ) is modified by the vertical groundwater pressure gradient following Turner and Masselink (1998):

$$\Delta_i = \frac{\rho_s - \rho}{\rho} + \alpha \frac{S}{K} \quad (4.2)$$

where  $\rho_s$  is the density of the sediment,  $\alpha$  is an empirical constant relating the surface seepage force to the seepage force in the bed (set to 0.5 – see McCall et al., 2015),  $K$  is the hydraulic conductivity of the aquifer, and  $S$  is the surface water-groundwater exchange flux (see Chapter 3).

When a sloping bed is present, the effective Shields parameter is modified according to Fredsøe and Deigaard (1992):

$$\theta' = \theta \cos(\beta) \left( 1 \pm \frac{\tan(\beta)}{\tan(\emptyset)} \right) \quad (4.3)$$

where  $\beta$  is the bed slope,  $\emptyset$  is the angle of repose of the sediment (for gravel, this is within 30° - 40°), and the right-hand term is  $< 1$  for up-slope transport, and greater than  $> 1$  for down-slope transport.

The dominant modes of sediment transport on gravel beaches are assumed to be bed load and sheet flow transport (Buscombe and Masselink, 2006). The total gravel sediment transport is computed using the bed load transport equation of Van Rijn (2007):

$$q_b = \gamma D_{50} D_*^{-0.3} \sqrt{\frac{\tau_b}{\rho}} \frac{\theta' - \theta_{cr}}{\theta_{cr}} \quad (4.4)$$

where  $q_b$  is the volumetric bed load sediment transport rate,  $\gamma$  is a calibration coefficient (set to 0.5 following Van Rijn (2007)),  $D_* = D_{50} \left( \frac{\Delta g}{\nu^2} \right)^{\frac{1}{3}}$  is the non-dimensional grain size,  $\nu$  is the kinematic viscosity coefficient of water, and  $\theta_{cr}$  is the Shields parameter for the initiation of transport. This parameter is computed using the Soulsby & Whitehouse (1997) equation:

$$\theta_{cr} = \frac{0.3}{1 + 1.2D_*} + 0.055(1 - e^{-0.020D_*}) \quad (4.5)$$

XBeach-G is a one-line model (i.e. only models cross-shore profile), and the bed-level changes are computed from the cross-shore gradient in the sediment transport, which itself is computed from:

$$\frac{\partial \xi_b}{\partial t} + \frac{1}{1-n} \frac{\partial q_b}{\partial x} = 0 \quad (4.6)$$

where  $\xi_b$  is the elevation of the bed above an arbitrary horizontal plane and  $n$  the porosity. Slope collapse is simulated by avalanching material down-slope when the bed slope exceeds the angle of repose ( $\phi$ ).

$$\left| \frac{\partial \xi_b}{\partial x} \right| > \phi \text{ avalanching} \quad \text{and} \quad \left| \frac{\partial \xi_b}{\partial x} \right| \leq \phi \text{ no avalanching} \quad (4.7)$$

Xbeach-G hydrodynamics (McCall et al., 2014) and morphodynamics (McCall et al., 2015) have been extensively validated using laboratory (Williams et al., 2011) and field datasets (Poate et al., 2013), with results showing that the model has very good skills in predicting both aspects. However, none of the validation datasets included direct and continuous measurements of overtopping and overwash conditions on a natural gravel barrier.

## 4.3 Results

### 4.3.1 Waves, tides and laser-scanner measurements

During the field experiment, storm waves from the southwest ( $\sim 240^\circ$ ) with significant ( $H_s$ ) and maximum ( $H_{\max}$ ) wave heights of 4 m and 8 m, respectively, were recorded at offshore depths (Porthleven wave buoy), with peak periods ( $T_p$ ) ranging from 10 to 15 seconds (Figure 4.4). Despite the small storm surge level observed at Newlyn tide gauge ( $\sim 15$  cm) the peak of the storm coincided with the peak of a spring high tide (2.45 m), thus providing optimal conditions for the occurrence of overwash events (Figure 4.4).

Interestingly during this storm event the offshore wave buoy recorded waves with a bimodal spectrum shape (Figure 4.4), indicating that this event was a result of two distinct swell events, one with shorter wave periods ( $T \sim 10$  s) and another with longer wave period ( $T \sim 16$  s – Figure 4.4).

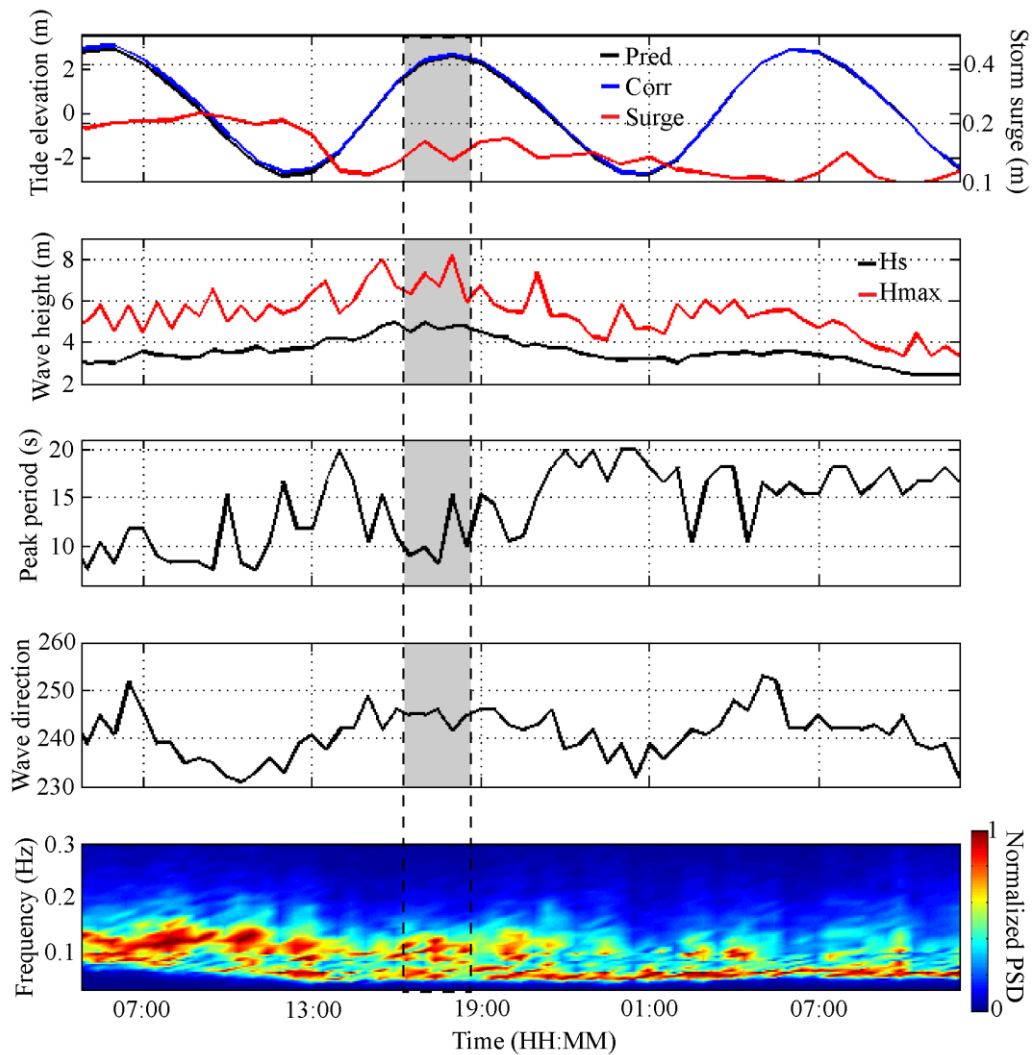


**Figure 4.4** Corrected tide level and surge measurements for Porthleven harbour (top panel); offshore wave conditions, including significant and maximum wave height (second panel), peak period (third), wave direction (fourth panel) and normalised spectra (bottom panel), measured at Porthleven offshore wave buoy; shaded area corresponds to the period of time when laser measurements were performed.

The measurements performed with the laser-scanner lasted approximately 2 hours and 30 minutes and covered the most energetic period of the storm, during which numerous overtopping and

overwash events were observed (Figure 4.5). Measurements included: vertical and horizontal runup excursions ( $R_z$  and  $R_x$  respectively) and morphological response (Figure 4.5).

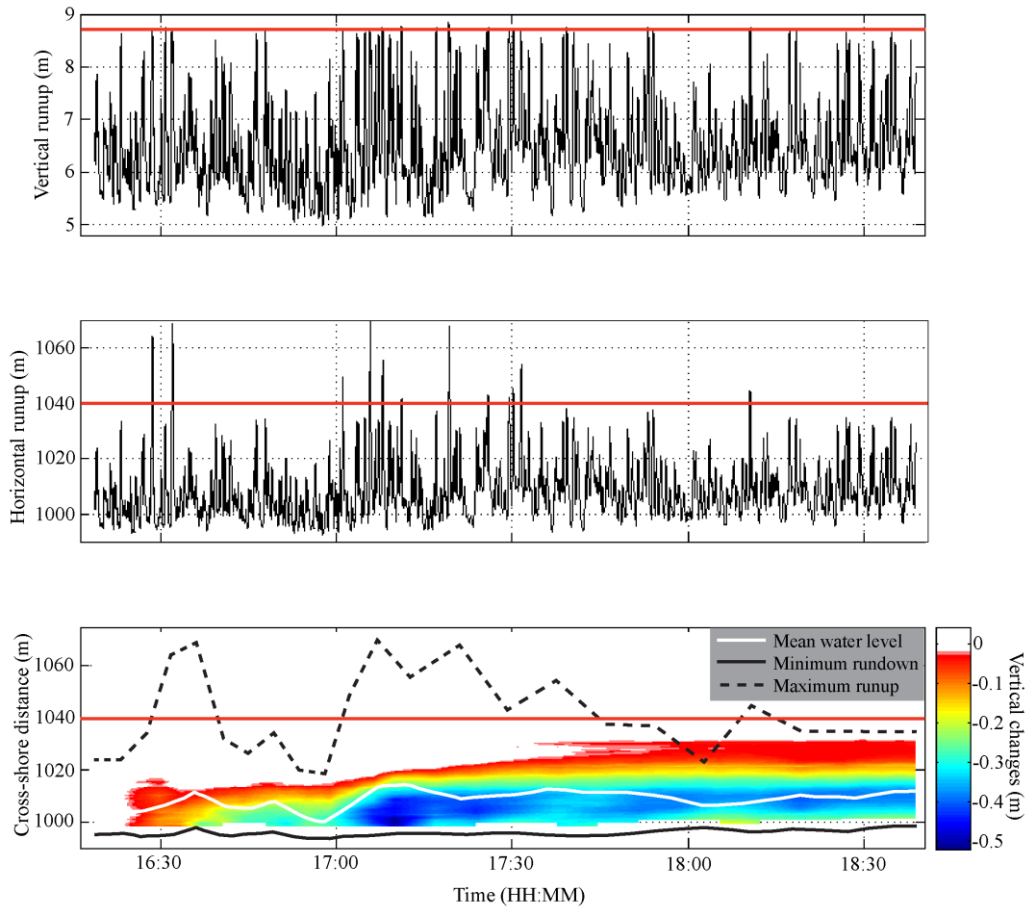


**Figure 4.5** Vertical (top panel) and horizontal (second panel) runup excursions and morphology cumulative changes (bottom panel) measured by the laser-scanner. Red line indicates the location of the crest of the barrier.

Time series of vertical runup show that a large number of waves reached close to the crest of the barrier ( $> 8$  m ODN), although only a small percentage of these did actually overtop or overwash the barrier, as the time series of horizontal runup illustrate (Figure 4.5). The measured vertical rundown limit is between 5 and 6 m (ODN), which is relatively high, taking in consideration that the high tide elevation was approximately 2.6 m (predicted tide + surge). This result is likely to be due to the lack of coverage of the laser-scanner in the lower swash zone, as a result of the limited

range of this particular laser-scanner or the low angle of incidence of the laser beam (low returns) on the lower part of the swash (Almeida et al., 2015).

The cumulative morphological changes observed by the laser-scanner during this storm event show that the only significant modification of the barrier occurred on the seaward side of the barrier, with the erosion of the mid swash zone (between  $x = 1000$  and  $1030$  m - Figure 4.5). The patch of erosion starts at approximately 16:30 (Figure 4.5) when the first overwash events occurred, and with the rising of the tide this patch moves onshore. The peak of erosion (beach erosion by about  $0.5$  m) occurs between 17:00 and 17:30, when a group of waves overwash the barrier and also when a large number of runup events reach close to the barrier crest (Figure 4.5).

One of the most important overwash parameters in determining the potential of flooding and damage on the barrier is overwash discharge. Typically this parameter is measured in the field by a combination of traditional *in-situ* instruments, such as electromagnetic current-meters and pressure transducers (e.g., Leatherman, 1976), although recent laboratory experiments suggest that these types of measurements can be estimated by semi-remote sensing methods, such as ultrasonic bed-level sensors (e.g., Matias et al., 2014). In the present experiment the overwash discharge was estimated by computing the product of the overwash depth ( $h_c$ ) and overwash front velocity ( $u_{crest}$ ) at the crest of the barrier:

$$q_c = h_c \cdot u_{crest} \quad (4.8)$$

Note that this method will provide an upper bound estimate of discharge because it is based on the initial crest velocity which is expected to subsequently reduce. Other problems can arise from the use of the bore front velocity method for computing the flow velocity, such as the slope of the back of the barrier (which can accelerate or reduce the flow velocity) or the presence of variable sediment sizes that can offer different resistance to the flow (due to friction and infiltration).

Despite these limitations this method has been successfully applied by other authors on gravel (Matias et al., 2014) and sandy (Matias et al., *in press*) barriers.

For each overwash event the water depth and velocity recorded by the laser-scanner at the crest of the barrier (Figure 4.6) was used to compute a time-series of overwash discharge. An example of this type of measurement is presented in Figure 4.6, where it is possible to observe the intrusion of one overwash event over the crest of the barrier with maximum water depth of 12 cm and maximum velocity of 3.8 m/s, producing a mean and maximum overwash discharge of 0.2 l/s/m and 0.33 l/s/m respectively (Figure 4.6)

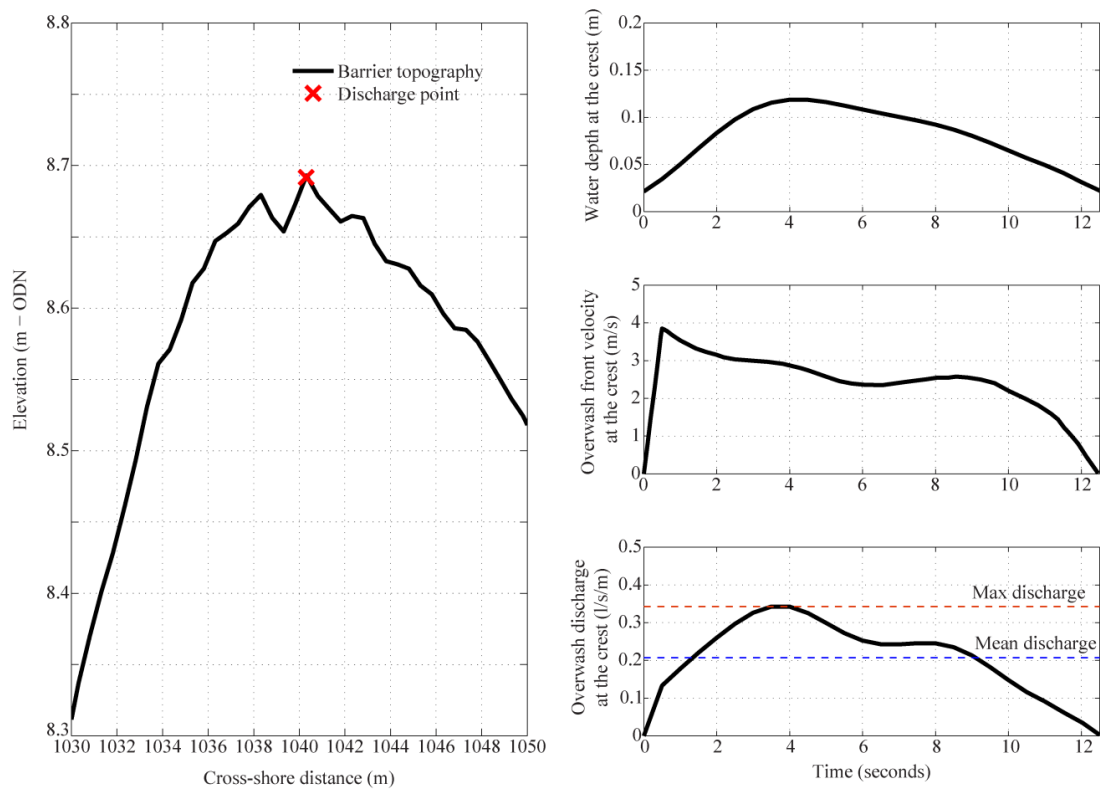


**Figure 4.6** Cross-shore barrier profile with location of the point (red cross) where overwash discharge was computed (left panel) and example time series of water elevation (top right panel), overwash front velocity (middle right panel) and estimated overwash discharge (bottom right) for a single overwash event measured by the laser-scanner.

The same procedure was applied to compute mean and maximum overwash discharge for all the overwash events measured by the laser-scanner (Figure 4.7). Results show that a variety of

overwash events were measured during the present field experiment, with several events overtopping the crest of the barrier but with limited horizontal intrusion across the back of the barrier (e.g., numbers 3, 6, 8, 9, 10, 11 and 12 – Figure 4.7), while another group had larger horizontal intrusion, reaching the Loe lagoon (overwash numbers 1, 2, 4 and 7 – Figure 4.7).

Average overwash depths measured at the crest of the barrier ranged from 4 to 14 cm, with maximum depths reaching 21 cm, and average flow velocities varied from 0.05 to 4 m/s with maximum records reaching 6.3 m/s (Figure 4.7). These values are within the range of observations presented by Matias et al., (2014) as the result of a large laboratory experiment, although field measurements of these parameters have not been hitherto reported.

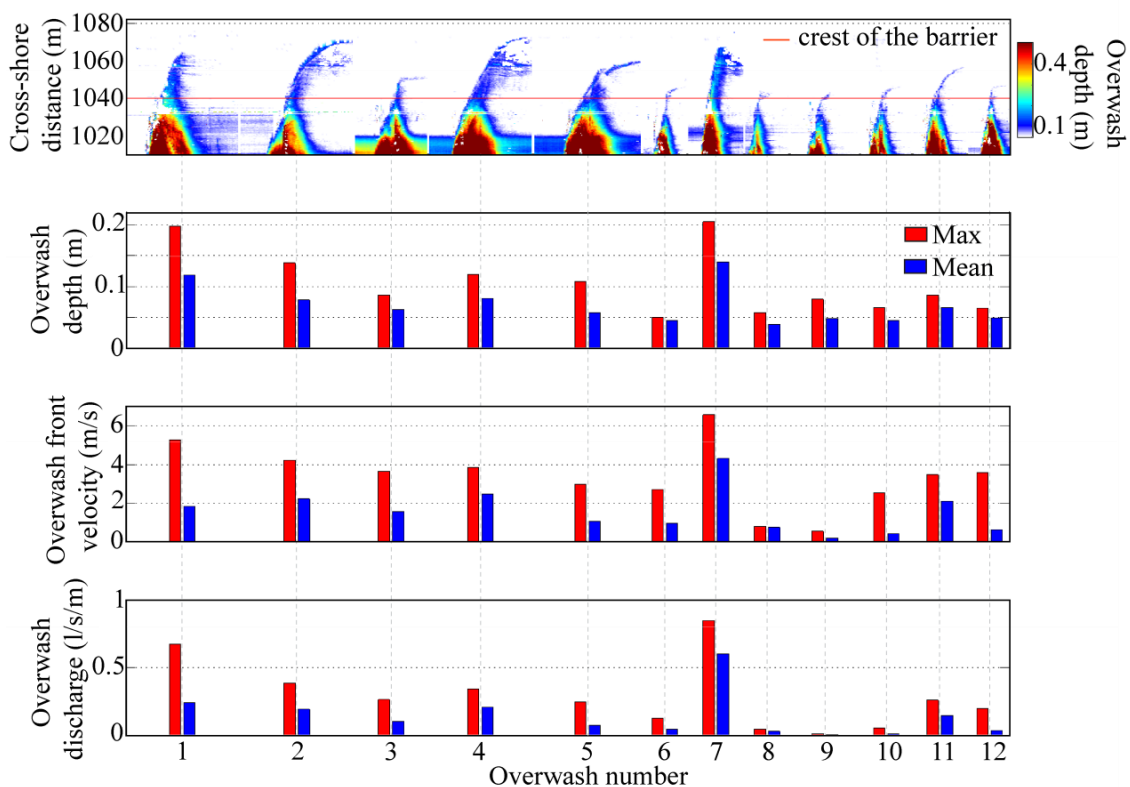


**Figure 4.7** Characteristics of the overwash events measured by the laser-scanner: time series of overwash depth for each event (top panel); average and maximum overwash depth (second panel); average and maximum overwash front velocity (third panel); and average and maximum overwash discharge (bottom panel).



Due to the scarce observational data and intrinsic logistical difficulties in gathering field measurements during overwash events, several researchers who have attempted to establish a relationship between overwash depth and velocity in order to predict overwash velocities. This relationship is typically assessed by the dam break equation, which has also been used for the tip of bores in the swash zone (e.g., Jiang et al., 2010):

$$u_{crest} = 2\sqrt{gh_c} \quad (4.9)$$

where  $u_{crest}$  and  $h_c$  are the velocity and depth respectively measured at the crest, which in this case are represented by the overwash velocity and depth, and  $g$  is the gravitational acceleration. The present field observations were used to explore this relationship (Figure 4.8) and results show that the dam break equation has a very low capacity to explain the present observations. The deviation from the dam break curve is more significant for maximum overwash velocities, although even the average overwash velocities shown seem to have a different relationship with overwash depth (Figure 4.8). Despite the relatively small range of velocities and water depths used in this comparison, it seems clear that this equation does not adequately explain the hydrodynamic processes of overwash flow over this barrier. This statement is supported by the fact that a linear fit was the better adjustment achieved with this dataset instead of a power fit (Figure 4.8).

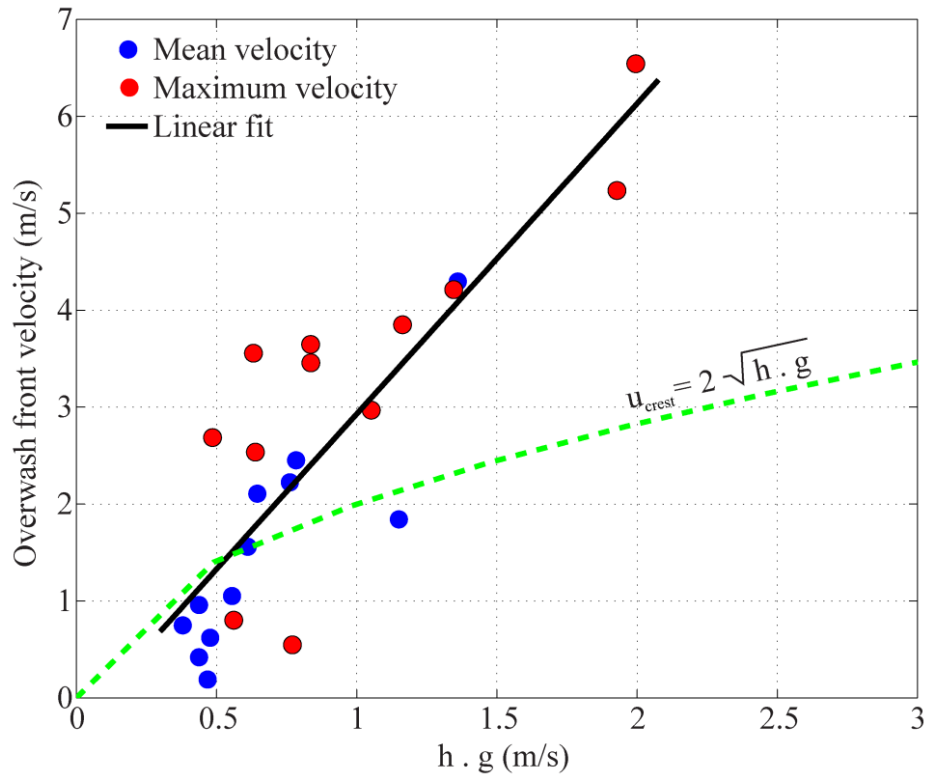


**Figure 4.8** Mean and maximum overwash front velocity at the crest as a function of mean and maximum overwash depth at the crest \* gravitational acceleration (g). The dam break equation is plotted in the figure (green dashed line) together with a linear fit (black line) between these two parameters.

One reason for such a difference might be due to the fact that dam break assumes that the initial condition of the water at the crest is static, while, on a natural beach, the overwash flow at the crest is a result of a wave runup excursion that carries some momentum before passing the crest of the barrier. With larger runup excursions, it is expected that the greater water depths and higher runup velocities will bring greater momentum to the overwash velocity at the crest, as the linear fit suggests (Figure 4.8).

## 4.3.2 Xbeach-G validation

### 4.3.2.1 Hydrodynamics

The field measurements were used to validate Xbeach-G by comparing measured and modelled overwash discharge, extreme runup and the frequency of overwash events.

The model bed level was set to the bed measured along the laser-scanner profile, with the sub-tidal section (measured by a previous bathymetric survey) of the profile extended to -18 m (ODN) depth (Figure 4.9). The cross-shore resolution of the model grid was set to vary gradually in the cross-shore direction to correctly capture wave breaking and runup in the model, with an approximate resolution of  $\sim 2\text{--}3$  m at the offshore boundary and 0.1 m near the waterline.

The grain size properties and hydraulic conductivity of the beach used in the present simulations was derived from McCall et al., 2014 (Table 4.1).

$D_{50}$ (mm)	$D_{90}$ (mm)	$K$ (mm s <sup>-1</sup> )
2	3	3

**Table 4.1** Sediment properties used in the simulations.

For each simulation, the model was forced with measured wave spectra retrieved from Porthleven wave buoy, and tide predictions for Porthleven harbour, corrected for the surge levels measured at Newlyn tide gauge.

To test the effect of considering groundwater interactions and morphological evolution, four different model setups were prepared. For Setup 1, the groundwater module was turned on and the bed was fixed during the entire duration (using the initial profile measured in the field). For Setup 2, the groundwater module was on and the morphology was “manually” updated (the measured morphological changes along the laser-scan profile were fed back into the model during the simulation, and the sediment transport and morphological model was set off; see Figure 4.9) every

10 minutes, using the same approach implemented by McCall et al. (2014). For Setup 3, the groundwater was turned off and the bedform was not updated. For Setup 4, groundwater was turned off and morphology was updated every 10 minutes.

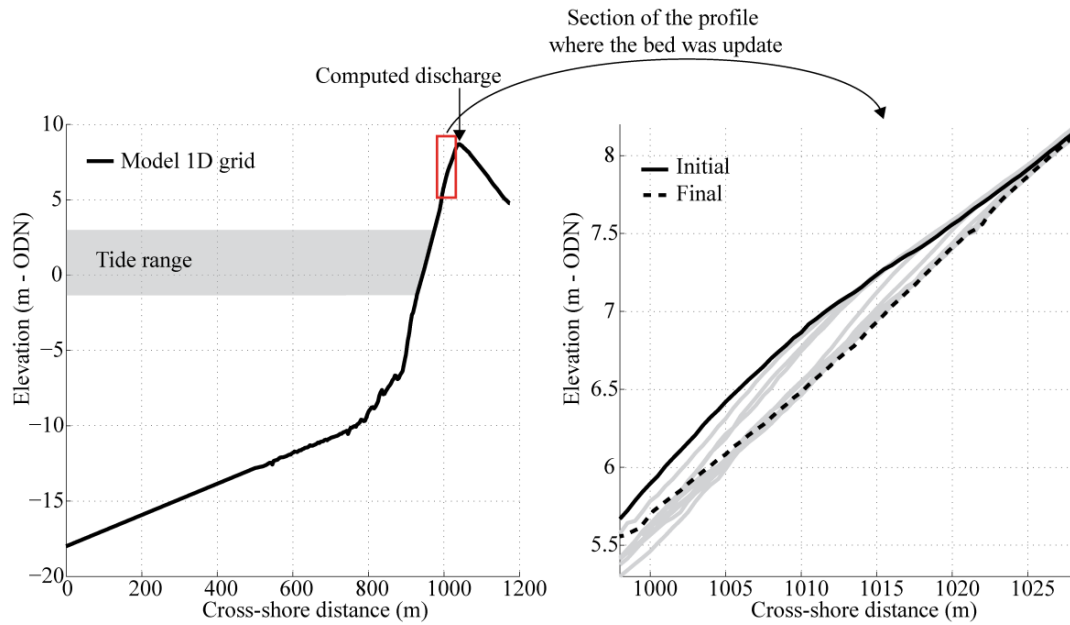


**Figure 4.9** Cross-shore profile used for the model validation (left panel), and example of the bed evolution for Setups 2 and 4 (right panel).

An example of the model outputs is shown in Figure 4.10. These results show that runup time series (vertical and horizontal) present values within the range of laser measurements. It is possible to verify that the average backwash limit is lower than what was observed by the laser-scanner, although it is impossible to compare this aspect with the measurements, since, as explained above, the laser was not able to reach the lower swash zone during this experiment.

Overwash discharge predictions (Figure 4.10) also show values within the range of observations, providing a positive overall visual assessment of model skill.

In order to quantitatively compare model predictions and field observations, the following parameters were computed: 1) 2% exceedance vertical runup ( $R_{2\%}$ ), 2) number of overwash events,

and 3) average and maximum overwash discharge. The results are presented in Table 4.2 and show that, in general, XBeach-G was able to reproduce results close to the field observations.

The extreme runup predicted by XBeach-G slightly underestimates the field observations (4.6% less when groundwater was on and less than 3% when groundwater was off – Table 4.2) and therefore this was also reflected on the number of overwash events predicted by the model. The only exception was the model simulations using groundwater off and no bed update (Setup 3), which predicted exactly the same number of overwash events as were measured in the field (Table 4.2).

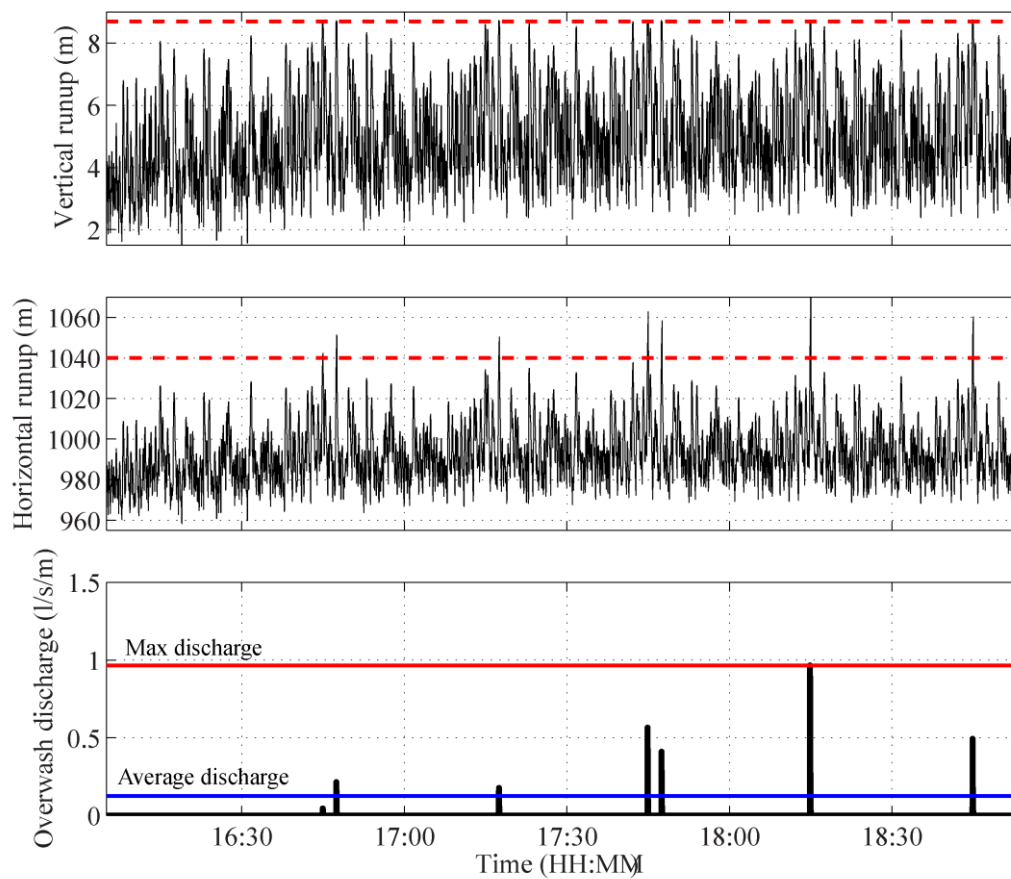


**Figure 4.10** Example of XBeach-G output for the simulations with Setup 1, showing the time series of vertical (top panel) and horizontal (middle panel) runup and the overwash discharge (bottom panel) computed for the storm conditions observed during the present experiment. Red dashed line indicates the position and elevation of the barrier crest.

The results show that average and maximum overwash discharge was better predicted when the model was using groundwater on and slightly overestimated the maximum overwash discharge when the groundwater was set off (Table 4.2).

	Measured	Setup 1	Setup 2	Setup 3	Setup 4
<b>Morphology</b>	-	fixed	update	fixed	update
<b>Groundwater</b>	-	on	on	off	off
<b><math>R_{2\%}</math> (m)</b>	6.5	6.2	6.2	6.4	6.3
<b>Overwash events</b>	12	7	7	12	10
<b>Average discharge (l/s/m)**</b>	0.14	0.12	0.1	0.11	0.07
<b>Maximum discharge (l/s/m)**</b>	0.84	0.96	0.88	1.26	1.21

\*\* Discharge is the average for the period of time that measurements were performed.

**Table 4.2** Results of the comparison between Xbeach-G

#### 4.3.2.2 Morphodynamics

To determine the skill of Xbeach-G in predicting the morphological response of the gravel barrier during storm conditions, the model was set up using the beach profile measured at the beginning of the experiment (initial profile – Figure 4.9) and forced with offshore wave conditions observed during the present experiment at the Porthleven wave buoy. Tidal level predictions for Porthleven harbor were corrected for the meteorological tide (surge) using the measured storm surge at Newlyn tide gauge. Two models were set up: one with the groundwater module on, and the other model with groundwater off. To compare the model results with the field measurements, simulations were performed to cover exactly the same period of time when the laser-scanner measurements of the topography were performed.

To assess the overall performance of the model, the measured and modelled final profiles were compared; to verify the performance of the model during the time, the measured and modelled cumulative morphological changes were plotted together (Figure 4.11).

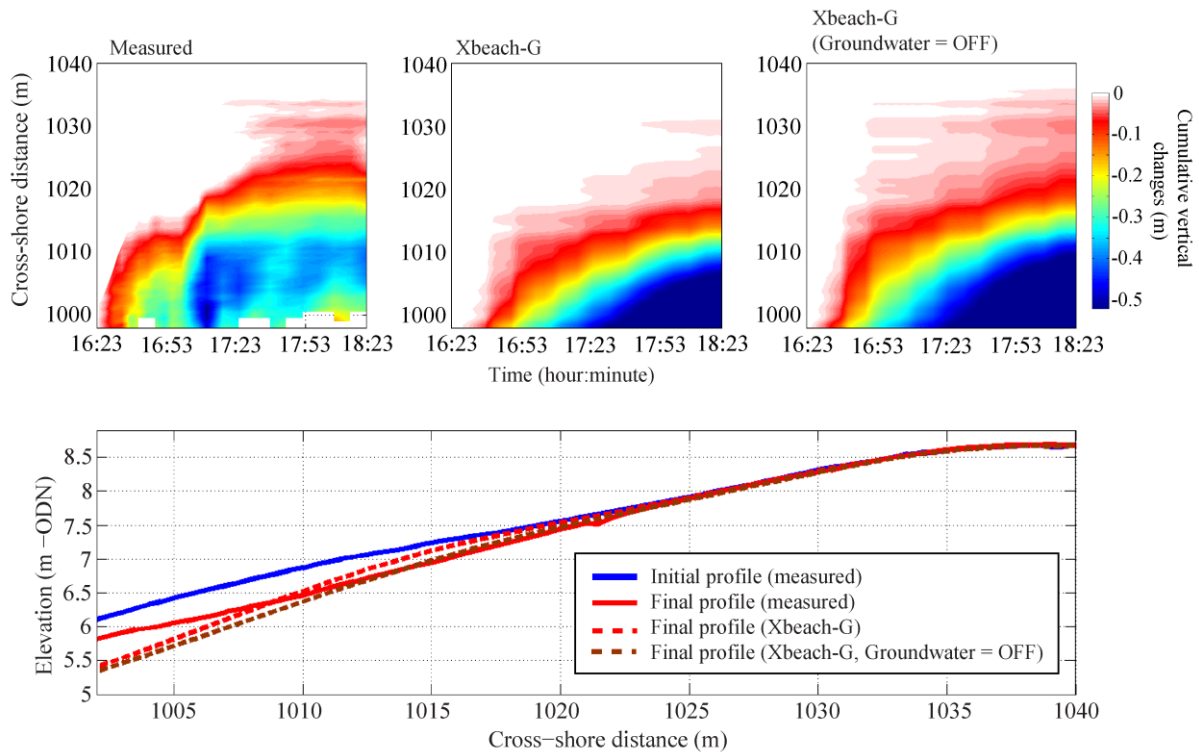


**Figure 4.11** Comparison between measured and modelled morphological response to a storm event, with the top panels showing the cumulative vertical changes and the bottom panel comparing the initial measured profile with the final measured profile and those predicted by Xbeach-G. Two XBeach-G models were run: groundwater = ON and groundwater = OFF.

The Xbeach-G model predictions compare very well with the field observations. Despite a small underestimation of the erosion at the top and overestimation at the lower section of the profile, overall the model was able to capture very well the shape of the changes along the entire profile (Figure 4.11).

### 4.3.3 Overtopping and overwashing discharge under variable wave height and water levels

Wave runup can exceed the barrier crest under storm and non-storm conditions, when the combination of the water levels and wave conditions allows this (Morton et al., 2000). To investigate and quantify the conditions under which the Loe Bar barrier overwashed, 64 Xbeach-G simulations were performed, using combinations of eight significant wave heights ( $H_s$  1–8 m) and eight water levels (1–8 m), and a fixed peak wave period ( $T_p = 10$  s) and mean wave period ( $T_m = 8.4$  s; representing the average wave period calculated from 4 years of measurements at Porthleven wave buoy). Each model was set up using the measured pre-storm profile (Figure 4.6), and the forcing waves were characterized by the standard unimodal Jonswap spectrum ( $\gamma = 3.3$ ). Each model was run for 5400 s (1 h and 30 min) with stationary water level, with the initial 1800 s used to spinoff the model and the remaining 3600 s for analysis.

Figure 4.12 shows the results of the simulations by means of a contour map of overwash discharge under variable water levels and wave heights. To contextualize these discharge values in terms of potential damage to the barrier (e.g. damage to the crest or back of the barrier), three main hydrodynamic regimes that occur at Loe Bar barrier under storm or non-storm conditions were identified. Swash regime is representative of cases when runup is confined to the foreshore, when no overtopping is observed (white area on the map -Figure 4.11), while overtopping and overwash regimes describe conditions when the wave runup exceeds the crest of the barrier.



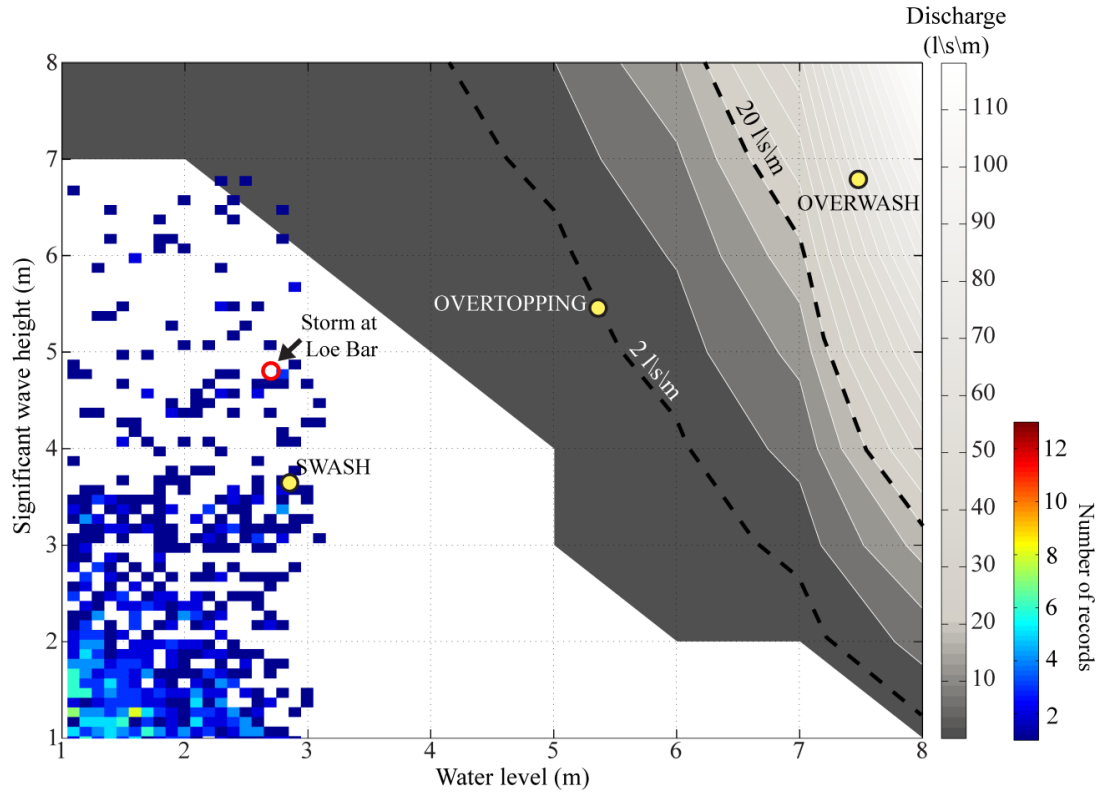


**Figure 4.12** Contour map of the average wave overtopping and overwash discharge under different significant wave height and water level conditions, overlain by a bivariate histogram of measured  $H_s$  and water level for waves with  $T_p > 10$  s (wave data source: Porthleven wave buoy; tide source: Newlyn tide gauge). The yellow dots represent the mid-regime forcing conditions for which the effect of changing wave period, spectral shape and groundwater interactions will be explored later in this chapter.

To identify the boundary between overtopping and overwash regime, the approach used by McCall et al., (2012) was followed. It defines the threshold for overwash discharge based on engineering guidelines for the stability of rip-rap structures under overwash conditions. According to these guidelines (Simm, 1991; Frizell et al., 1998), an average overwash discharge above 20 l/s/m is expected to cause severe damage to the crest and back of the barrier; therefore, that value was used here to define the threshold for an overwash regime.

By overlapping the joint distribution of waves and tides (based on four years of wave and tide measurements, for  $T_p > 10$  s) on the discharge map (Figure 4.12), it is clear that only a very small number of actual observations lie within the overtopping domain, and none inside the overwash

regime. A preliminary interpretation of this result is that Loe Bar has an extremely low vulnerability to overtopping and overwash events. This assumption is supported by recent studies performed at this site (e.g., Poate *et al.*, 2013 or Almeida *et al.*, 2015), which observed a lack of overtopping even under energetic wave conditions.

Interestingly, on the current discharge map, the present storm measurements fall within the swash regime (red dot – Figure 4.12), when, according to field measurements and model validation (e.g., Table 4. 2), this result should be within an overtopping regime. An important difference between the model setup during the validation section and the regime analysis was the fact that, in the validation section, the bimodality of the offshore wave spectrum was taken in account, whereas, on the discharge map, the simulations were performed using a unimodal spectrum shape.

Previous authors have shown bimodality of offshore wave spectra to be an important factor when considering the prediction of wave runup on gravel beaches (Polidoro *et al.*, 2013) and potentially the overtopping discharge (Masselink *et al.*, 2014).

To investigate why the present storm conditions do not fall within the overtopping regime in Figure 4.12, two new model simulations were performed using a bimodal Jonswap wave spectrum with similar shape to the measured wave spectrum (measured at Porthleven wave buoy) and another model using a unimodal Jonswap wave spectrum with identical  $H_s$  and  $T_m$  (Figure 4.13).

The results of these two model simulations show that overtopping discharge at the crest occurs when the model was forced with a bimodal wave spectrum, but no discharge when a unimodal wave spectrum was used (Figure 4.13). This result confirms that the presence of a bimodal wave spectrum can enhance the occurrence of overwash. The fact that the present storm did not fall within the overtopping regime was merely due to the present regime map being produced with unimodal wave spectrum shape.

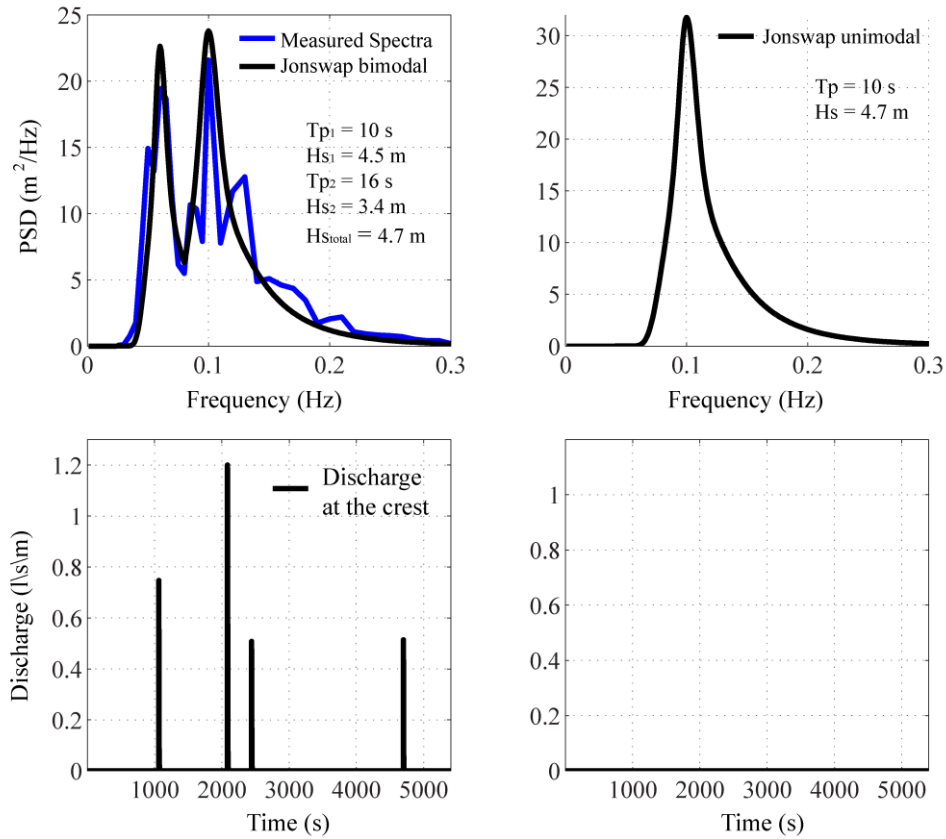


**Figure 4.13** Results of the overtopping discharge (lower panels) computed using a bimodal (top left panel) and unimodal Jonswap spectra (top right panel) with the same  $T_m = 10$  s and  $H_s = 4.7$ , using gamma = 2.

The wave spectrum was computed for each time series of water elevations predicted for each cross-shore position of the grid, and is presented in Figure 4.14. The results show that, for the bimodal wave forcing, the lower frequency energy increases towards the shore (from  $x = 600$  to  $900$  m), whereas the shorter frequency energy dissipates (Figure 4.14). The swash zone becomes dominated by the longer period waves, producing a wider swash zone, and there is development of infragravity waves (Figure 4.14). When the model was forced with the unimodal wave spectrum, the peak period waves were dissipated significantly before reaching the swash zone (between  $x = 0$  and  $600$  m), and swash zone width is slightly narrower than that which developed under bimodal wave spectrum (Figure 4.14). No apparent development of energy on the infragravity band was found under unimodal wave spectrum conditions and no overwash occurred (Figure 4.14).

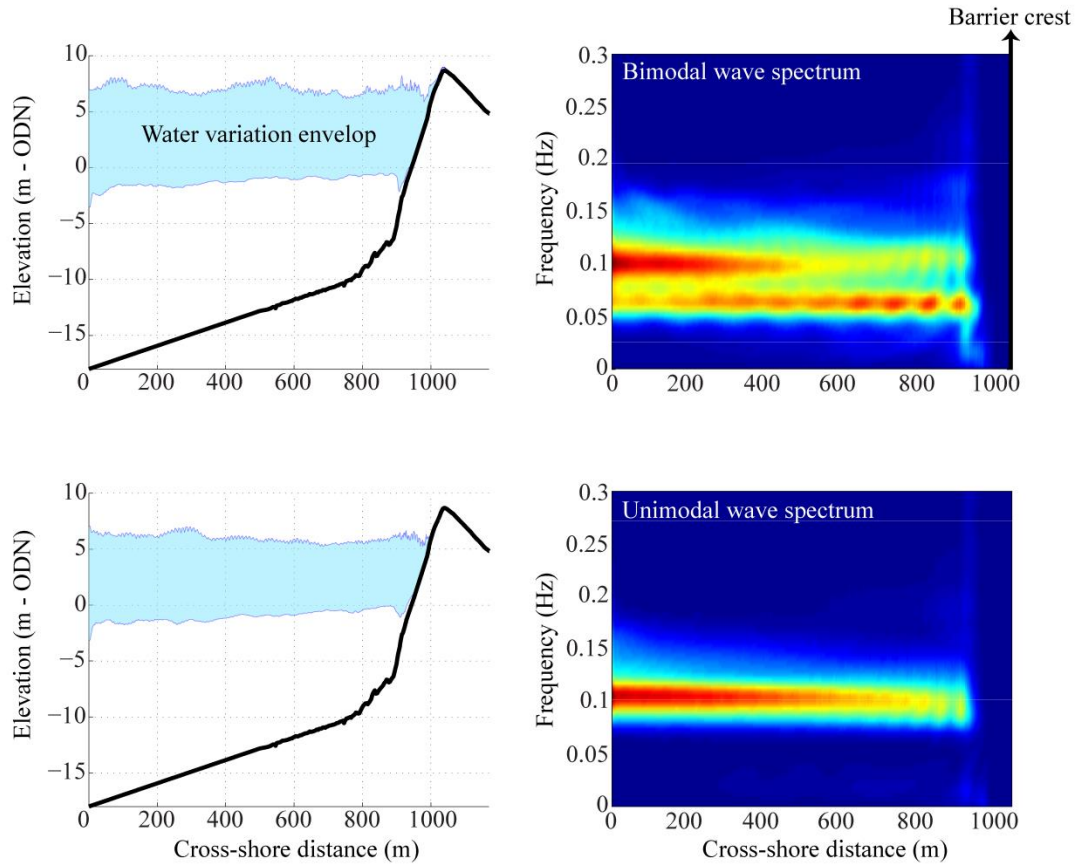


**Figure 4.14** Wave spectrum computed for each time series of water elevations predicted for each cross-shore position of the grid from the model outputs presented in Figure 4.13.

#### 4.3.4 The effect of wave period, spectral shape and groundwater on the definition of storm impact regimes

To quantify the effect of wave period, spectral shape and groundwater on the impact regimes identified in Figure 4.12, a new set of Xbeach-G model runs was formulated. Three categories of simulations were defined, one per regime (swash – overtopping – overwash), and for each regime category a representative value of water level and  $H_s$  was used as a constant during all the simulations (see yellow dots in Figure 4.12). To enable a fair comparison between the different spectral shapes, the mean period  $T_m$  ( $T_m = m_1/m_0$ , where  $m_1$  and  $m_0$  represent the first and zero

moment of the wave spectrum, respectively) was kept constant, independently of whether a bimodal or unimodal spectrum was employed. The details of the  $H_s$  and  $T_p$  values calculated for spectrum are provided in Appendix I.

To test the role of wave period, a total of 30 Xbeach-G models was set up (10 per regime) for 10 classes of  $T_m$  (from 5–12 s) using a standard unimodal wave spectrum (Figure 4.16). The 30 simulations were carried out both with and without the groundwater module turned on. Finally, an additional set of 90 simulations was set-up to investigate the role of spectral shapes on swash and overwash dynamics. In addition to the unimodal wave spectrum, two bimodal Jonswap spectra were designed by adding a long period swell ( $T_{p(swell)} = 15$  s) to the unimodal spectrum (Figure 4.15).

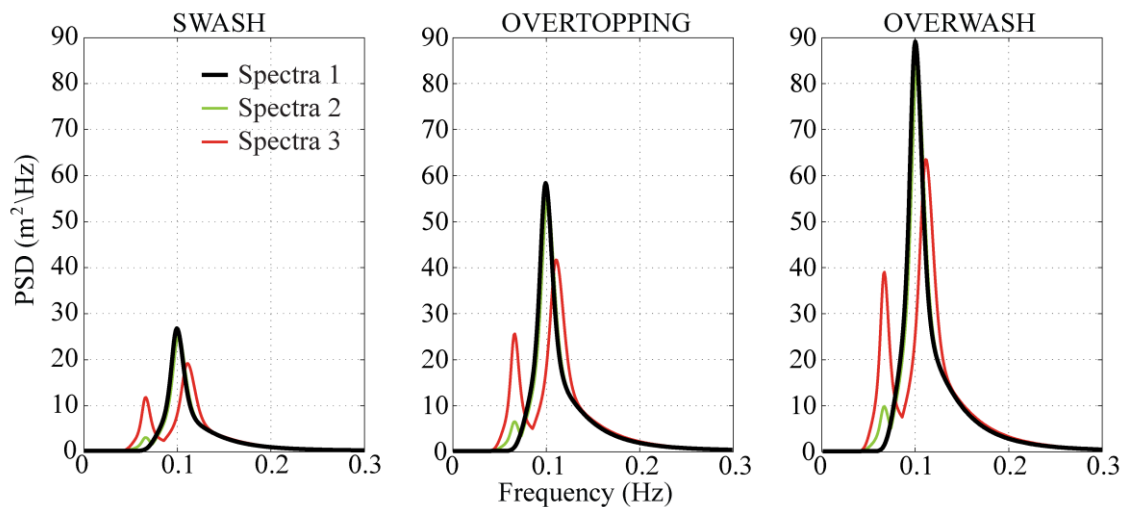


**Figure 4.15** Shape of the three different wave spectra tested for each regime; these wave spectra are representative of the simulations performed with the  $T_p = 10$ s.

Care was taken to ensure that the addition of the long period swell peak was balanced by a reduction in the wave height and period of the short period wind peak to ensure that the significant wave height and the mean wave period remained the same. The groundwater module for these additional 90 simulations was turned on or off.

Each simulation was run for 5400 s (1h 30m), with the first 30 minutes to spinoff the model (these data were removed from the analysis), and for each simulation the average discharge was computed at the crest of the barrier.

The average overwash discharge for the three different hydrodynamic regimes for variable wave periods (with and without groundwater) and spectral shapes are presented in Figure 4.16. The results show that wave period and spectral shape can produce significant modifications on the predicted average discharges, and change the boundaries of the impact regimes presented in Figure 4.12. Increasing both wave period and energy in the swell peak enhances the likelihood of overtopping and overwashing, and increases overwash discharge. Groundwater interactions only seem to have a significant effect on the swash regime, when large  $T_m$  values are tested, but under overtopping or overwash regimes the inclusion of groundwater interaction does not produce a significant difference in modelled discharge (Figure 4.12).

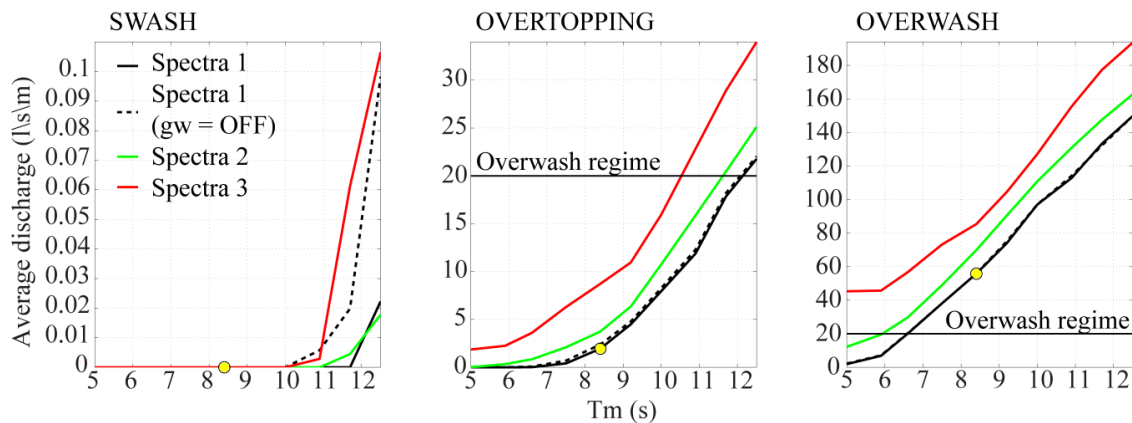


**Figure 4.16** Discharge under variable  $T_m$  values for the different regimes, testing different parameters: typical Jonswap spectra with groundwater ON (black line); with groundwater OFF (dashed grey line); and testing different wave spectral shapes (red, blue and green lines). The yellow dots represent the mid-regime simulations indicated in Figure 13.

Under overtopping and overwash regimes the water level forced in the model was significantly higher (see Figure 4.12) than the level used in the swash regime simulations. Thus, under larger

water levels the water table becomes quickly saturated, reducing the infiltration losses and enhancing the runup to go over the barrier. Under swash regime the lower water level and unsaturated beach face increase the infiltration losses and reduce the capacity of the runup to overtop the crest, while with ground-water off this effect is removed and overtopping occurs with a lower threshold.

#### **4.3.5 Morphological response under different regimes**

The analysis performed in the previous section (4.3.4) was extended to investigate the morphological response of Loe Bar under different regimes and with varying wave periods, wave spectral shapes and groundwater interactions. One hundred and twenty Xbeach-G model simulations were performed, using identical hydrodynamic forcing conditions as discussed in section 4.3.4., but this time including sediment transport and morphological updates.

Net vertical changes (difference between initial and final predicted profile) for each model simulation were computed and the results separated according to the different impact regimes (Figure 4.17).

Under the swash regime, the barrier crest is not impacted and morphological changes are restricted to the front of the barrier, characterized by erosion at the top of the beach and accumulation at the bottom (Figure 4.17).

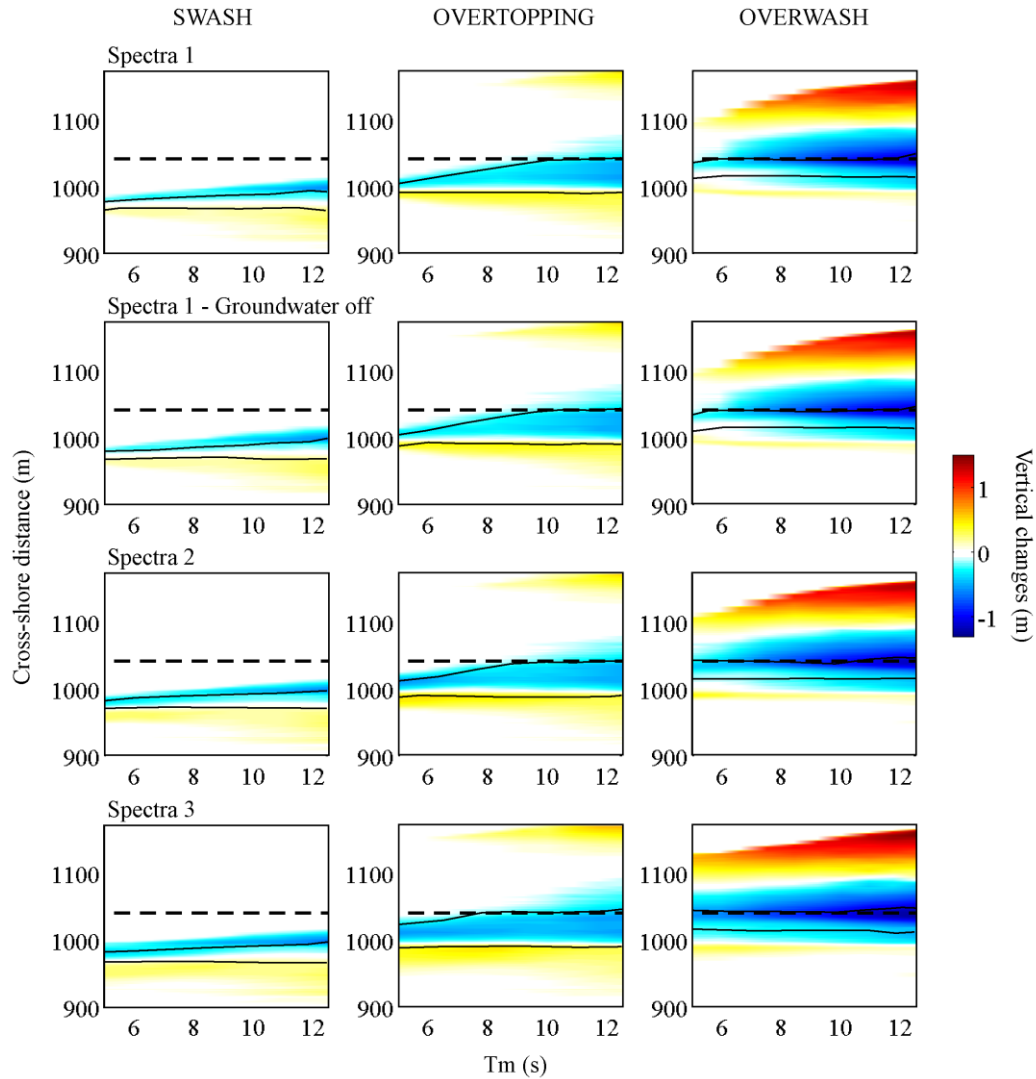


**Figure 4.17** Contour maps of the net of changes predicted for Loe Bar barrier under different impact regimes, with varying mean wave period ( $T_m$ ), spectral shapes and using groundwater off, using Xbeach-G. The dashed line represents the barrier crest and the two other black lines represent the mean water level and rundown limit.

When the barrier is subjected to overtopping conditions, the region of erosion\accumulation shifts landward, and under longer periods and/or strong wave bimodality the barrier crest is eroded with accumulation at the back of the barrier (i.e., an overwash deposit develops; Figure 4.17). This indicates that, under the overtopping regime, two morphological responses can occur, depending on wave period and spectrum shape: (1) erosion of the upper beach and accumulation on the lower



beach; and (2) erosion of the upper beach and the barrier crest and accumulation on the lower beach and the back of the barrier (Figure 4.18).

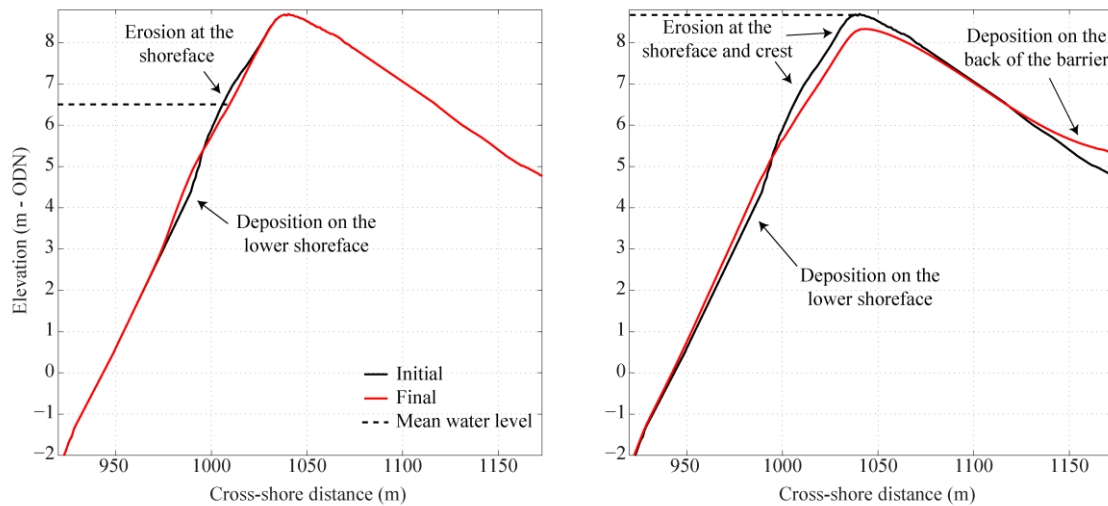


**Figure 4.18** Example of the two morphological responses of the gravel barrier under an overtopping regime.

Interestingly, in none of the overtopping cases did accretion occur on the barrier crest, considered a typical morphological response of gravel barriers to such a regime (Orford and Carter, 1982; Matias et al., 2012).

Finally, in the overwash regime, the model predicts a consistent response, characterised by erosion of the barrier crest and deposition mostly at the back of the barrier (Figure 4.17). This pattern of onshore-directed sediment transport under overwash conditions has been described in the literature as a “rollover” process, and represents an evolutionary mechanism of gravel (and sandy) barriers to attain equilibrium with the sea level and hydrodynamic conditions (Orford and Carter, 1984; Carter and Orford, 1993).

In agreement with the model simulations with morphodynamic updating turned off, the morphological response is enhanced with increasing wave period and bi-modal spectral shape, reflecting larger runup and overwash discharges.

## **4.4 Discussion**

In the first section of this Chapter, a new and unique dataset of field measurements of storm runup and overwash events on a gravel barrier (Loe Bar) is presented. This dataset was subsequently used to validate the Xbeach-G model predictions of hydrodynamics and morphodynamics. The validated model was then used to explore the hydrodynamic conditions under which this gravel barrier is exposed to different impact regimes (swash, overtopping or overwash), and the respective morphological response. This model analysis also included the investigation of the model's sensitivity to wave period, spectral shape and groundwater dynamics.

### **4.4.1 Measuring wave overtopping on a gravel barrier with a laser-scanner**

Continuous measurements of the morphological evolution and hydrodynamics were, for the first time, collected on a gravel barrier during a storm. During this experiment, 12 overwash events were recorded by a new remote sensing technique, 2D laser-scanning.

The laser-scanner measurements provided coverage of an entire cross-section of the barrier, enabling the detection of overwash flow from the top of the beach face to the back of the barrier. Due to the limited range of this laser-scanner ( $\sim 50$  m), the amount of information (e.g., backwash limit, morphological change in the lower swash zone) collected from the lower beach face was limited. Despite this limitation, the present measurements allowed a complete characterization of overtopping and overwash hydrodynamics, including vertical and horizontal runup excursions, flow velocity and overtopping depth, together with the morphological evolution of the barrier.

Due to the absence of field observations of overwash hydrodynamics on gravel beaches worldwide, the present observations may only be compared with measurements performed on sandy beaches or laboratory experiments. The average overwash velocities measured during the present field experiment (Figure 4.7) are of the same order as those measured in the field on sandy barriers (Leatherman, 1977; Leatherman and Zaremba, 1987; Holland et al., 1991; Bray and Carter, 1992; Matias et al., 2010), where mean velocities varied between 0.5 and 3 m/s, and in laboratory tests using sandy (Srinivas et al., 1992; or Donnelly, 2008) and gravelly sediments (Matias et al., 2014), where average overtopping and overwash velocities ranged from 0.8 and 3.6 m/s. Despite these results, in the present

In regard to overwash depths, past field observations performed on sandy barriers yielded peak flow depths ranging from 0.10 m to 0.7 m (Fisher and Stauble, 1977; Matias et al., 2010; or Bray and Carter 1992), leaving the present observations within the lower range of values (maximum depths of approximately 0.20 m – Figure 4.7).

These comparisons provide confidence that this remote sensing technique is suitable for measuring these processes on gravel barriers under challenging field conditions.

The present observations of the morphological response of the gravel barrier during this storm event showed that major adjustments of the beach face occurred; however, no changes were noticed on the crest or at the back of the barrier (Figure 4.5). Typical gravel barrier morphological responses under overwash conditions include the build-up of the barrier crest under short overwash intrusion (Orford and Carter, 1982), or crest erosion and deposition on the back of the barrier (Matias et al., 2012). Despite the lack of detail on the fundamental mechanisms that are underlying these morphological responses, Matias et al. (2012) demonstrated in a laboratory experiment that the antecedent morphological state of the barrier is a key aspect in determining its morphological

response to storm conditions. Therefore, under equilibrium conditions between the barrier morphology and overwash hydrodynamics, modifications to the crest and back of the barrier can be very small.

Taking into consideration that the present storm has a return period of 1 year (from the 4 years of wave observations) is expected that the present morphological state of Loe Bar is in equilibrium with these conditions, and therefore limited morphological changes on the barrier were observed.

#### **4.4.2 The use of Xbeach-G to predict overtopping and overwash on a gravel barrier**

Comparison between the Xbeach-G predictions and the field observations presented in this Chapter show that Xbeach-G has very good skill in accurately predicting the hydrodynamics and morphological response of this gravel barrier under storm conditions. Despite the limited number of overwash events observed during this storm, the model was capable of reproducing them (with some level of under-prediction), indicating that it has the ability to predict the occurrence of overwash under threshold conditions.

Using the most complete model setup (Setup 2 – with bed update and groundwater on), the model was able to predict extreme runup ( $R_{2\%}$ ) with only a 5 % underestimation of the observations (Table 4. 2). Modelled averages and maximum overtopping discharge at the crest were also very close to what was measured in the field (Table 4.2). Such accurate results are in line with recent validation efforts performed with Xbeach-G hydrodynamics, indicating that the model is capable of reproducing wave transformation, runup and overtopping with an average error < 10% (McCall et al., 2012; McCall et al., 2014).

The morphodynamic Xbeach-G model (McCall et al., 2015) was validated in the present Chapter by simulating the morphological response of Loe Bar under the measured storm conditions. Comparison between the model predictions and laser-scanner measurements show that the model accurately predicts net changes (comparing only the measured and predicted final profile), and also the morphological evolution during the storm with varying tide levels (Figure 4.11). These results are in agreement with a recent validation of the Xbeach-G morphodynamic module (McCall et al., 2015), in which the model accurately reproduced the morphodynamic response of several gravel barriers in both qualitative and quantitative terms.

According to McCall et al. (2015), the skill of Xbeach-G in predicting the morphological response is greatest under energetic storms (e.g., barrier rollover) and that the model underestimates berm development under less energetic conditions. The limited ability of Xbeach-G to construct a berm is also apparent in the overtopping simulations, since no deposition at the crest was verified (Figure 4.17).

Overtopping may be considered a process in which swash excursions simply carry over the crest, causing vertical accretion at the top of the crest due to the rapid crestal percolation (Orford and Carter, 1982). Present model simulations show that under overtopping regime the effect of groundwater on overwash discharge (Figure 4.16) and morphological response (Figure 4.17) is relatively small. This indicates that infiltration processes are not preponderant on the dissipation of the overwash flow and therefore sediment tends to be transported to the back of the barrier.

To test the capability of XBeach-G in producing typical overtopping responses, such as crest-build up or berm development, a new group of simulations were performed, using the forcing conditions used to produce the overtopping regime on Figure 4.17 (unimodal spectrum shape and groundwater on). Four models were run using different sediment sizes ( $D_{50} = 2, 5, 20$  and  $30$  mm) and, inside

each of those models, ten different wave periods were tested (as in Figure 4.17). The results show that by increasing significantly the sediment size the model starts to predict berm development and accumulation at the top of the barrier crest (Figure 4.19).

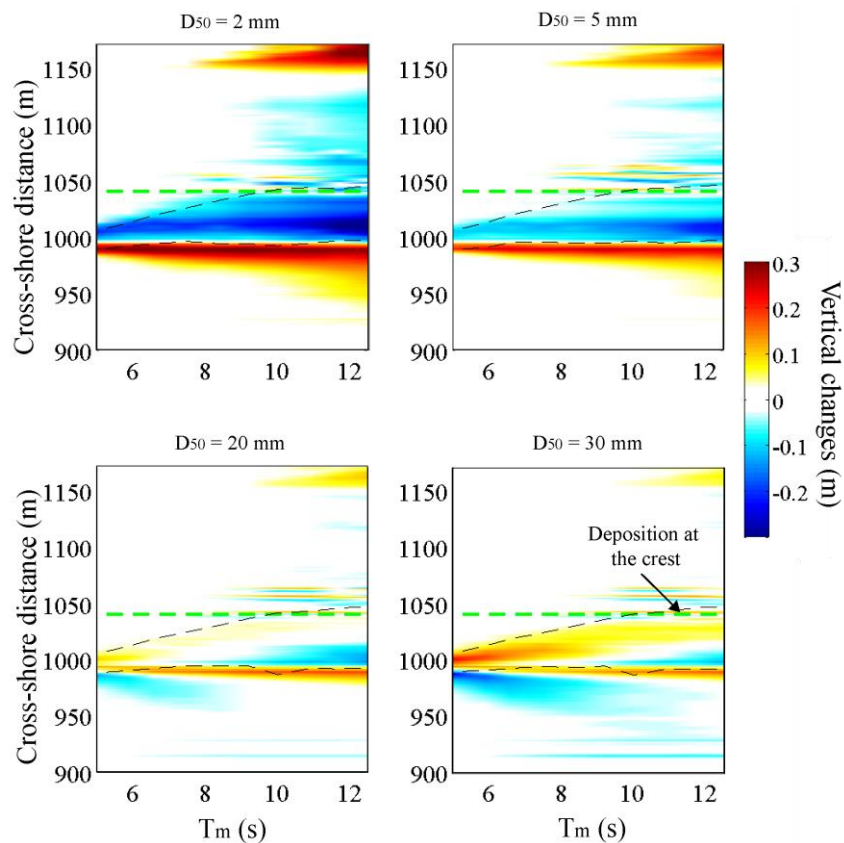


**Figure 4.19** Morphological response of Loe Bar under overtopping impact regime for different wave periods and using different sediment sizes. Green dashed line represents the barrier crest while the two black dashed lines indicate the lower and mid limit of the water level.

With larger sediments, the larger hydraulic conductivity increases water infiltration on the bed, reducing the power of the runup flow to transport sediments to the back of the barrier. Therefore, these sediments accumulate faster on the top of the barrier crest or beach face (Figure 4.19). With finer sediments, like those at Loe Bar, and according to the present model results, it seems unlikely

that such processes would occur and therefore the morphological response under this impact regime is different (Figure 4.17).

#### **4.4.3 Defining storm impact regimes on Loe Bar**

In the third section of this Chapter the conditions characterizing the three different impact regimes (swash, overtopping and overwashing) were investigated for Loe Bar barrier using Xbeach-G. The initial approach was to quantify the overtopping and overwashing discharge under different combinations of water level and wave height for a certain wave period (Figure 4.12). With this ‘map’ it was then possible to define the three boundaries, based on discharge, that separate the three different impact regimes. These boundaries were defined using existing engineering guidelines that relate average overwash discharge at the crest of defence structures (e.g., dykes) with morphological responses. The present model results allowed the validity of this method to be tested for gravel barriers, since a very strong relationship was verified between average overwash discharges at the crest ( $q_c$ ) and morphological response on the crest and back of the barrier (Figure 4.20).

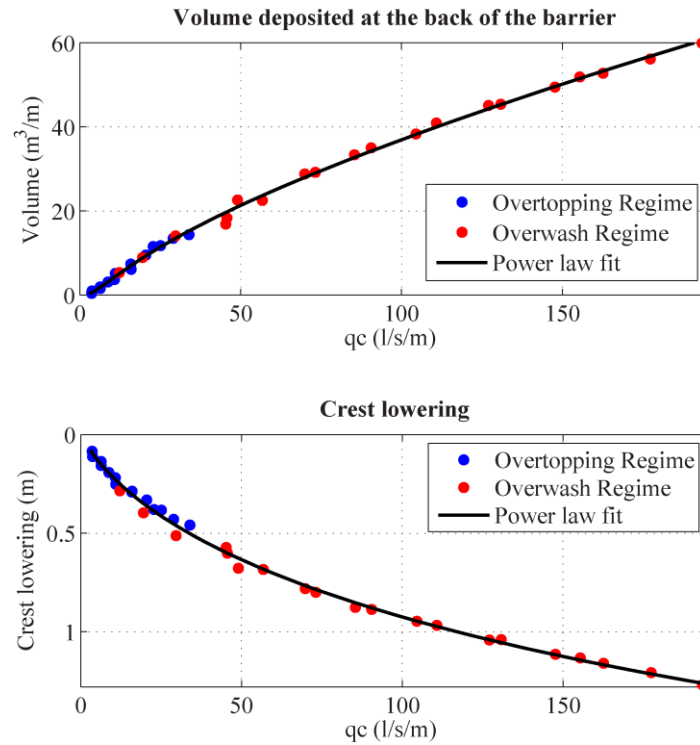


**Figure 4.20** Volume deposited at the back of the barrier as a function of average overwash discharge at the crest (top panel). The power fitting adjustment to data is represented with a black line. Crest lowering as a function of average overwash discharge at the crest (bottom panel).

The resulting impact regime diagram was then compared with the joint distribution of wave height and tide level for the Loe Bar location. This comparison indicated that, according to the Xbeach-G model, overtopping/overwashing conditions on Loe Bar are extremely unlikely because this requires unrealistically high water levels (Figure 4.12). Further analysis of this result revealed that this apparent low vulnerability is due to the limited representativeness of the regime diagram in terms of the effects of different wave periods and the wave spectral shapes.

Each impact regime can operate quite differently under different wave periods and spectral shapes, as the present model exploration demonstrates very clearly (Figure 4.16). Two new sets of XBeach-G models were performed in order to reproduce the boundaries of the overwash regime under a large wave period ( $T_m = 12.5$  s) and using unimodal and bimodal spectrum shapes. The results of



these new simulations were overlapped on the results for the overwash regime boundary computed in Figure 4.12, and demonstrate how dramatically the definition of this impact regime can change when these parameters are modified (Figure 4.21).

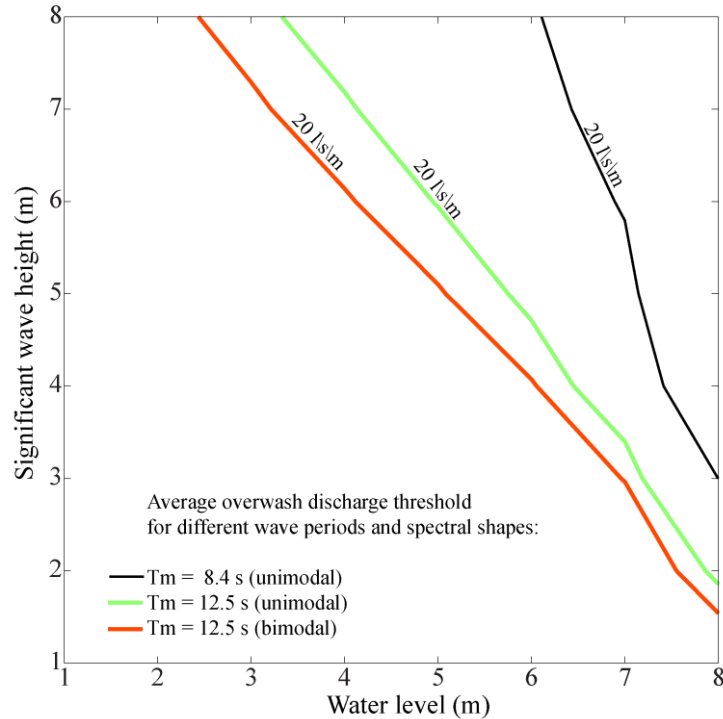


**Figure 4.21** Map showing the average overwash discharge threshold ( $20 \text{ l/s/m}$ ) predicted using different wave period ( $T_m$ ) and wave spectrum shape.

From all these parameters, the one which seems to most magnify the discharge predictions is wave spectrum bimodality. This particular aspect has been previously identified along the south coast of England as an important factor linked to coastal flooding hazards (Hawkes et al., 1998); nevertheless, very little is known about the underlying processes responsible for such markedly different results when compared to a unimodal spectrum (Masselink et al., 2014). In the present Chapter, this particular aspect is explored by the validated Xbeach-G model (Figure 4.9). The main difference between the unimodal and bimodal spectrum across the nearshore is shown to be the differential mechanism of wave dissipation that both spectra present (Figure 4.10). While in a

bimodal spectrum the short period peak (the peak period) tends to dissipate the energy before arriving to the swash (due to breaking), the long period peak gains due to shoaling processes (Mendez Lorenzo, et al., 2000). The result of this differential dissipation of the two peaks of the spectrum causes the long-period peak to become dominant in the swash zone, increasing the vertical runup excursions and swash width (Figure 4.10).

These results also highlight the importance of a complete characterization of the wave spectrum in order to properly characterize water motions in the swash zone; this aspect may be crucial in areas where wave spectrum bimodality is present (Polidoro et al., 2013).

The effect of wave period and spectrum shape was also investigated using the morphodynamic predictions and showed similar impacts to what was observed in hydrodynamic predictions (Figure 4.13). Under larger wave periods, erosion at the shoreface or barrier crest increases and this is magnified with the increase in wave spectrum bimodality. Larger runup excursions induced by the bimodal wave spectrum are expected to induce more overtopping discharge or to increase the backwash activity, and thereby initiate sediment transport.

## **4.5 Conclusion**

This chapter presented unique field observations of overtopping and overwash events during a storm on a gravel barrier. These measurements were performed with a 2D Laser-scanner and allowed a complete characterization of the hydrodynamics and morphological response along a cross-section of the barrier. These measurements allowed a validation of Xbeach-G for this gravel barrier, providing a very high level of confidence for subsequent analysis performed with the model.

The boundaries between the different impact regimes (swash, overtopping and overwash) were explored for a fine gravel beach, Loe Bar, using Xbeach-G. Hundreds of model simulations demonstrated that these boundaries are not only the result of the combination between water level and wave height, but that wave period and spectral shape also play key roles. Wave bimodality encourages the development of higher wave runup and wider swash zones dominated by long-period water motions, enhance the likelihood of overtopping and overwash, and increase the associated discharge. Morphological responses under the different impact regimes are also heavily controlled by these parameters.

## 5. Discussion and Conclusions

This chapter will provide a summary of the discussions explored in the separate chapters and brings together the different components which have structured the thesis with summary results. Section 5.1, 5.2 and 5.3 will discuss the advantages and disadvantages of the 2D laser-scanner, the contribution of the present findings to the state of the art knowledge of swash zone of coarse-grained beaches under positive (section 5.2), and zero and negative freeboard regimes (section 5.3). This is followed by the overall conclusions of the thesis.

### 5.1. Development of a 2D laser-scanner to measure swash zone during storms

The versatility and precision of 2D laser-scanners has enabled the development of a large range of non-contact measurement applications, ranging from forestry (Miettinen *et al.*, 2007) to robotics (Teixidò, *et al.*, 2012). Applications of this technology to the nearshore zone are recent and by the beginning of the present research project only a few short publications reported the attempt to acquire field and laboratory measurements of swash zone hydro- and morphodynamics (Brodie *et al.*, 2012, and Blenkinsopp *et al.*, 2010 and 2012). Recently, and during the present research project, the number of applications of this instrument to measure swash hydrodynamics has increased, particularly in laboratory applications, such as the combined use of laser-scanners with video cameras to measure swash hydro- and morphodynamics (Vousdoukas, *et al.*, 2014) or the single use of a laser-scanner to measure

the wave propagation along a wave flume (Streicher et al., 2013). Notwithstanding these recent developments, the acquisition of field data on coarse-grained beaches during storms was never performed before, and the present research project reports the first time that this instrument was used in the field during such a range of storm conditions.

In the present research project, a 2D laser-scanner (Sick LD-LRS3100) was deployed during seven field experiments on six different coarse grained beaches during a variety of storm conditions to record swash zone hydro- and morphodynamics (Figure 5.1). This instrument allowed the acquisition of high-frequency hydro- and morphodynamics of the entire swash zone at each of the study sites, covering the full range of storm impact regimes that this project aimed to collect data for (positive, zero and negative freeboard; refer to Section 1.2 for definition of storm impact regimes). Such type of deployment has not been performed previously in the field; thus, the present research project provides new insights into the skills and limitations of this technique, in comparison to the existing methods, as well as providing novel insights into the measured conditions.

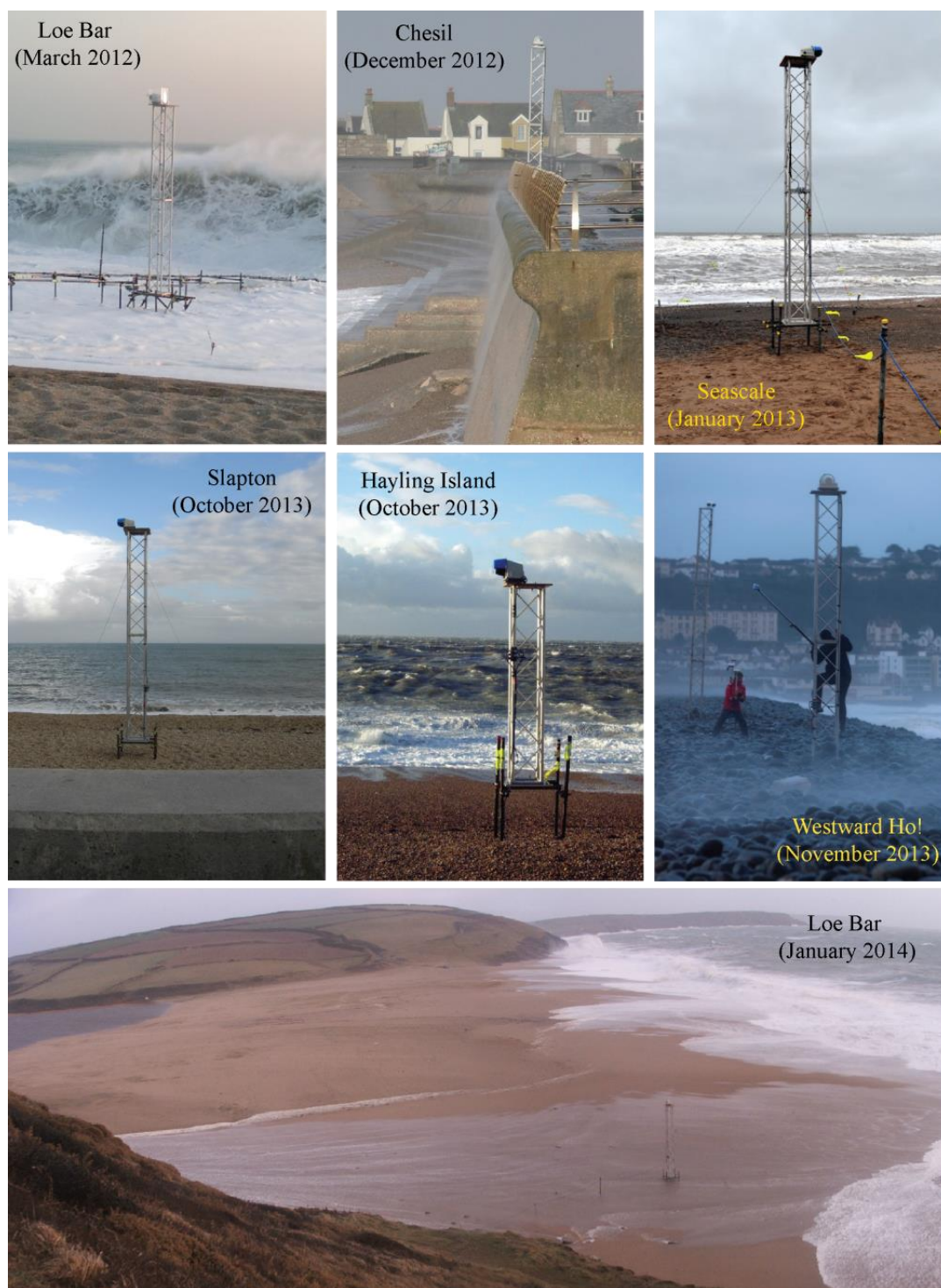


**Figure 5.1** Field photos from each field deployment performed with the laser-scanner, showing the large variety of environments and setup types (e.g., mounted on the beach or at the top of a seawall).

### **5.1.1 Advantages and limitations**

Considering the state-of-the-art field methods and the objectives of the present research project (measure high frequency swash morphological response and hydrodynamics on coarse-grained beaches during storms; refer to Section 1.3), most of the conventional methodological options (e.g. RTK-GPS, pressure transducers, video cameras, etc.) would not be appropriate for the present research project requirements. The laser-scanner provides clear advantages compared to the existing methods:

- The capability to collect simultaneous measurements of the morphological evolution and hydrodynamics (track the water surface) using a single instrument.
- High spatial resolution (depending on the elevation of the tower and shape of the profile – but typically ranging from few cm to a few meters maximum) and high frequency of acquisition (depending on the sample rate, but up to 5 Hz).
- Data collection can proceed under reduced light (e.g., at night) and during rainy conditions, which are typical meteorological conditions during storms.

There are also some limitations associated with using a laser scanner:

- Limited spatial range of this instrument (~ 50 m).
- Data are collected along a single profile of scan (2D) and alongshore variability in the hydro- and morphodynamics are not captured.

The fact that this instrument can perform measurements during day and night and under rainy conditions represents a significant advantage over traditional remote sensing methods, such

as video cameras, as under storm conditions environmental parameters such as light level and precipitation, can become limiting factors. The only other type of instrument capable of collect simultaneous beach morphology and water surface are ultrasonic bed level sensors (Tuner et al., 2008) which have been successfully used under stormy conditions on a fine gravel beach (Poate et al., 2013). Although Poate et al. (2013) obtained good results with a bed-level sensor array deployed on a gravel beach, it was shown in Chapter 2 that a single laser-scanner provides superior coverage and spatial resolution (see also Almeida et al., 2013). In addition, the effort involved with deployment of bed level sensors array is very considerable (e.g., requires an extensive scaffold frame with numerous vertical uprights and horizontal connecting scaffolds). Moreover, bed-level sensors have a very short range ( $\sim 1.5$  m) and this inhibits their use during storm conditions when rapid and extensive bed-level changes may occur.

The spatial resolution of the laser-scanner is an important advantageous aspect, because it enables capturing small morphological features that typically have short relaxation times. An example of the importance of such resolution was demonstrated in Chapter 2, which presented observation of highly detailed morphodynamic evolution of the step deposit during a tide cycle (Almeida et al., 2015). Similar swash morphodynamics measurements have been made previously on gravel beaches (Masselink et al., 2010); however, the present data represents significantly more energetic conditions.

All field deployments performed with the laser-scanner during the present research project allowed measurement of the swash zone with an average horizontal resolution of about 7 cm and a minimum distance between adjacent sample points of around 1.5 m (Figure 5.2). During most deployments, the entire swash zone was fully covered by the laser-scanner



measurements, enabling the tracking of the full extension of the runup and rundown excursions during high tide stages (Figure 5.2). The only exception was the last field deployment performed at Loe Bar (Chapter 4) where the lower swash zone was not covered by the laser measurements, but where the set-up was designed to capture overwash processes (Figure 5.2).

During mid and low tide stages, and at the most dissipative sites (e.g., Seascale and Westward Ho!), the swash zone shifted significantly offshore ( $> 200$  m) precluding any laser-scanner measurement. This aspect reveals one of the most important limitations of the present instrument which is the range. The present laser-scanner sensor has a range of approximately 50 m, which for macro-tidal environments with intertidal areas of about 300 m wide only represents 1/6 of the total area of interest. To cover such a large distance with an appropriate horizontal resolution it would need a much more powerful laser-scanner and a laser-scanner with an extended range would significantly enhance the capability of this technique. However, a larger scan range also requires a higher mounting elevation, because due to the low angles of incidence at larger scan distance the specular reflection of the laser beams will potentially increase and the signal quality will reduce (Almeida et al., 2015).

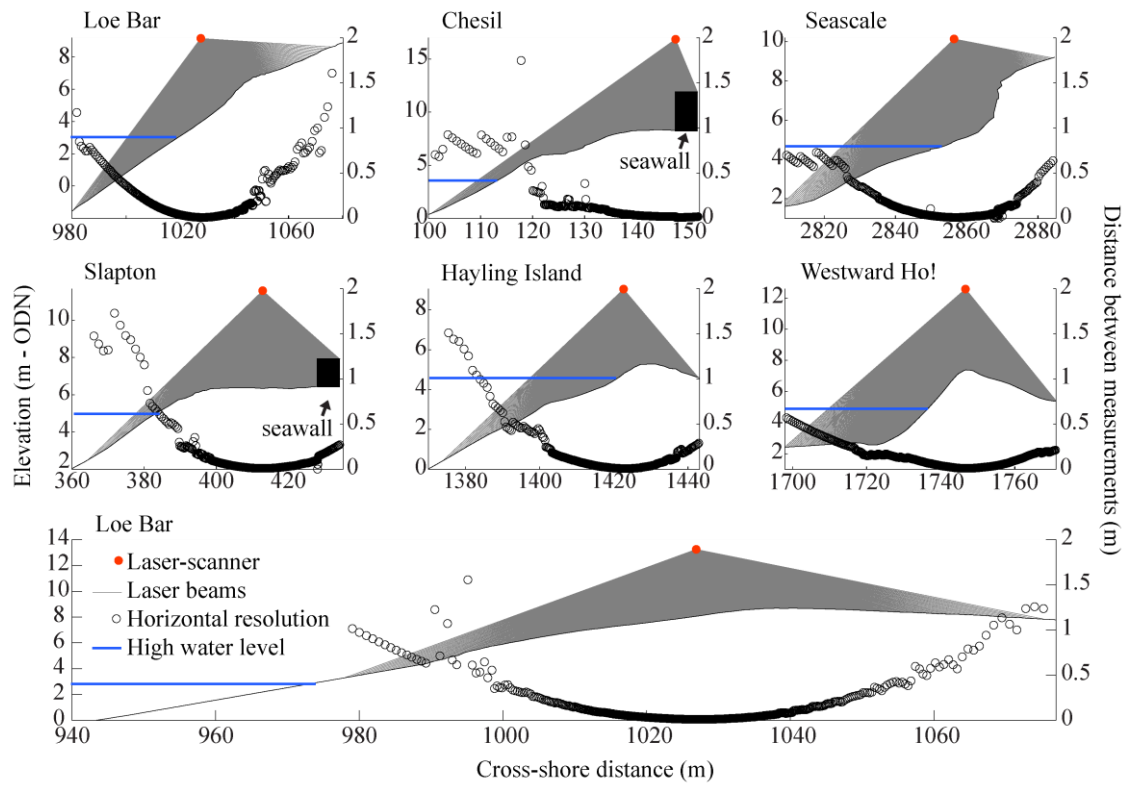


**Figure 5.2** Theoretical laser-beam trajectories during a scanner rotation (gray lines) and horizontal distance between measurements (black dots) performed by the laser-scanner at each of the study sites.

Another important limitation of this instrument is the spatial coverage, since it only has a single rotation mirror that can only scan a single profile along a specified sector. Other laser-scanners, such as the 3D terrestrial laser-scanners have a second rotational axis; however, the rotation frequency on this second axis is generally too low to scan a quasi-instantaneous water surface in two spatial dimensions. A combination of several scanning lines might event make this possible (e.g., Wübbold et al., 2012) although the spatial resolution would be proportional to the number of devices, meaning an extremely high number of installations for high resolution coverage.

### **5.1.2 Future developments and applications**

Taking into consideration the present limitations, it is possible to formulate suggestions for future improvements to the present technique:

- Development or test existing laser-scanners with higher range in order to cover the entire swash zone on macro-tidal environments under all tide stages;
- Development of a laser-scanners with two rotating axis that allow a complete 3D coverage and resolve the full spectrum of waves propagating into the surf and swash zone; some sort of combination between the present 2D laser-scanner and fast rotating radar would potentially achieve this.

Despite the present limitations, the advantages of this method are notable and during the present research project several other surveys were performed that demonstrate the versatility and potential of this instrument. An example of such additional deployment is shown in Figure 5.3, which shows the deployment of the laser-scanner in front of seawall of a gravel beach (Chesil) during an extreme storm.



**Figure 5.3** Sequence of photos showing the deployment of the laser-scanner on top of the seawall at Chesil on the 05/02/14 during an extreme storm.

Figure 5.4 shows the continuous time series of the morphological response of the upper beach at Chesil over 3 tidal cycles during the storm obtained with the laser scanner. Lowering of the upper beach in front of the seawall by up to 4–5 m occurred mainly during the falling tide at the peak of the storm with significant wave height  $H_s$  of up to 7.5 m. Beach recovery started immediately after the peak of the storm during the second rising tide with significant wave heights still exceeding 4 m. Beach recovery continued throughout the third tide and by the end of the third tide more than 2 m of accretion had occurred; in other words, the lower part of the high tide swash zone had recovered by 50% within 24–36 hours. This highlights the rapidity of the recovery process and the importance of the laser-scanner in recording such important processes under extreme conditions where no other equipment is able to collect this type of information.

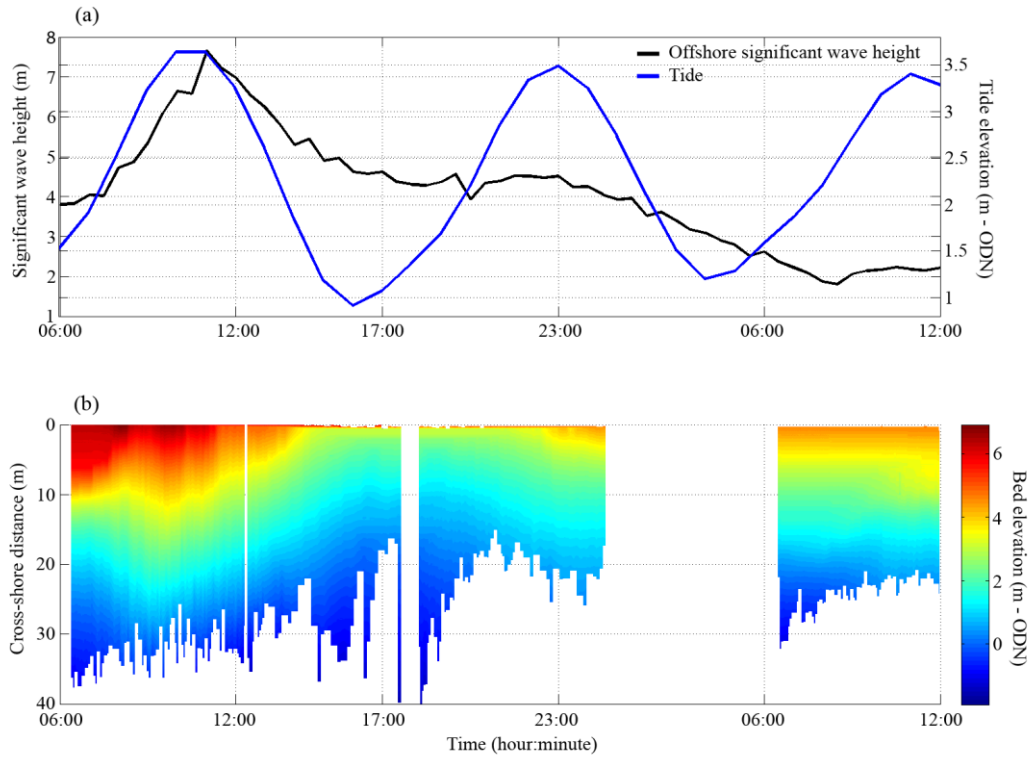


**Figure 5.4** Time series of: (a) significant wave height  $H_s$  and tide level; (b) bed elevation at Chesil in south Dorset during an extreme storm.

The simplicity and capability of the 2D laser-scanner allows this instrument to be adapted to a huge variety of coastal applications, ranging from the collection of measurements on natural beaches to coastal engineering structures. Therefore it is expected that the interest in, and application of, this instrument in the future will rise significantly, and is very likely to become a reference tool to measure nearshore zone.

## **5.2 Morphodynamics of coarse-grained beaches during storms (positive freeboard)**

The only existing classification scheme that attempts to describe the morphodynamic behaviour of distinct coarse grained beaches during mild and storm conditions under positive freeboard hydrodynamics is that developed by Jennings and Shulmeister (2002). Based on 42 beaches around New Zealand, Jennings and Shulmeister (2002) proposed a division of the different coarse-grained beaches in three main groups: pure gravel (PG), mixed sand and gravel (MSG) and composite sand and gravel (CSG) beaches. This division was achieved by means of discriminant analysis and took into consideration several morphological and sedimentological aspects (e.g., average sediment size, beach width, number of berms, or the storm berm height), together with a morphodynamic index (Iribarren number - Battjes, 1974) as a differentiator of the dominant morphodynamic regimes identified in each of the sites.

Jennings and Shulmeister (2002) classification was developed using beaches with tidal ranges varying between micro- (38 of the sites) and meso-tidal (4 of the sites) regimes, whereas in the present research project study sites, and in most of the coarse-grained beaches in UK, the tidal regimes varied from meso-tidal to macro-tidal. This aspect led to some difficulties during the present research project to link the Jennings and Shulmeister (2002) conceptual model to the present field sites. For example, according to Jennings and Shulmeister (2002) it would be expected that Seascale (MSG) would display a morphodynamic behaviour more similar to that of the PG beaches (e.g., Chesil or Loe Bar) than CSG beaches such as Westward Ho!. Present results show, however, that Seascale and PG beaches have a significantly distinct morphodynamic response, mainly due to the fact that at Seascale a very

wide intertidal terrace dissipates most of the incoming waves, while on PG beaches a very narrow surf zone develops just at the seaward boundary of the swash. These findings demonstrate that for the development of a complete conceptual morphodynamic model for coarse-grained beaches under storms is fundamental to include all tidal range beaches and take into consideration their different surf zone dynamics.

These aspects, together with some new insights into the fundamental processes underlying the swash zone morphodynamics during storms found during this research project (e.g., Almeida et al., 2014 and 2015) represent a significant contribution to the work developed by Jennings and Shulmeister (2002) and to the state-of-the-art conceptual understanding of the response of coarse-grained beaches during storms under positive freeboard regimes.

Figure 5.5 presents a diagram that summarizes the present findings in relation to the link between the contrasting surf zone dynamics and the morphodynamics of the different coarse-grained swash zones during storms. On the top panel of this diagram is illustrated the relationship between the surf scaling parameter and the extreme vertical runup (obtained in Chapter 3) which represents a categorization of the swash hydrodynamics according with their morphodynamic regime. On the basis of this relationship are the different profile shapes found under different tidal regimes, and their contrasting capability to dissipate the incoming wave energy before reaching the swash zone (Almeida et al., 2014).

The left side of this diagram is representative of the reflective beaches, such as the energetic PG beaches, typically with very steep beach faces, a very well defined beach step and no development of an offshore bar during storms (Jennings and Shulmeister, 2002). They develop very narrow surf zones near the swash zone (Buscombe and Masselink 2006),

controlled by the beach step, with very energetic plunging breaker dominating the entire tide cycle (Kemp, 1961).

Present field observations provided new insights into the morphodynamics of the swash zone of PG beaches during storms (under positive freeboard hydrodynamics) which are strongly linked to the dynamics of the beach step (Almeida et al., 2015).



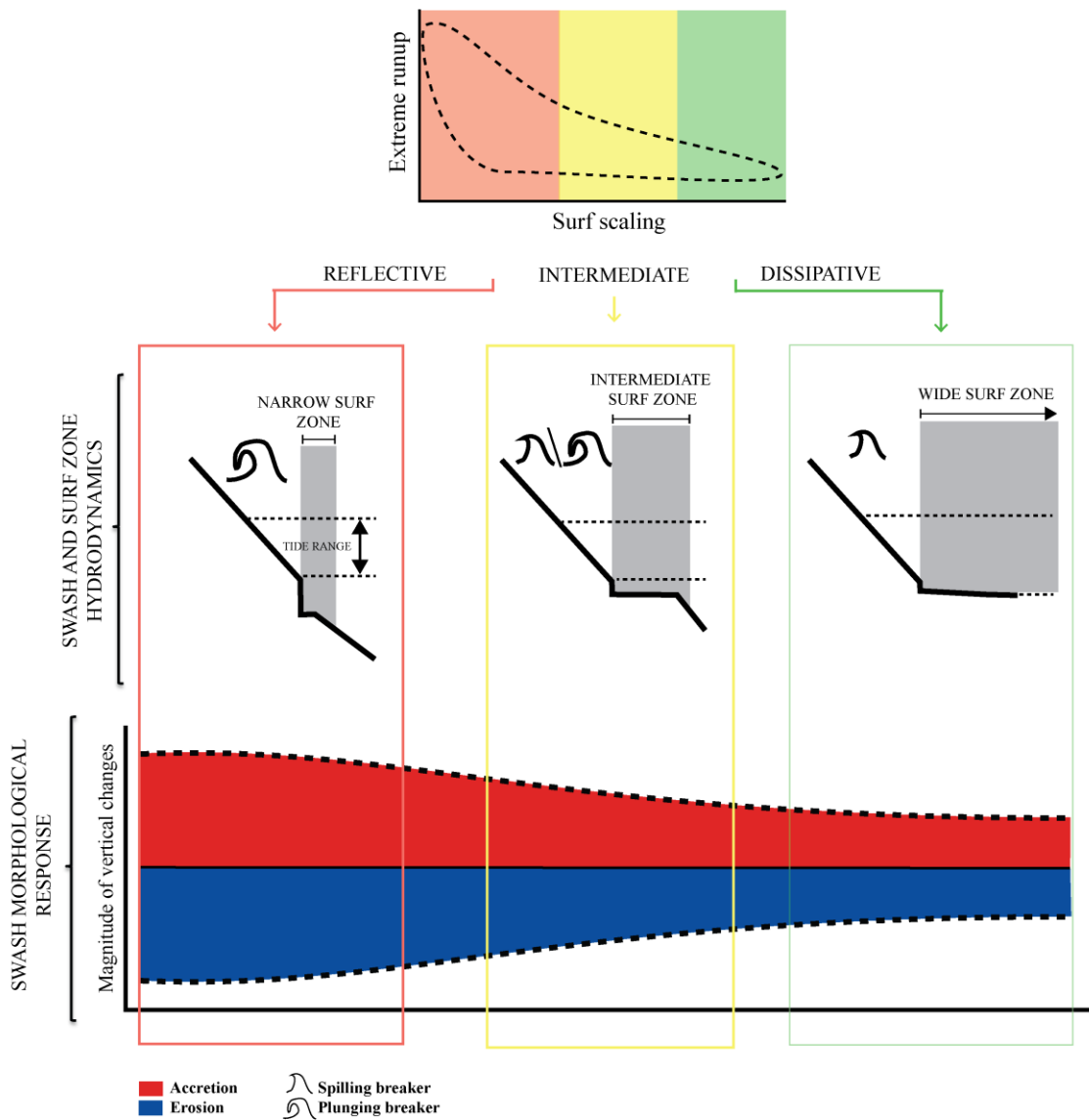


**Figure 5.5** Conceptual diagram for coarse-grained beaches hydrodynamics and morphodynamics during storms; on the basis of this diagram is the relationship between surf scaling parameter and extreme vertical runup (top panel – the dashed area represents the relative range of vertical runup excursions under different regimes), which express the amount of wave dissipation that occurs on the different types of surf zones (middle panel) and can be linked to the swash potential morphological response (bottom panel – top and bottom dashed lines represent the respective maximum and minimum vertical change observed in the field on each type of beach).

Due to the absence of an offshore bar, the beach step becomes the key morphological feature where offshore incident waves dissipate all their energy before entering the swash zone

(Ivamy and Kench, 2006). Present field observations revealed that the tide induced variable wave breaking location is linked to the cross-shore translation of the beach step, and associated to the accumulation and erosion phases on the swash zone during the tide cycle (Almeida et al., 2015).

Underlying this tidal asymmetrical morphological response is the link between the wave breaking sediment remobilization and the distance between the break point to the uprush (Masselink et al., 2010). When waves break directly on the beach face (during rising tide – Figure 5.6) the amount of sediment added to uprush is higher than the amount that is eroded during the following downrush. On this scenario accretionary processes are dominant (e.g., development of step deposit), while on the falling tide the offshore migration of the breaking point increases the distance between the breaking point and the uprush, favouring the erosion processes during backwash (Figure 5.6).

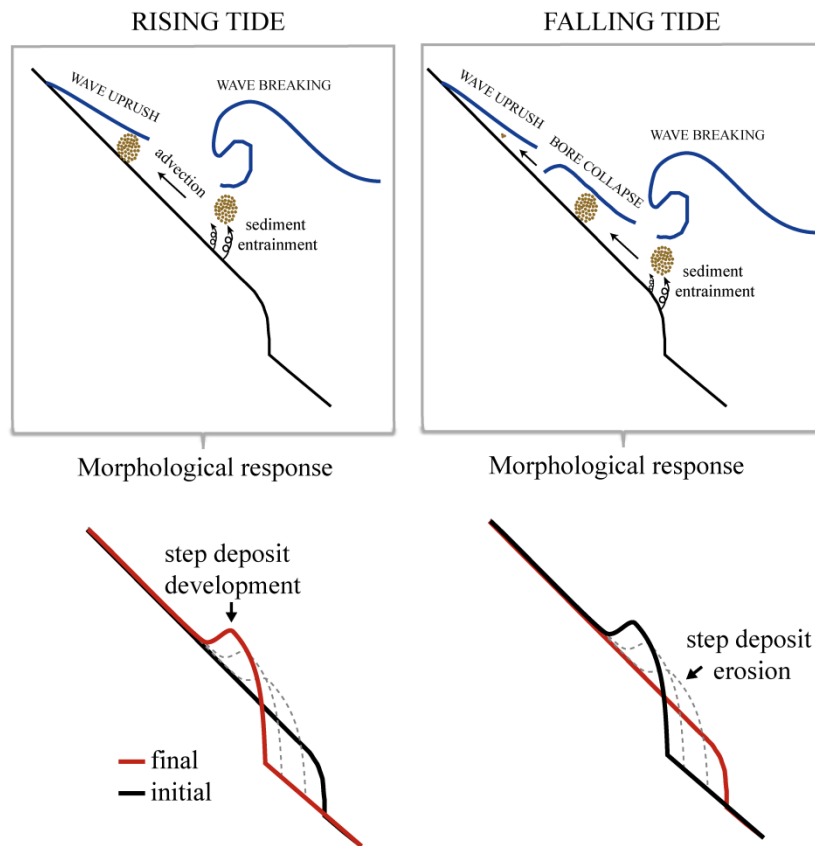


**Figure 5.6** Illustration of the link between breaking location and sediment transport during the rising and falling tide, and consequent morphological response. On the rising tide (left panels) the breaking point moves onshore and waves break more often landward from the beach step and the sediment transport favours uprush and step deposit development. On the falling tide (right panels) the breaking point moves offshore reducing the uprush sediment transport and enhancing backwash and erosion of the step deposit.

Similar morphodynamic processes were identified by Kulkarni et al. (2004) on a MSG beach under mild wave conditions, however present field observations were the first to document this morphodynamics process under energetic wave conditions and on different PG beaches (e.g., Chesil and Loe Bar).

These new findings build on the existing understanding of the morphodynamics of PG beaches during storms (e.g., Jennings and Schulmeister, 2002), although they might not

represent the only response that these type of beaches can present during storms. It's expected that under strong longshore swash hydrodynamics (e.g., oblique wave attack) the morphological response might be significantly different (e.g., Ruiz de Alegria-Arzaburu and Masselink, 2010).

On the central section of the diagram (Figure 5.5) are the beaches characterized by intermediate morphodynamic regimes, which in the present study were characterized by the presence of a narrow intertidal terrace and a very gentle beach step on the lower beach face (e.g., Hayling Island), however resembled in response and shape by the MSG beaches of the East coast of UK (Pontee, et al., 2004). Key differences between these sites and PG reflective beaches are the partial dissipation of the incident waves on the intertidal terrace and the apparent reduced influence of the beach step on the swash zone dynamics during the tidal cycle (Almeida et al., 2014).

Moderate wave dissipation is verified on this type of surf zone during all tidal stages but with more expression during low tide, when waves break on the full length of the terrace (Miles and Russell et al., 2006). Under such conditions the amount of wave energy that reaches the swash zone is relatively smaller than what is verified on PG beaches, resulting in lower levels of extreme runup. Present findings indicate that the lack of energetic waves at the boundary of the swash zone to “inject” sediment into the uprush (Figure 5.6 – rising tide) limits the amount of onshore sediment transport and favours backwash. This is assumed to be one of the reasons why during storms these beaches typically present a negative net sediment transport (Almeida et al., 2014, Pontee et al., 2004), although strong longshore swash motions can potentially produce distinct morphological response.

Finally on the right side of the diagram (Figure 5.5) are presented the sites dominated by dissipative regimes, typical macrotidal beaches characterized by having very large and flat intertidal terraces (e.g., Seascale and Westward Ho!) and very dissipative surf zones during storms (Chapter 3). Due to the very large amount of wave dissipation in the surf zone, limited amount of wave energy reaches the swash zone of these sites, and typically it reaches the swash zone in the form of spilling breakers (Chapter 3). Such type of boundary conditions plays an important role on swash zone hydro- and morphodynamics of these sites (Almeida et al., 2014). Due to the reduced amount of wave energy, a limited range of runup excursions occur and consequently small morphological changes are found (Figure 5.5). As it was verified on intermediate sites, the lack of mechanisms to promote onshore sediment transport favours backwash sediment transport and therefore erosion might be the result of the net of morphological changes observed during a storm (e.g., Westward Ho! results – Chapter 3).

This particular type of beach (dissipative) was not included in Jennings and Schulmeister (2002) conceptual model, and therefore CSG beaches such as Westward Ho! and MSG beaches like Seascale are expected to present significantly different morphodynamics behaviour to CSG and MSG beaches under microtidal environments.

These new insights bring a new perspective to the response of coarse-grained beaches during storms under positive freeboard hydrodynamics. In order to achieve a universal behavioural model for coarse-grained beaches the present Jennings and Schulmeister, (2002) conceptual model needs to include all tidal regimes environments, which represent a large amount of UK coarse-grained beaches (Scott et al., 2011).

The present research project provide clear evidence that in order to understand the net morphological changes over a tide cycle it is fundamental to acquire high frequency morphological data. This type of information is crucial to improve our understanding of the short term processes which with traditional pre- and post-storm surveys would be missed (e.g., Single, 1992). The present research project represents an attempt to characterize the relationship between the swash zone hydrodynamics and the related morphological response under storms; however the presented analysis and assumptions are limited to the present measurements. Further and similar datasets are important to solidify the present assumptions and to improve the understanding of processes that were not covered in the present project such as the influence of the long shore motions and the preceding morphological state of the beach on the morphodynamic response of the beach during a storm.

### **5.3 Storm impact regimes on gravel barriers**

The final section of this research project was dedicated to the investigation of gravel barrier response to extreme storms under conditions of zero and negative freeboard. A combination of unique field measurements and numerical modelling (XBeach-G) was used to investigate under which conditions a gravel barrier is exposed to different impact regimes, such as swash, overtopping or overwash (Sallenger, 2000). The definition of the boundaries of these different impact regimes is important for assessing the vulnerability of these environments to present and future scenarios of storminess and sea-level rise. This aspect is particularly relevant for the ARCoES project since such types of analysis can provide practical evidence

of the level of vulnerability of the nuclear power sites and energy grid to future scenarios of storminess and sea level rise.

On gravel and sandy barriers the impact regimes are defined by explicitly coupling hydrodynamic forcing and beach morphology by examining the relationship between the elevation of extreme water levels (e.g., max vertical runup or  $R_{2\%}$ ) and relevant beach morphology (e.g., foredune or barrier crest elevation; Masselink and van Heteren, 2014).

On sandy beaches and barriers these regimes are defined through the application of the most updated runup equations such as Stockdon et al. (2006). A similar approach was recently developed for gravel barriers, with the concept of overwash potential (OP) which represents the level above the crest that the extreme runup will achieve, under a given storm condition (Matias et al., 2012). The OP uses Stockdon et al. (2006), which was defined as the most adequate equation for gravel barriers after extensive testing of different runup equations (Matias et al., 2012). Shortcomings in the application of Stockdon et al. (2006) on gravel barriers may arise from aspects such as the permeability, complex nearshore or foreshore features (e.g., several berms) or the effect of wave spectral shape that are not taken in consideration by this runup equation.

It was demonstrated in Chapter 4 that the presence of a bimodal spectrum can significantly affect the occurrence and magnitude of overwash events. Such process is very well captured by XBeach-G numerical model (McCall et al., 2014) which, beyond other important parameters, includes a non-hydrostatic pressure correction term that allows wave-by-wave modelling of the free surface elevation, allowing the simulation of the whole wave spectrum, including variable spectral shapes. The comparison between extreme runup observations

presented in Chapter 4 and predictions performed with XBeach-G and Stockdon et al. (2006) runup equation show that the latter (based on peak wave period) underestimates significantly the runup elevation (Figure 5.7).

Potential reasons for such evident underestimation is the fact that Stockdon et al. (2006) equation was not validated for extreme waves ( $H_s > 3$  m), and very important processes such as the wave bimodality are not taken in account on this formulation. From all these reasons the former assume particular importance since in Chapter 4 it was demonstrated with Xbeach-G model that for these particular storm conditions, if the wave forcing is performed using a unimodal wave spectra (maintaining the energy and significant wave height), the model also underestimates the field measurements.



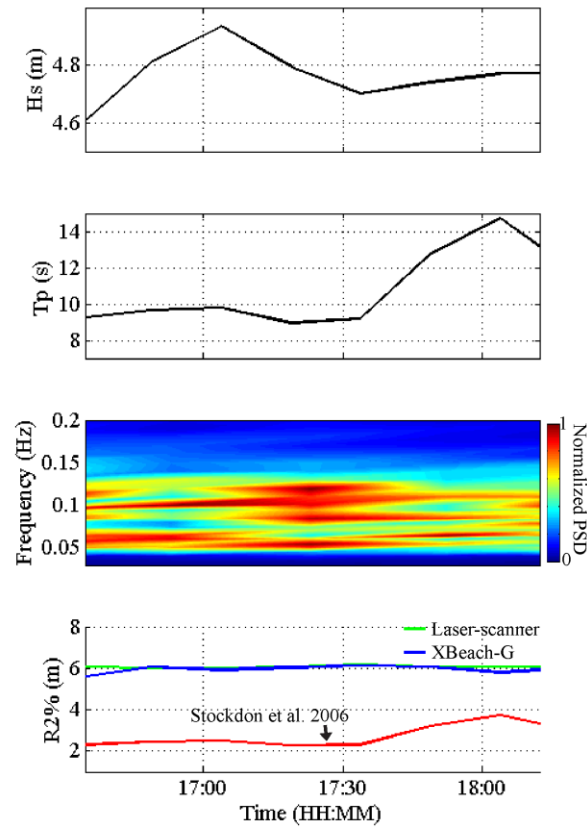


**Figure 5.7** Comparison between vertical runup observations and predictions using Stockdon et al., (2006) runup equation and Xbeach-G numerical model (bottom panel), forced with 2 hours of wave measurements (performed at Porthleven wave buoy) during the storm presented in Chapter 4; Stockdon et al., (2006) runup equation was implemented using significant offshore wave height (top panel), peak period (second panel), while Xbeach-G used the full wave spectra (third panel). For these simulations it was used the tide elevation presented in Chapter 4.

Predicting accurately the extreme runup on gravel barriers during extreme storm is crucial to assess the vulnerability of these environments to destructive hazards such as overwashes, but also to understand the link between extreme hydrodynamic regimes and the long-term morphological evolution of these systems (Orford et al., 2003).

Traditionally the assessment of the vulnerability of a barrier to overwash and coastal flooding is performed using the joint probability of wave height and water levels (e.g., Ciavola and

Stive, 2012). Little importance is given to wave period or to the shape of the spectrum of the offshore incident waves; however, Chapter 4 demonstrates that these two parameters are crucial and overtopping and overwash discharge are very sensitive to these parameters. Modifications to these parameters significantly affect the magnitude of overtopping and overwash discharge predictions; in turn, this has a direct effect on the definition of the different storm impact regimes (Figure 5.8).

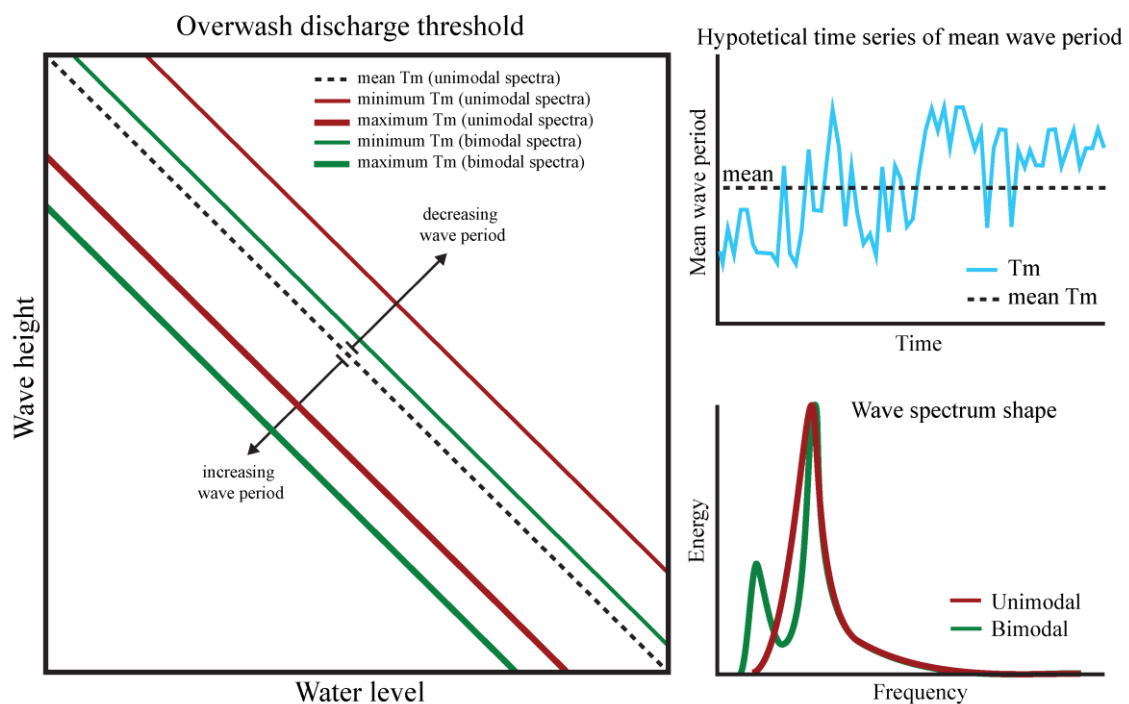


**Figure 5.8** Diagram illustrating the effect of the modification of wave period and spectral shape on the definition of the overwash discharge threshold (left panel). This overwash discharge map was produced based on a combination of water levels and wave heights and using a hypothetical wave period time series which express the variability of this parameter along the time (top right panel); the different statistical moments of this distribution (mean, max and min) were used to produce the discharge map, using different wave spectra shapes: unimodal and bimodal (bottom right panel).

The present research project provide strong evidence that an adequate mapping of the storm impact regimes on a gravel barrier requires, in addition to the combination of water level and

wave height, the integration of the full range of wave period and spectral shapes present on the wave climate of the considered location. Taking these aspects into consideration means that the definition of the different impact regimes will account for the first order hydrodynamic forcing elements that describe the behaviour of extreme runup on gravel barriers (Figure 5.8).

Wave runup is a key factor controlling the long-term evolution of gravel barriers. The elevation of the crest reflects a balance between runup sufficient to deposit material at the beach crest (during overtopping) and runup sufficient to exceed the crest and move material onto the back-barrier slope (overwash), the latter leading to barrier transgression via rollover (e.g., Orford and Carter, 1982).

The link between the wave runup and barrier morphological response was recently investigated on a large laboratory experiment (BARDEX - Williams et al., 2011), where a proto-type scale gravel barrier ( $D_{50} = 11$  mm) was tested under different wave and water levels. The results from this experiment confirmed that under overtopping conditions the barrier crest was gradually raised and narrowed, becoming less vulnerable to overwash, while during overwash conditions the crest was lowered and the width of the barrier increased (Matias et al., 2012).

In the present research project similar analysis were performed using the validated Xbeach-G model, in order to investigate the morphological response of a fine gravel barrier (Loe Bar) under overtopping and overwashing conditions (Chapter 4). The findings revealed that while under overwash flow conditions (defined as average flow discharges over the crest above  $20 \text{ l/s/m}$ ) the present results agree with the existing conceptual knowledge of gravel barrier, and

barrier rollover was verified. Under overtopping flows (average discharge flow under 20 l/s/m) the morphological response was different and instead of the build-up of the barrier crest it was found deposition on the back of the barrier (Section 4.3.5).

These results provide strong insights that the mechanism of crest build-up under overtopping conditions are absent on finer gravel barriers and that sediment size is a key element to trigger this process. While on coarse gravel barriers vertical accretion at the runup-limit is a result of rapid crestal infiltration (Orford and Carter, 1982), on a fine gravel barrier the lower hydraulic conductivity of the finer sediments, promote quicker saturation of the ground causing limited dissipation to the overtopping flow. This aspect together with the lower threshold for transport of finer gravel sediments are likely to be the key mechanisms responsible for the sedimentation on the back of the barrier predicted by Xbeach-G under overtopping flows (Chapter 4).

These findings are significantly important in the context of the present research project since they suggests that the morphological response of coarse and fine gravel barriers to overtopping conditions might be different (Figure 5.9). Thus while on coarser gravel barriers overtopping flows are expected to increase the beach face slope (due to erosion of the beach face and deposition at the top of the crest), raise the crest elevation and reduce the barrier width (Matias et al, 2012), on fine gravel barriers similar hydrodynamic conditions are expected to reduce the beach face slope, maintain or reduce the barrier crest and raise or extend the back of the barrier face (Figure 5.9).

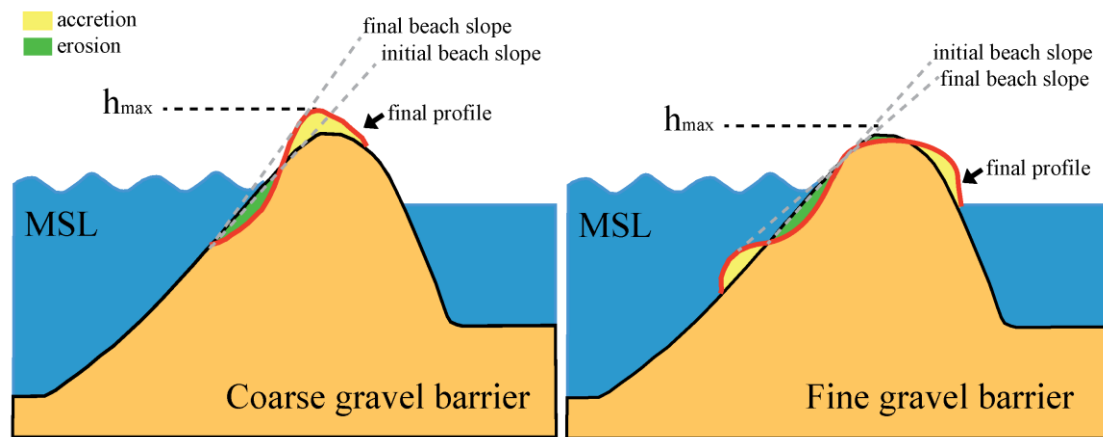


**Figure 5.9** Illustration of the two types of morphological response that a coarse (left) and a fine (right) gravel barrier present under overtopping conditions.

Despite these distinct morphological responses both represent fundamental mechanisms of resilience of these environments to a similar hydrodynamic forcing. While on a coarse gravel barrier the increase of the crest provides more protection to future extreme storms and decrease the likelihood of overwashing (Matias et al., 2012), on fine barriers the lowering of the beach face and widening of the barrier may impose extra dissipation to storm runup flows and reduce the magnitude of overwash transport, thus inducing a feedback control on migration rate.

## 5.4 Conclusions

The aim of the present research project has been to provide new insights on the swash zone morphodynamics of coarse-grained beaches (pure gravel - PG, mixed and composite sand and gravel beaches - MSG and CSG respectively) under the full range of energetic hydrodynamic conditions (positive, zero and negative freeboard). The following bullet points summarise the key findings in relation to the initial thesis aim:

- An innovative method, 2D laser-scanner was developed to measure high frequency swash zone hydro- and morphodynamics during storms. This method allowed the complete coverage of the swash zone of six different coarse-grained beaches with a vertical accuracy of approximately  $\pm 0.015$  m and average horizontal resolution of 0.07 m. The quality of the measurements performed with this new instrument showed that are within the accuracy of traditional field techniques (e.g. video cameras, ultrasonic bed-level sensors or dGPS), thus confirming the capability of this remote sensing tool to perform these type of observations.
- This new remote sensing method has great versatility (e.g., it can be deployed on the top of a dune crest or seawall) and can perform high quality measurements under very adverse conditions (e.g., rain, strong winds, etc.) or reduced light conditions. This aspect, together with the fact that it does not need to be deployed *in-situ* to collect data, makes this instrument the best solution for measuring the swash zone under storm conditions.

The 2D laser-scanner was used to collect high quality datasets of swash zone hydrodynamics and morphological response under different storm conditions. With reference to the swash zone dynamics under storms with positive freeboard regimes the present findings provide the following new insights:

- Coarse-grained beaches such as PG, CSG and MSG beaches, present distinct swash zone hydrodynamics and morphological responses during energetic wave conditions ( $H_s > 2$  m). The dissipative character of their different surf zones together with the beach step dynamics are key elements underlying their distinct swash zone responses.
- Extreme runup measured on the different coarse-grained beaches was found to have an inverse relationship with the surf scaling parameter. The highest vertical runup excursions were found on the steepest beaches (PG beaches) and under long-period swell, while lower vertical runup excursions were linked to short-period waves and beaches with gentle intertidal slopes with intermediate and dissipative surf zones. This demonstrates that the contrasting degree of wave dissipation observed in the different types of surf zones is a key factor that control the extreme runup: while on steep beaches (like PG beaches) breaking is delayed and waves break and run directly up the beach with little surf zone dissipation leading to high vertical runup excursions; on flatter slopes, earlier breaking results in higher levels of surf zone dissipation and lower vertical runup excursions. Ground-water interaction and morphological changes can also play an important role, however Xbeach-G modeling results showed that these are second order of importance for the prediction of extreme wave runup.

- Contrasting morphological responses were observed on the different coarse-grained beaches as a result of the different swash/surf zone dynamics. PG beaches with narrow surf zone, presented an asymmetric morphological response during the tide cycle (accretion during the rising and erosion during the falling tide) as a result of beach step adjustments to the prevailing hydrodynamics. On dissipative MSG and CSG beaches the morphological response was not significant due to the very dissipative surf zone, while on an intermediate CSG beach significant erosion of the beach face and berm was observed during the entire tide cycle as a result of moderate surf zone wave dissipation and absence of beach step dynamics.
- Fundamental processes underlying the link between the beach step dynamics and the asymmetrical response during the tidal cycle were for the first time measured under energetic wave conditions. During the rising tide the onshore shift of the breaking point triggers the onshore translation of the step and favors accretion (step deposit development), while during ebb the offshore translation of the wave breaking point triggers retreat of the step and favours backwash sediment transport (erosion of the step deposit).

With reference to the swash zone dynamics under storms with zero and negative freeboard regimes:

- Present field measurements and numerical modelling (Xbeach-G) provide clear evidence that the presence of bimodal wave spectra can increase the likelihood of the occurrence of overtopping and overwash events over a gravel barrier.
- Most runup equations (e.g., Stockdon et al., 2006) used to predict the thresholds for storm impact regime (e.g., swash, overtopping and overwash) on barriers, lack



adequate characterisation of the full wave spectra, and therefore miss important aspects of the incident wave field, such as wave bimodality. XBeach-G allows a full characterization of the incident wave field and is capable of predicting the effect of wave spectra bimodality on the runup, thus demonstrating that is a more appropriate tool for predicting the storm impact regimes on gravel barriers.

- Regarding the definition of storm impact regimes on gravel barriers, it was found that wave period and wave spectra bimodality are key parameters that can significantly affect the definition of the thresholds for these different regimes. Present findings showed that while short period waves dissipate most of their energy before reaching the swash zone (due to breaking) and produce short runup excursions, long period waves due to their low steepness arrive to the swash with enhanced heights (due to shoaling) and break on the edge of the swash, thus promoting large runup excursions. When the offshore wave spectrum presents a bimodal shape, the wave transformation on shallow waters favours the long period peak (even if the short period waves peak is the most energetic offshore) and large runup excursions are verified.
- XBeach-G simulations show that the morphological response of fine gravel barriers is distinct to coarse gravel barriers under similar overtopping conditions. While on coarser barriers overtopping regimes are expected to increase the crest elevation and narrow the barrier, on fine barriers under the same hydrodynamic conditions sedimentation occurs on the back of the barrier and in the lower beach face. Underlying such different sedimentation patterns are the different hydraulic conductivity of the different sediment sizes which control the amount of flow

dissipation (due to infiltration), and therefore the capacity of the flow to transport sediment behind the crest.

# References

- Aagaard, T., Hughes, M.G., 2010. Breaker turbulence and sediment suspension in the surf zone. *Marine Geology*, 271, pp. 250-259.
- Admiralty Tide Tables United Kingdom and Ireland (including European Channel Ports) Hydrographic Office, Taunton, U.K (2009).
- Almeida, L.P., Voudoukas, M.V., Ferreira, Ó., Rodrigues, B.A., Matias, A., 2012. Thresholds for storm impacts on an exposed sandy coastal area in southern Portugal. *Geomorphology*, 143–144, pp. 3–12.
- Almeida, L.P., Masselink, G., Russell, P., Davidson, M., Poate, T., McCall, R., Blenkinsopp, C., Turner, I., 2013. Observations of the swash zone on a gravel beach during a storm using a laser-scanner. *Journal of Coastal Research Proceedings 12th International Coastal Symposium* (Plymouth, England), pp. 636–641 (Special Issue No. 65).
- Almeida, L.P., Masselink, G., Russell, P., Davidson, M., McCall, R., Poate, T., 2014. Swash zone morphodynamics of coarse-grained beaches during energetic wave conditions. *Proceedings to International Conference on Coastal Engineering*, Seoul, South Korea.
- Almeida, L.P., Masselink, G., Russell, P., Davidson, M., 2015. Observations of gravel beach dynamics during high energy wave conditions using a laser scanner. *Geomorphology*, 228, pp. 15-27.
- Alsina, J.M., Falchetti, S., Baldock, T.E., 2009. Measurements and modelling of the advection of suspended sediment in the swash zone by solitary waves. *Coastal Engineering*, 56, pp. 621–631.
- Austin, M.J., Masselink, G., 2006. Observations of morphological change and sediment transport on a steep gravel beach. *Marine Geology*, 229, pp. 59–77.
- Austin, M.J., Buscombe, D., 2008. Morphological change and sediment dynamics of the beach step on a macrotidal gravel beach. *Marine Geology*, 249, pp. 167–183.

Battjes, J.A., 1974. Surf similarity. Proc. 14th Conference on Coastal Engineering, American Society of Civil Engineers, pp. 466-480.

Blenkinsopp, C.E., Mole, M.A., Turner, I.L., Peirson, W.L., 2010. Measurements of the time-varying free-surface profile across the swash zone obtained using an industrial lidar. Coastal Engineering, 57, pp. 1059-1065.

Blenkinsopp, C.E., Turner, I.L., Masselink, G., Russell, P.E., 2011. Swash zone sediment fluxes: field observations. Coastal Engineering, 58, pp. 28-44.

Blenkinsopp, C.E., Turner, I.L., Allis, M.J., Peirson, W.L., Garden, L.E., 2012. Application of LiDAR technology for measurement of time-varying free-surface profiles in a laboratory wave flume. Coastal Engineering, 68, pp. 1-5.

Bradbury, A., Cope, S.N., Prouty, D.B., 2005. Predicting the response of shingle barrier beaches under extreme wave and water level conditions in Southern England. Proc. Coast.Dynam.ASCE, Barcelona, Spain. Paper 144.

Bray, T.F., Carter, C.H., 1992. Physical processes and sedimentary record of a modern, transgressive, lacustrine barrier island. Marine Geology, 105, pp. 155–168.

Brocchini, M., Baldock, T.E., 2008. Recent advances in modeling swash zone dynamics: influence of surf–swash interaction on nearshore hydrodynamics and morphodynamics. Reviews of Geophysics, 46, RG3003.

Brodie, K.L., Slocum, R.K., McNinch, J.E., 2012. New insights into the physical drivers of wave runup from a continuously operating terrestrial laser scanner. Final Proceedings of Ocean's 12, Virginia, U.S.A., pp. 1-8.

Buscombe, D., Masselink, G., 2006. Concepts in gravel beach dynamics. Earth Science Reviews, 79, pp. 33–52.

Butt, T., and Russell, P. (2000). Hydrodynamics and cross-shore sediment transport in the swash-zone of natural beaches: a review. Journal of Coastal Research, 255-268.

Carr, A.P., 1969. Size grading along a pebble beach: Chesil Beach, England. Journal of Sedimentary Petrology, 39, pp. 297–311.

Carr, A.P., 1983. Shingle beaches: aspects of their structure and stability. Shoreline protection. Proceedings of Shore Protection, A Conference Organised by the Institution of Civil Engineers. University of Southampton, Thomas Telford, pp. 69–76

Carter, R.W.G., Orford, J.D., 1984. Coarse clastic barrier beaches: a discussion of the distinctive dynamic and morphosedimentary characteristics. *Marine Geology*, 60, pp. 377–389.

Carter, R.W.G., Orford, J.D., 1993. The morphodynamics of coarse clastic beaches and barriers: a short- and long-term perspective. *Journal of Coastal Research*, 15, pp. 158-179.

Christensen, E.D., Deigaard, R., 2001. Large eddy simulation of breaking waves. *Coastal Engineering*, 42, pp. 53–86.

Ciavola, P., Stive, M., 2012. Thresholds for storm impacts along European coastlines: Introduction. *Geomorphology*, 143, pp. 1-2.

Contardo, S. and Symonds, G., 2013. Infragravity response to variable wave forcing in the nearshore. *Journal of Geophysical Research*, 118, pp. 7095-7106.

Darcy, H., 1856. Les fontaines publiques de la ville de Dijon. Tech. Rep., Dalmont, Paris.

Donnelly, C., 2008. Coastal Overwash: Processes and Modelling. Lund University, Sweden (53 pp).

Elfrink, B., and Baldock, T. (2002). Hydrodynamics and sediment transport in the swash zone: a review and perspectives. *Coastal Engineering*, 45(3), 149-167.

Feser, F., Barcikowska, M., Krueger, O., Schenk, F., Weisse, R., Xia, L., 2014. Storminess over the North Atlantic and northwestern Europe a review. *Quarterly Journal of the Royal Meteorological Society*, 141, pp. 350-382.

Fredsøe, J., Deigaard, R., 1992. Mechanics of coastal sediment transport, advanced series on ocean engineering, Vol. 3. World Scientific, Singapore.

Fisher, J. S. and Stauble, D. K. 1977. Impact of Hurricane Belle on Assateague Island washover. *Geology*, 5, pp. 765-768.

Frizell, K.H., Ruff, J.F., and S. Mishra, 1998. Simplified design guidelines for riprap subjected to overtopping flow. Proceedings of the Annual Conference of the Assoc. of State Dam Safety Officials, pp. 301–312.

Guza, R.T., Inman, D.L., 1975. Edge waves and beach cusps. *Journal of Geophysical Research*, 80, pp. 2997-3012.

Hawkes, P.J., Coates T.T., Jones, R.J., 1998. Impact of bi-model seas on beaches and control structures. Research report SR 507, HR Wallingford.

Holland, K.T., Holman, R.A., Sallenger, A.H., 1991. Estimation of overwash bore velocities using video techniques. Proceedings of Coastal Sediments '91, USACE, Seattle, Washington, USA, pp. 489–497.

Holman, R. A., 1986. Extreme value statistics for wave run-up on a natural beach. *Coastal Engineering*, 9, pp. 527-544.

Horn, B.K., 1987. Closed-form solution of absolute orientation using unit quaternions. *Journal of Optical Society of America*, 4, pp. 629-642.

Horn, D.P., Li, L., Holmes, P., 2003. Measurement and modelling of gravel beach groundwater response to wave run-up. Coastal Sediments '03. ASCE, New York.

Horn, D.P., Li, L., 2006. Measurement and modelling of gravel beach groundwater response to wave run-up: effects on beach profile changes. *Journal of Coastal Research*, 22, pp. 1241-1249.

Hughes, M.G., Cowell, P.J., 1987. Adjustment of reflective beaches to waves. *Journal of Coastal Research*, 3, pp. 153–167.

Ivamy, M.C., Kench, P.S., 2006. Hydrodynamics and morphological adjustment of a mixed sand and gravel beach, Torere, Bay of Plenty, New Zealand. *Marine Geology*, 228, pp. 137–152.

Jennings, R., Schulmeister, J., 2002. A field based classification scheme for gravel beaches. *Marine Geology*, 186, pp. 211-228.

Jiang, A.W., Hughes, M., Cowell, P., Gordon, A., Savioli, J.C., Ranasinghe, R., 2010. A hybrid model of swash-zone longshore sediment transport on reflective beaches. Proceedings of International Conference on Coastal engineering, Shanghai, China.

Kemp, P.H., 1961. The relationship between wave action and beach profile characteristics. Proc. Seventh Conference on Coastal Engineering, American Society of Civil Engineers, pp. 262-277.

Kirk, R. M., 1970: Swash zone processes: An examination of water motion and the relations between water motion and foreshore response on some mixed sand and shingle beaches, Kaikoura, New Zealand. Ph.D. thesis, Dept Geography, Univ. Canterbury, Christchurch, New Zealand.

Kirk, R.M., 1980. Mixed sand and gravel beaches: morphology, processes and sediments. Progress in Physical Geography, 4, pp. 189-210.

Kulkarni, C.D., Levoy, F., Montfort, O., Miles, J., 2004. Morphological variations of a mixed sediment beachface (Teignmouth, UK). Continental Shelf Research, 24, pp. 1203–1218.

Leatherman, S.P., 1976. Quantification of overwash processes. Charlottesville, Virginia: Department of Environmental Sciences, University of Virginia, PhD dissertation, 245 pp.

Leatherman, S.P., 1977. Overwash hydraulics and sediment transport. Proceedings of Coastal Sediments '77. ASCE, Charleston, USA, pp. 135–148.

Leatherman, S.P., Zaremba, R.E., 1987. Overwash and aeolian processes on a U.S. Northeast coast barrier. Sedimentary Geology 52, pp. 183–206.

Lippmann, T.C., Holman, R.A., 1989. Quantification of sand bar morphology: a video technique based on wave dissipation. Journal of Geophysical Research, 94, pp. 995–1011.

Longuet-Higgins, M., and R. Stewart, 1962. Radiation stress and mass transport in gravity waves, with application to surf beats, Journal of Fluid Mechanics, 13, pp. 481–504.

Lorang, M.S., 2002. Predicting the crest height of a gravel beach. Geomorphology, 48, pp. 87–101.

Mason, T., Voulgaris, G., Simmonds, D.J., Collis, M.B., 1997. Hydrodynamics and sediment transport o composite (mixed sand/shingle) beaches: a comparison. Coastal Dynamics '97. ASCE, pp. 48–57.

Masselink, G., Li, L., 2001. The role of swash infiltration in determining the beachface gradient: a numerical study. Marine Geology. 176, pp. 139–156.

Masselink, G., Russell, P., Turner, I.L., Blenkinsopp, C., 2009. Net sediment transport and morphological change in the swash zone of a high-energy sandy beach from swash event to tidal cycle time scales. Marine Geology, 267, pp. 18-35.

Masselink, G., Russell, P., Blenkinsopp, C.E., Turner, I.L., 2010. Swash zone sediment transport, step dynamics and morphological response on a gravel beach. Marine Geology, 274, pp. 50–68.

Masselink, G., Turner, I.L., 2012. Large-scale laboratory investigation into the effect of varying back-barrier lagoon water levels on gravel beach morphology and swash zone sediment transport. Coastal Engineering 63, pp. 23–38.

Masselink, G., Turner, I.L., Conley, D.C., Ruessink, B.G., Matias, A., Thompson, C., Castelle, B., Wolters, G., 2013. BARDEX II: Bringing the beach to the laboratory – again!. Journal of Coastal Research, Special Issue 65, pp. 1545-1550.

Masselink, G., van Heteren, S., 2014. Response of wave-dominated and mixed-energy barriers to storms. Marine Geology, 352, pp. 321-347.

Masselink, G., McCall, R., Poate, T., Van Geer, P., 2014. Modelling storm response on gravel beaches using XBeach-G.Proceedings of the ICE - Maritime Engineering, 167, pp. 173-191.

Matias, A., Ferreira, Ó., Vila-Concejo, A., Morris, B., Dias, J.A., 2010. Short-term morphodynamics of non-storm overwash. Marine Geology 274, pp. 69–84.

Matias, A., Williams, J.J., Masselink, G., Ferreira, Ó., 2012. Overwash threshold for gravel barriers. Coastal Engineering, 63, pp. 48–61.

Matias, A., Blenkinsopp, C., Masselink, G., 2014. Detailed investigation of overwash on a gravel barrier. Marine Geology, 350, pp. 27-38.



Matias, A., Masselink, G., Castelle, B., Blenkinsopp, C., Kroon, A., in press. Measurements of morphodynamic and hydrodynamic overwash processes in a large-scale wave flume. *Coastal Engineering*.

McCall, R., Masselink, G., Roelvink, J., Russell, P., Davidson, M., Poate, T., 2012. Modeling overwash and infiltration on gravel barriers. *Proceedings of the 33rd International Conference on Coastal Engineering*.

McCall, R., Masselink, G., Poate, T., Bradbury, A., Russell, P., Davidson, M., 2013. Predicting overwash on gravel barriers. *Journal of Coastal Research Special Issue No. 65 Proceedings 12th International Coastal Symposium*, pp. 1473–1478.

McCall, R., Masselink, G., Poate, T., Roelvink, J., Almeida, L., Davidson, M., Russell, P., 2014. Modelling storm hydrodynamics on gravel beaches with Xbeach-G. *Coastal Engineering* 91, pp. 231-250.

McCall, R., Masselink, G., Poate, T., Roelvink, D., Almeida, L.P. 2015. Modelling storm morphodynamics on gravel beaches with Xbeach-G. *Coastal Engineering*, 103, 52-66.

Mendez Lorenzo, A.B., van der Meer, J.W., Hawkes, P.J., 2000. Effects of bi-modal waves on overtopping: application of UK and Dutch prediction methods. *Proceedings to International Conference on Coastal Engineering, Sydney, Australia*, pp. 2114-2127.

Miettinen, M., Ohman, M., Visala, A., Forsman, P., 2007. Simultaneous localization and mapping for forest harvesters. *Final Proc. of IEEE International Conference on Robotics and Automation, Rome, Italy*, pp. 517-522.

Miles, J., Russell, P., 2004. Dynamics of a reflective beach with a low tide terrace. *Continental Shelf Research*, 24, pp. 1219-1247.

Morton, R.A., Gonzalez, J.L., Lopez, G.I., Correa, I.D., 2000. Frequent non-storm washover of barrier islands, Pacific coast of Columbia. *Journal of Coastal Research*, 16, pp. 82-87.

Moses, C.A., Williams, R.B.G., 2008. Artificial beach recharge: the south-east England experience. *Zeitschrift für Geomorphologie*, 52, pp. 107–124.

Nicholls, R.J., Marinova, N., Lowe, J.A., Brown, S., Vellinga, P., De Gusmão, D., Hinkel, J., Tol, R.S.J., 2011. Sea-level rise and its possible impacts given a ‘beyond 4 °C world’ in the twenty-first century. *Philosophical Transactions of the Royal Society*, 369, pp. 161–181.

Obhrai, C., Powell, K., Bradbury, A., 2008. A laboratory study of overtopping and breaching of shingle barrier beaches. Proceedings of International Conference on Coastal Engineering, Hannover, Germany, pp. 1497–1508.

Orford, J., Jennings, S.C., Pethick, J., 2003. Extreme storm effect on gravel-dominated barriers. Final Proc. of the International Conference on Coastal Sediments, St Petersburg, United States, pp. 1-12.

Orford, J.D., Carter, R.W.G., 1982. Crestal overtop and washover sedimentation on a fringing sandy gravel barrier coast, Carnsore Point, Southeast Ireland. Journal of Sedimentary Petrology, 52, pp. 265–278.

Orford, J.D., Carter, R.W.G., 1984. Mechanisms to account for the longshore spacing of overwash throats on a coarse clastic barrier in southeast Ireland. Marine Geology, 56, pp. 207–226.

Orford, J.D., Cooper, J.A.G., Jackson, D., Malvarez, G., White, D., 1999. Extreme storms and thresholds on foredune stripping at Inch Spit, South-West Ireland. Proc. Coast. Sedim. '99. ASCE, New York, U.S.A, pp. 1852–1866.

Osborne, P.D., 2005. Transport of gravel and cobble on a mixed sediment inner bank shoreline of a large inlet, Grays Harbor, Washington. Marine Geology, 224, pp. 145–156.

Pallejà, T., Teixidó M., Tresanchez, M., Palacín J., 2009. Measuring gait using a ground laser range sensor. Sensors, 9, pp. 9133-9146.

Pedrozo-Acuña, A., Simmonds, D.J., Otta, A.K., Chadwick, A.J., 2006. On the cross-shore profile change of gravel beaches. Coastal Engineering, 53, pp. 335–347.

Plant, N.G. and Holman, R.A., 1997. Intertidal Beach Profile Estimation Using Video Images. Marine Geology, 140, pp. 1–24.

Poate, T., Masselink, G., Davidson, M., McCall, R., Russell, P., Turner, I., 2013. High frequency *in-situ* field measurements of morphological response on a fine gravel beach during energetic wave conditions. Marine Geology 342, pp. 1–13.

Polidoro A, Dornbusch U and Pullen T (2013) Improved maximum run-up formula for mixed beaches based on field data. In Allsop W and Burgess K (eds). Proceedings of the ICE Breakwaters Conference.

Pontee, N.I., Pye, K., Blott, S.J., 2004. Morphodynamic behaviour and sedimentary variation of mixed sand and gravel beaches, Suffolk, UK. *Journal of Coastal Research*, 20 , pp. 256–276.

Roelvink, D., Reniers, A., van Dongeren, A., de Vries, J.T., McCall, R., Lescinski, J., 2009. Modelling storm impact on beaches, dunes and barrier islands. *Coastal Engineering*, 56, pp. 1133–1152.

Ruessink, G., Michallet, H., Bonneton, P., Mouaze, D., Lara, J.L., Silva, P.A., Wellens, P., 2013. Globex: Wave dynamics on a gently sloping laboratory beach. *Proceedings to the 7th International Conference on Coastal Dynamics*.

Ruggiero, P., R.A., Holman, and R.A. Beach, 2004. Wave run-up on a high-energy dissipative beach. *Journal of Geophysical Research*, 109, pp. 1-12.

Ruiz de Alegria-Arzaburu, A. & Masselink, G., 2010 'Storm response and beach rotation on a gravel beach, Slapton Sands, U.K', *Marine Geology*, 278, pp. 77-99.

Sallenger Jr., A.H., 2000. Storm impact scale for barrier islands. *Journal of Coastal Research* 16, pp. 890–895.

Saville, T., 1958. Wave run-up on composite slopes. *Proceedings of the 6th International Conference on Coastal Engineering*, Miami, USA, pp. 691-699.

Scott, T., Masselink, G., Russell, P., 2011. Morphodynamic characteristics and classification of beaches in England and Wales. *Marine Geology*, 286, pp. 1-20.

Senechal, N., Coco, G., Bryan, K. R., Holman, R., 2011. Wave runup during extreme storm conditions. *Journal of Geophysical Research*, 116, pp. 1-13.

SICK, 2009. LD-OEM1000 to 5100 Laser Measurement System – operating manual. SICK AG Waldkirch, Germany.

Simm J. D. (Editor), 1991. Manual on the use of rock in coastal and shoreline engineering. CIRIA special publication 83, CUR Report 154.

Single, M.B., 1992. Hi energy coastal processes on mixed sand gravel beaches. PhD Thesis, University of Canterbury, New Zealand.

Smit, P., Zijlema, M., Stelling, G., 2013. Depth-induced wave breaking in a non-hydrostatic, near-shore wave model. *Coastal Engineering*, 76, pp. 1–16.

Sou, I. M., E. A. Cowen, and P. L.-F. Liu, 2010. Evolution of the Turbulence Structure in the Surf and Swash Zones, *Journal of Fluid Mechanics*, 644, 193–216.

Soulsby, R. L., Whitehouse, R. J. S. W., 1997. Threshold of sediment motion in coastal environments. In: *Pacific Coasts and Ports '97 Conference*. Univ. of Canterbury, Christchurch, New Zealand.

Srinivas, R., Dean, R.G., Parchure, T.M., 1992. Barrier Island Erosion and Overwash Study. Volume 1. Coastal and Ocean Engineering Department, University of Florida (92 pp.).

Stockdon, H.F., Holman, R.A., 2000. Estimation of wave phase speed and nearshore bathymetry from video imagery. *Journal of Geophysical Research*, 105, pp. 22015–22033.

Stockdon, H.F., Holman, R.A., Howd, P.A. and Sallenger Jr., A. H., 2006. Empirical parameterization of setup, swash and runup. *Coastal Engineering*, 53, pp. 573–588.

Strahler, A.N., 1966. Tidal cycle of changes in an equilibrium beach, Sandy Hook, New Jersey. *Journal of Geology*, 74, pp. 247–268.

Streicher, M., Hofland, B., Lindenbergh, R.C., 2013. Laser ranging for monitoring water waves in the new Deltares Delta flume. *Proceedings to ISPRS Workshop Laser Scanning*, Antalya, Turkey, pp. 271-276.

Teixido, M., Palleja, T., Davinia, F., Tresanchez, M., Moreno, J., Palacin, J., 2012. Two-dimensional radial laser scanning for circular marker detection and external mobile robot tracking, *Sensors*, 12 pp. 16482-16497.

Turner, I.L., Russell, P.E., Butt, T., 2008. Measurement of wave-by-wave bed-levels in the swash zone. *Coastal Engineering*, 55, pp. 1237–1242.

Turner, I., Masselink, G., 1998. Swash infiltration-exfiltration and sediment transport. *Journal of Geophysical Research*, 103, pp. 813-824.

Turner, R.J., 1990. The effects of a mid-foreshore groundwater effluent zone on tidal-cycle sediment distribution in Puget Sound, Washington. *Journal of Coastal Research*, 6, pp. 597-610.

Van Rijn, L., 2007. United view of sediment transport by currents and waves, i: Initiation of motion, bed roughness, and bed-load transport. *Journal of Hydraulic Engineering*, 133, pp. 649–667.

Van Wellen, E., Chadwick, A.J., Mason, T., 2000. A review and assessment of longshore sediment transport equations for coarse grained beaches. *Coastal Engineering* 40, pp. 243–275.

Vásquez-Martín, R., Núñez, P., Bandera, A., Sandoval, F., 2009. Curvature-based environment description for robot navigation using laser range sensors. *Sensors*, 9, pp. 5894–5918.

Voulgaris, G., Collins, M.B., 2000. Sediment resuspension on beaches: response to breaking waves. *Marine Geology*, 167, pp. 137–187.

Vouskoulas, M.I.; Kirupakaramoorthy, T.; Oumeraci, H.; de la Torre, M.; Wubbold, F.; Wagner, B., and Schimmels, S., 2014. The role of combined laser scanning and video techniques in monitoring waveby-wave swash zone processes. *Coastal Engineering*, 83, pp. 150–165.

Waddell, E., 1973. Dynamics of swash and implications to beach response. Technical Report 139, Coastal Studies Institute, Louisiana State University, Baton Rouge, U.S.A..

Whitecombe, L.J., 1996. Behaviour of an artificially replenished shingle beach at Hayling Island, UK. *Quarterly Journal of Engineering Geology*, 29, pp. 265–271.

Williams, J.J., Buscombe, D., Masselink, G., Turner, I.L., Swinkels, C., 2011. Barrier Dynamics Experiment (BARDEX): aims, design and procedures. *Coastal Engineering* 63, pp. 3–12.

Wübbold, F., Vousdoukas, M.I., Hentschel, M., Wagner, B., 2012. Towards Autonomous Coastal Monitoring using 3D Laser Range Scanners and Camera Vision. 33rd International Conference on Coastal Engineering, Santander, Spain.

## Appendix I

**Parameters used in Xbeach-G to investigate the influence of increasing the wave peak period and spectral shape on the overtopping and overwash discharge. These conditions were used for the swash regime.**

Spectra	H <sub>s1</sub> (m)	T <sub>p1</sub> (s)	H <sub>s2</sub> (m)	T <sub>p2</sub> (s)	T <sub>p</sub> (s)	T <sub>m</sub> (s)
1	3.7	6	-	-	6	5
2	3.5	5.7	1	15	5.7	5
3	3.1	4.9	2	15	15	5
1	3.7	7	-	-	7	5.9
2	3.6	6.7	1	15	6.8	5.9
3	3.2	5.8	2	15	15	5.9
1	3.7	8	-	-	8	6.7
2	3.6	7.6	1	15	7.6	6.7
3	3.2	6.8	2	15	6.8	6.7
1	3.7	9	-	-	9	7.5
2	3.6	8.8	1	15	8.8	7.5
3	3.2	7.9	2	15	7.9	7.5
1	3.7	10	-	-	10	8.4
2	3.6	9.8	1	15	9.8	8.4
3	3.3	9	2	15	9	8.4
1	3.7	11	-	-	11	9.2
2	3.7	10.8	1	15	10.8	9.2
3	3.4	10.1	2	15	10.1	9.2
1	3.7	12	-	-	12	10
2	3.7	12	1	15	12	10
3	3.5	11.5	2	15	11.5	10
1	3.7	13	-	-	13	10.9
2	3.7	12.9	1	15	12.9	10.9
3	3.6	12.8	2	15	12.8	10.9
1	3.7	14	-	-	14	11.7
2	3.7	13.9	1	15	13.9	11.7
3	3.7	13.7	2	15	13.7	11.7
1	3.7	15	-	-	15	12.5
2	3.7	14.9	1	15	14.9	12.5
3	3.7	14.9	2	15	14.9	12.5

**Parameters used in Xbeach-G to investigate the influence of increasing the wave peak period and spectral shape on the overtopping and overwash discharge. These conditions were used for the overtopping regime.**

<b>Spectra</b>	<b>H<sub>s1</sub> (m)</b>	<b>T<sub>p1</sub> (s)</b>	<b>H<sub>s2</sub> (m)</b>	<b>T<sub>p2</sub> (s)</b>	<b>T<sub>p</sub> (s)</b>	<b>T<sub>m</sub> (s)</b>
1	5.5	6	-	-	6	5
2	5.2	5.8	1.4	15	5.8	5
3	4.6	4.8	2.9	15	15	5
1	5.5	7	-	-	7	5.9
2	5.3	6.7	1.4	15	6.7	5.9
3	4.7	5.7	2.9	15	15	5.9
1	5.5	8	-	-	8	6.7
2	5.3	7.6	1.4	15	7.6	6.7
3	4.7	6.7	2.9	15	6.7	6.7
1	5.5	9	-	-	9	7.5
2	5.3	8.8	1.4	15	8.8	7.5
3	4.8	7.9	2.9	15	7.9	7.5
1	5.5	10	-	-	10	8.4
2	5.3	9.8	1.4	15	9.8	8.4
3	4.9	9	2.9	15	9	8.4
1	5.5	11	-	-	11	9.2
2	5.4	10.9	1.4	15	10.9	9.2
3	4.9	10.1	2.9	15	10.1	9.2
1	5.5	12	-	-	12	10
2	5.4	12	1.4	15	12	10
3	5.1	11.5	2.9	15	11.5	10
1	5.5	13	-	-	13	10.9
2	5.4	12.9	1.4	15	12.9	10.9
3	5.3	12.8	2.9	15	12.8	10.9
1	5.5	14	-	-	14	11.7
2	5.4	13.9	1.4	15	13.9	11.7
3	5.4	13.8	2.9	15	13.8	11.7
1	5.5	15	-	-	15	12.5
2	5.4	14.9	1.4	15	14.9	12.5
3	5.5	14.9	2.9	15	14.9	12.5



**Parameters used in Xbeach-G to investigate the influence of increasing the wave peak period and spectral shape on the overtopping and overwash discharge. These conditions were used for the overwash regime.**

<b>Spectra</b>	<b>H<sub>s1</sub> (m)</b>	<b>T<sub>p1</sub> (s)</b>	<b>H<sub>s2</sub> (m)</b>	<b>T<sub>p2</sub> (s)</b>	<b>T<sub>p</sub> (s)</b>	<b>T<sub>m</sub> (s)</b>
1	6.8	6	-	-	6	5
2	6.4	5.7	1.8	15	5.7	5
3	5.7	4.8	3.6	15	15	5
1	6.8	7	-	-	7	5.9
2	6.5	6.7	1.8	15	6.7	5.9
3	5.8	5.7	3.6	15	15	5.9
1	6.8	8	-	-	8	6.7
2	6.6	7.6	1.8	15	7.6	6.7
3	5.8	6.7	3.6	15	6.7	6.7
1	6.8	9	-	-	9	7.5
2	6.6	8.8	1.8	15	8.8	7.5
3	5.9	7.9	3.6	15	7.9	7.5
1	6.8	10	-	-	10	8.4
2	6.6	9.8	1.8	15	9.8	8.4
3	6.0	9	3.6	15	9	8.4
1	6.8	11	-	-	11	9.2
2	6.7	10.9	1.8	15	10.9	9.2
3	6.1	10.1	3.6	15	10.1	9.2
1	6.8	12	-	-	12	10
2	6.7	12	1.8	15	12	10
3	6.3	11.5	3.6	15	11.5	10
1	6.8	13	-	-	13	10.9
2	6.7	12.9	1.8	15	12.9	10.9
3	6.6	12.8	3.6	15	12.8	10.9
1	6.8	14	-	-	14	11.7
2	6.7	13.9	1.8	15	13.9	11.7
3	6.7	13.8	3.6	15	13.8	11.7
1	6.8	15	-	-	15	12.5
2	6.7	14.9	1.8	15	14.9	12.5
3	6.8	14.9	3.6	15	14.9	12.5

## Appendix II

### First author papers

Almeida, L.P., Masselink, G., Russell, P., Davidson, M., Poate, T., McCall, R., Blenkinsopp, C., Turner, I., 2013. Observations of the swash zone on a gravel beach during a storm using a laser-scanner. *Journal of Coastal Research Proceedings 12th International Coastal Symposium* (Plymouth, England), pp. 636–641 (Special Issue No. 65).

Almeida, L.P., Masselink, G., Russell, P., Davidson, M., McCall, R., Poate, T., 2014. Swash zone morphodynamics of coarse-grained beaches during energetic wave conditions. *Proceedings to International Conference on Coastal Engineering*, Seoul, South Korea.

Almeida, L.P., Masselink, G., Russell, P., Davidson, M., 2015. Observations of gravel beach dynamics during high energy wave conditions using a laser scanner. *Geomorphology*, doi:10.1016/j.geomorph.2014.08.019.